

# TABLE OF CONTENTS

<u>Section</u>	<u>Page</u>
1.0 SUMMARY	1 1/A10
2.0 INTRODUCTION	3 1/A12
2.1 List of Symbols	4 1/A13
3.0 TEST FACILITY DESCRIPTION	6 1/B1
4.0 MODEL DESCRIPTION	10 1/B5
5.0 DATA REDUCTION PROCEDURES	22 1/C3
5.1 Flow Rates	22 1/C3
5.2 Flow Coefficients	23 1/C4
5.3 Thrust Measurements	24 1/C5
5.4 Thrust Coefficient	26 1/C7
5.5 Pressure Data	26 1/C7
6.0 TEST RESULTS AND DISCUSSION	28 1/C9
6.1 Data Quality	28 1/C9
6.2 Model Thrust Coefficients	33 1/C14
6.2.1 Effect of Outer Nozzle Radius Ratio	52 1/E5
6.2.2 Effect of Inner Nozzle Radius Ratio	59 1/E12
6.2.3 Effect of Inner Nozzle Flow Rate and Pressure Ratio	64 1/F3
6.2.4 Effect of External Mach Number	80 1/G5
6.3 Model Flow Coefficients	85 1/G10
7.0 CONCLUSIONS	98 2/B1
APPENDIX - DATA REDUCTION PROCEDURES	99 2/B2
References	107 2/B10

# LIST OF ILLUSTRATIONS

<u>Figure</u>		<u>Page</u>	
1.	Schematic of Model System.	7	1/B2
2.	Schematic of Model Air Supply.	8	1/B3
3.	Schematic of Model Assembly.	11	1/B6
4.	Model Schematics, Configurations 1-4.	12	1/B7
5.	Model Schematics, Configurations 5-8.	13	1/B8
6.	Supersonic Tunnel Association Model Assembly.	15	1/B10
7.	Configuration 2 Mounted in NASA Tunnel.	16	1/B11
8.	Configuration 4 Mounted in NASA Tunnel.	17	1/B12
9.	Configuration 5 Mounted in NASA Tunnel.	18	1/B13
10.	Configuration 6 Mounted in NASA Tunnel.	19	1/B14
11.	Configuration 7 Mounted in NASA Tunnel.	20	1/C1
12.	STA Nozzle Mounted in NASA Tunnel.	21	1/C2
13.	Control Volume Applied to Model Test Setup.	25	1/C6
14.	STA Static Performance with the 3.1699 cm (1.248 in.) Diameter Flowmeter.	30	1/C11
15.	STA Static Performance with the 2.8951 cm (1.1398 in.) Diameter Flowmeter.	31	1/C12
16.	Wind-on STA Nozzle Thrust Coefficients.	32	1/C13
17.	STA Nozzle Bias and Standard Deviation on Static Thrust Coefficient.	34	1/D1
18.	STA Nozzle Bias and Standard Deviation on Flow Coefficient.	35	1/D2
19.	Thrust Coefficients for Configuration 1 [ $(R_r)_0 = 0.902$ , $(R_r)_i = 0.673$ , Bent Inner Plug] with High Inner Flow Rates.	37	1/D4
20.	Thrust Coefficients for Configuration 1 [ $(R_r)_0 = 0.902$ , $(R_r)_i = 0.673$ , Bent Inner Plug] with Low Inner Flow Rates.	38	1/D5

# LIST OF ILLUSTRATIONS (Continued)

<u>Figure</u>		<u>Page</u>	
21.	Configuration 1 Thrust Coefficients Compared to Previous Results.	39	1/D6
22.	Thrust Coefficients for Configuration 2 [ $(R_r)_o = 0.902$ , $(R_r)_i = 0.8$ , Conical Inner Plug] with High Inner Flow Rates.	40	1/D7
23.	Thrust Coefficients for Configuration 2 [ $(R_r)_o = 0.902$ , $(R_r)_i = 0.8$ , Conical Inner Plug] with High Inner Flow Rates.	41	1/D8
24.	Thrust Coefficients for Configuration 3 [ $(R_r)_o = 0.902$ , $(R_r)_i = 0.902$ , Conical Inner Plug] with High Inner Flow Rates.	42	1/D9
25.	Thrust Coefficients for Configuration 3 [ $(R_r)_o = 0.902$ , $(R_r)_i = 0.902$ , Conical Inner Plug] with Low Inner Flow Rates.	44	1/D11
26.	Thrust Coefficients for Configuration 4 [ $(R_r)_o = 0.902$ , $(R_r)_i = 0.8$ , Bent Inner Plug] with Low Inner Flow Rates.	45	1/D12
27.	Thrust Coefficients for Configuration 4 [ $(R_r)_o = 0.902$ , $(R_r)_i = 0.8$ , Bent Inner Plug] with Low Inner Flow Rates.	46	1/D13
28.	Inner Plug Pressure Distributions, Configuration 4 [ $(R_r)_o = 0.902$ , $(R_r)_i = 0.8$ , Bent Inner Plug].	47	1/D14
29.	Thrust Coefficients for Configuration 5 [ $(R_r)_o = 0.853$ , $(R_r)_i = 0.8$ , Conical Inner Plug] with High Inner Flow Rates.	48	1/E1
30.	Thrust Coefficients for Configuration 5 [ $(R_r)_o = 0.853$ , $(R_r)_i = 0.8$ , Conical Inner Plug] with Low Inner Flow Rates.	49	1/E2
31.	Thrust Coefficients for Configuration 6 [ $(R_r)_o = 0.926$ , $(R_r)_i = 0.8$ , Conical Inner Plug] with High Inner Flow Rates.	50	1/E3
32.	Thrust Coefficients for Configuration 6 [ $(R_r)_o = 0.926$ , $(R_r)_i = 0.8$ , Conical Inner Plug] with Low Inner Flow Rates.	51	1/E4
33.	Thrust Coefficients for Configuration 7 [ $(R_r)_o = 0.853$ , $(R_r)_i = 0.902$ , Conical Inner Plug] with High Inner Flow Rates.	53	1/E5

# LIST OF ILLUSTRATIONS (Continued)

Figure		Page	
34.	Thrust Coefficients for Configuration 7 [ $(R_r)_o = 0.853$ , $(R_r)_i = 0.902$ , Conical Inner Plug] with Low Inner Flow Rates.	54	1/E7
35.	Thrust Coefficients for Configuration 8 [ $(R_r)_o = 0.853$ , $(R_r)_i = 0.8$ , Bent Inner Plug] with High Inner Flow Rates.	55	1/E8
36.	Thrust Coefficients for Configuration 8 [ $(R_r)_o = 0.853$ , $(R_r)_i = 0.8$ , Bent Inner Plug] with Low Inner Flow Rates.	56	1/E9
37.	Thrust Coefficient as a Function of Outer Nozzle Radius Ratio for Low Inner Flow and Conical Inner Plug.	57	1/E10
38.	Thrust Coefficient as a Function of Outer Nozzle Radius Ratio for High Inner Flow Rates and Conical Inner Plug.	58	1/E11
39.	Thrust Coefficient as a Function of Outer Nozzle Radius Ratio for Low Inner Flow Rates and Bent Inner Plug.	60	1/E13
40.	Thrust Coefficient as a Function of Outer Nozzle Radius Ratio for High Inner Flow Rates and Bent Inner Plug.	61	1/E14
41.	Thrust Coefficient as a Function of Inner Nozzle Radius Ratio for Low Inner Flow Rates, $(R_r)_o = 0.902$ .	62	1/F1
42.	Thrust Coefficient as a Function of Inner Nozzle Radius Ratio for Low Inner Flow Rates, $(R_r)_o = 0.853$ .	63	1/F2
43.	Static Pressure Distribution, Configuration 2 [ $(R_r)_o = 0.902$ , $(R_r)_i = 0.8$ , Conical Inner Plug] with Zero Inner Flow.	65	1/F4
44.	Static Pressure Distribution, Configuration 3 [ $(R_r)_o = 0.902$ , $(R_r)_i = 0.902$ , Conical Inner Plug] with Zero Inner Flow.	66	1/F5
45.	Integrated Inner Plug Pressure Force as a Function of Inner Nozzle Radius Ratio for Low Inner Flow Rates.	67	1/F6
46.	Thrust Coefficient as a Function of Inner Nozzle Radius Ratio for High Inner Flow Rates, $(R_r)_o = 0.902$ .	68	1/F7
47.	Thrust Coefficient as a Function of Inner Nozzle Radius Ratio for High Inner Flow Rates, $(R_r)_o = 0.853$ .	69	1/F8



# LIST OF ILLUSTRATIONS (Continued)

<u>Figure</u>		<u>Page</u>	
48.	Thrust Coefficient as a Function of Inner Weight Flow for Low Inner Flow Rates, $M_a = 0$ .	70	1/F9
49.	Thrust Coefficient as a Function of Inner Weight Flow for Low Inner Flow Rates, $M_a = 0.36$ .	71	1/F10
50.	Static Pressure Distributions, Configuration 6 [( $R_r$ ) <sub>0</sub> = 0.926, ( $R_r$ ) <sub>1</sub> = 0.8, Conical Inner Plug] for Low Inner Flow Rates.	73	1/F12
51.	Thrust Coefficient as a Function of Inner Nozzle Pressure Ratio for High Inner Flow Rates, $M_a = 0$ .	74	1/F13
52.	Thrust Coefficient as a Function of Inner Nozzle Pressure Ratio for High Inner Flow Rates, $M_a = 0.36$ .	75	1/F14
53.	Inner Plug Integrated Pressure Force as a Function of Inner Nozzle Pressure Ratio for High Inner Flow Rates.	76	1/G1
54.	Static Pressure Distributions, Configurations 2 and 4, High Inner Flow, $P_{T1}/P_a = 1.1$ .	77	1/G2
55.	Static Pressure Distributions, Configurations 2 and 4, High Inner Flow, $P_{T1}/P_a = 2.5$ .	78	1/G3
56.	Static Pressure Distributions, Configurations 2 and 4, High Inner Flow, $P_{T1}/P_a = 3.5$ .	79	1/G4
57.	Thrust Coefficient as a Function of Tunnel Mach Number for Low Inner Flow Rates.	81	1/G6
58.	Inner Plug and Outer Plug Integrated Pressure Forces as a Function of Tunnel Mach Number for Low Inner Flow Rates, [( $R_r$ ) <sub>0</sub> = 0.902, ( $R_r$ ) <sub>1</sub> = 0.8].	82	1/G7
59.	Inner Plug and Outer Plug Integrated Pressure Forces as a Function of Tunnel Mach Number for Low Inner Flow Rates, [( $R_r$ ) <sub>0</sub> = 0.853, ( $R_r$ ) <sub>1</sub> = 0.8].	83	1/G8
60.	Shroud Drag as a Function of Tunnel Mach Number for Low Inner Flow Rates.	84	1/G9
61.	Thrust Coefficient as a Function of Tunnel Mach Number for High Inner Flow Rates.	86	1/G11

# LIST OF ILLUSTRATIONS (Concluded)

<u>Figure</u>		<u>Page</u>	
62.	Outer Nozzle Flow Coefficients.	87	1/G12
63.	Inner Nozzle Flow Coefficients for Configuration 1 [ $(R_r)_0 = 0.902$ , $(R_r)_1 = 0.673$ , Bent Inner Plug].	88	1/G13
64.	Inner Nozzle Flow Coefficients for Configuration 2 [ $(R_r)_0 = 0.902$ , $(R_r)_1 = 0.8$ , Conical Inner Plug].	89	1/G14
65.	Inner Nozzle Flow Coefficients for Configuration 3 [ $(R_r)_0 = 0.902$ , $(R_r)_1 = 0.902$ , Conical Inner Plug].	90	2/A7
66.	Inner Nozzle Flow Coefficients for Configuration 4 [ $(R_r)_0 = 0.902$ , $(R_r)_1 = 0.8$ , Bent Inner Plug].	91	2/A8
67.	Inner Nozzle Flow Coefficients for Configuration 5 [ $(R_r)_0 = 0.853$ , $(R_r)_1 = 0.8$ , Conical Inner Plug].	92	2/A9
68.	Inner Nozzle Flow Coefficients for Configuration 6 [ $(R_r)_0 = 0.926$ , $(R_r)_1 = 0.8$ , Conical Inner Plug].	93	2/A10
69.	Inner Nozzle Flow Coefficients for Configuration 7 [ $(R_r)_0 = 0.853$ , $(R_r)_1 = 0.902$ , Conical Inner Plug].	94	2/A11
70.	Inner Nozzle Flow Coefficients for Configuration 8 [ $(R_r)_0 = 0.853$ , $(R_r)_1 = 0.8$ , Bent Inner Plug].	95	2/A12
71.	Measured Static Pressure Distribution with Unchoked Outer Nozzle, Configuration 2, Low Inner Flow.	96	2/A13

APR 28 1978

Item No. 830-----14

NAS1.26: 2990

NASA Contractor Report 2990

COMPLETED

ORIGINAL

# Wind Tunnel Performance Tests of Coannular Plug Nozzles

Paul S. Staid

CONTRACT NAS3-19777  
APRIL 1978

**NASA**

NASA Contractor Report 2990

## Wind Tunnel Performance Tests of Coannular Plug Nozzles

Paul S. Staid  
*General Electric Company*  
*Cincinnati, Ohio*

Prepared for  
Lewis Research Center  
under Contract NAS3-19777



National Aeronautics  
and Space Administration

Scientific and Technical  
Information Office

1978

**BLANK PAGE**

## 1.0 SUMMARY

Previous programs have indicated potential combined acoustic and aerodynamic performance advantages for dual-flow plug nozzles applicable to supersonic cruise aircraft during takeoff operation. The General Electric Company, under contract to the NASA Lewis Research Center, conducted design and scale model test studies which investigated the effects of key design parameters on the aerodynamic and acoustic characteristics of such an exhaust system. The performance tests, reported in this document, were conducted in the NASA Lewis 8 x 6 foot supersonic wind tunnel. The test conditions were commensurate with takeoff and low-speed flight regimes - ambient Mach numbers from 0 to 0.45, outer stream pressure ratios of 1.5 to 3.5, and inner stream pressure ratios from 1.1 to 3.5. In addition, low or bleed flow rates from zero to 6% of the outer stream weight-flow were run on the inner nozzle. The model geometric variables were the radius at which the outer exhaust stream was located (termed "radius ratio", i.e., the ratio of the diameters of the inside to the outside flowpaths at the nozzle throat), the inner stream radius ratio, and the inner plug surface contour.

Thrust coefficients for the high inner flow rate tests varied between 0.95 and 0.974 for the eight configurations running at an external Mach number of 0.36 with an outer nozzle pressure ratio of 2.5, representative of takeoff operating conditions. The primary parameters influencing the performance level in these instances were the outer nozzle radius ratio and the inner plug contour. Increasing outer radius ratio from 0.853 to 0.926 resulted in a 1-2% loss in performance. Of the two inner plug contours tested, the conical plugs with smooth contours exhibited as much as a 1.5% performance advantage at high inner pressure ratios over the plugs having an abrupt angular change downstream of the throat.

Thrust coefficients with low inner flow rates ranged from 0.88 to 0.97 at Mach 0.36 and an outer nozzle pressure ratio of 2.5. The outer nozzle radius ratio was the predominant factor determining these levels, decreasing the coefficients by 6% in going from 0.853 to 0.926. Performance levels

increased 2-3% as the inner bleed flow was raised from 0 to 6% of the outer flow rate. Decreasing inner nozzle radius ratio also increased thrust by approximately 2%.

## 2.0 INTRODUCTION

A previous program conducted under NASA Lewis contract NAS3-18008 has indicated that plug nozzles with two coannular exhaust streams exhibit favorable jet noise characteristics. These exhaust systems, operating at conditions representative of takeoff power settings for supersonic cruise aircraft, generate less exhaust noise than other nozzle types - such as round nozzles with single exhaust streams. The potential exists for utilizing these characteristics to produce an engine sufficiently quiet to negate the necessity of a mechanical jet noise suppressor. Such a system would realize benefits in exhaust system weight, simplicity, and performance.

The original program investigated only a single nozzle configuration over a limited range of operating conditions. A subsequent program under contract NAS3-19777 was contracted to extend these studies in order to provide a basic understanding and the design data needed for the continuing evaluation of these engine/exhaust system designs. The primary parameters considered capable of influencing the combined acoustic and aerodynamic performance were (1) the radius at which the outer exhaust stream was located (designated by the term "radius ratio" - the ratio of the diameters of the inside of the flowpath to the outside of the flowpath at the nozzle throat), (2) the inner exhaust stream radius ratio, and (3) the relative velocities or flow rates of the two streams. Acoustic and aerodynamic test models were designed to be modular in nature so that aspects of the geometry could be varied independently, thereby isolating the effect of key parameters.

The aerodynamic performance tests were run in the NASA Lewis 8 x 6 foot supersonic wind tunnel. Data were taken over a range of inner and outer stream pressure ratios representative of takeoff conditions with tunnel Mach numbers of 0, 0.36, and 0.45. The performance test program and its results are presented in this report.



## 2.1 LIST OF SYMBOLS

$A$	area
$A_1$	inner nozzle throat area
$A_o$	outer nozzle throat area
$C_D$	drag coefficient
$C_f$	flow coefficient
$C_T$	thrust coefficient
$D$	drag
$DM$	sting diameter
$F$	nozzle thrust
$F_{AS}$	axial force of air supply tubes
$F_{LC}$	load cell axial force
$F_P$	pressure forces
$f_g$	dimensionless stream thrust parameter
$K$	critical flow factor
$K_{v_1}$	inner venturi calibration constant
$M$	Mach number
$m$	known value of any quantity
$n$	number of measured samples of any quantity
$P$	pressure
$RN$	Reynolds number
$(R_r)_1$	inner nozzle radius ratio
$(R_r)_o$	outer nozzle radius ratio
$T$	temperature
$V$	velocity
$W$	mass flow rate
$\bar{X}$	mean of measured values
$X_1$	individual sample
$\Delta A$	incremental projected area
$Y$	ratio of specific heats

## 2.1 LIST OF SYMBOLS (Concluded)

### Subscripts

a	ambient
c	cylindrical surface of metric sting
f	friction
I	ideal
i	inner
o	outer
T	total
V	venturi
9	STA <sup>(1)</sup> nozzle exit station
1 - 4	control volume surfaces

### Superscripts

*	critical flow condition (at Mach number = 1.0)
---	--

(1) Supersonic Tunnel Association

### 3.0 TEST FACILITY DESCRIPTION

The test program was conducted in the NASA Lewis 8 x 6 foot supersonic wind tunnel. The test nozzles were mounted to a 21.59 cm (8.5 in.) diameter cylindrical sting which was supported in the test section by a perpendicular strut connected to the tunnel ceiling. A schematic illustrating the model system is shown in Figure 1. Air was supplied to the model through tubes running down the strut and emptying into coannular air passages which carried the air aft to the model. The air source was a continuous supply of  $310.28 \text{ N/cm}^2$  (450 psig) compressor air which passed through a system of control valves, flowmeters, and into the strut. A schematic of the air supply system is shown in Figure 2. The outer nozzle air was metered through a choked venturi 3.1699 cm (1.248 in.) in diameter at the throat. The inner nozzle air supply was metered through either a 2.8951 cm (1.1398 in.) or 1.0122 cm (0.3985 in.) diameter choked venturi, depending on the flow rate required.

The nozzle thrust was measured with a load cell mounted in the forward portion of the sting. The coannular air passages in the sting were mounted to the load cell and were metric, i.e., forces felt by, and transmitted by, the air passages were measured by the load cell. The air supply tubes running down the strut were fixed to the tunnel ceiling at the top, which was nonmetric (forces here were not felt by the load cell), and to the air passages at the bottom which were metric. These air supply tubes thus formed flexure columns bridging the nonmetric and metric portions of the test rig, creating a force which was accounted for in the balance calibration. Air flow from the tubes entered the sting perpendicular to the sting axis and thus created no entering momentum force on the load cell. The air passages themselves were suspended inside the sting with bearings which supported the concentric passages, but allowed the axial forces to be transmitted to the load cell. Static pressure instrumentation was located on the forward-facing portions of the internal metric hardware so that a tare force could be calculated in cases where internal static pressures were different from ambient (see Section 5.3).

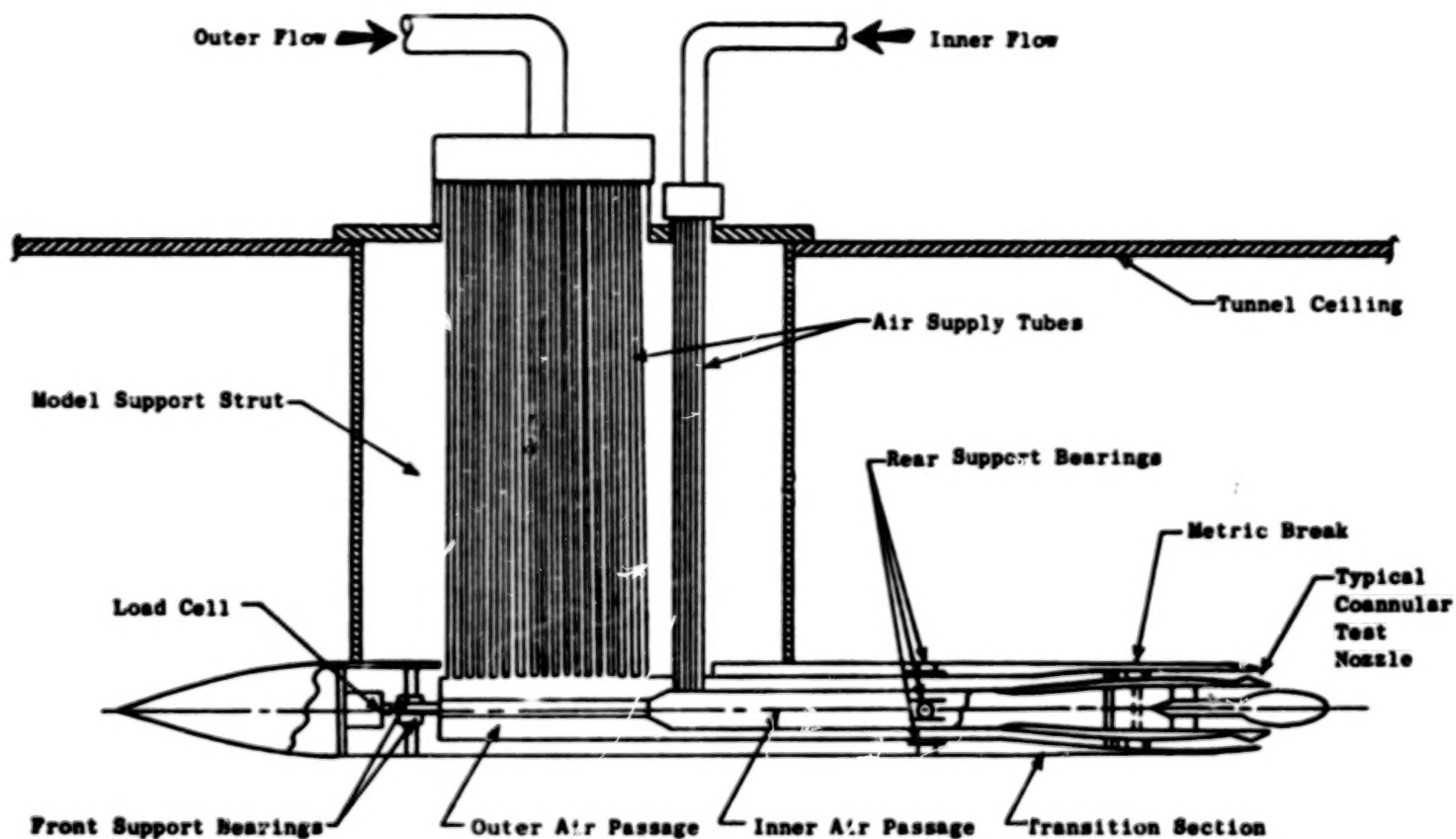


Figure 1. Schematic of Model System.

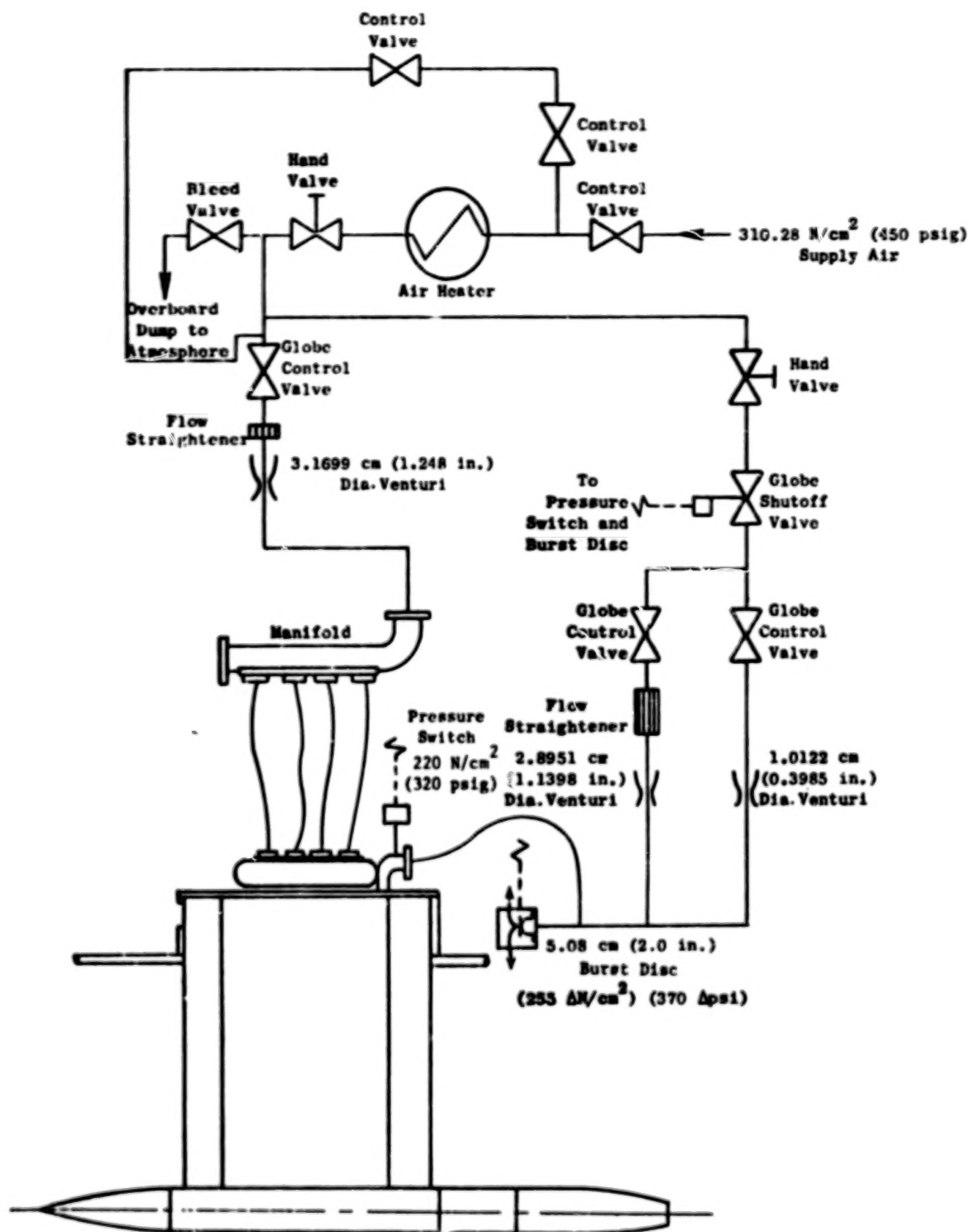


Figure 2. Schematic of Model Air Supply.

The load cell was calibrated by assembling the Supersonic Tunnel Association (STA) model on the sting and applying a known axial force along the center-line of the model and the load cell. This known force was generated by a hydraulic cylinder connected to a circular pad which butted-up against the STA nozzle exit with the shaft of the hydraulic cylinder pushing at the axis of the nozzle in an axial direction. The correlation of the known applied force and the millivolt output of the load cell comprised the desired calibration. The calibration was made from 0 to 4458 newtons (1000 lbs.), the maximum allowable balance load.

#### 4.0 MODEL DESCRIPTION

A schematic of the eight model configurations assembled on the sting is shown in Figure 3. Adapters connected the model flowpaths with the inner and outer air supply passages. The nozzle total pressure and temperature measurements were made with instrumentation rakes downstream of flow conditioners (choked plates and screens) which assured a flat total-pressure profile for an accurate measurement. The outer diameter of the models was 20.32 cm, (8.0 in.), which required a reduction from the 21.59 cm (8.5 in.) sting diameter. This reduction was made via a fairing attached to the sting and was therefore nonmetric (not connected to the load cell). The metric break (the separation between the metric and nonmetric portion of the system) was provided by a gap of approximately 0.127 cm (0.05 in.) between the end of the fairing and model shrouds, which were attached to the air supply passages, as shown in Figure 3.

Schematics of the eight model configurations are shown in Figures 4 and 5. The principal nozzle design variables were inner- and outer-nozzle radius ratio and the inner plug geometry. Two inner plug geometries were tested: "conical" plugs which had a constant plug angle from the radius at the crown of the plug aft to the tip radius (Configurations 2, 3, 5, 6 and 7); and "bent" plugs which had an abrupt angle change partway down the plug (Configurations 1, 4, and 8). The two conical plugs had a 2.415 cm (0.951 in.) radius of curvature at the crown of the plug, a 15° plug angle, and a 2.08 cm (0.819 in.) radius circular-arc plug tip. The two bent plugs were the same as the conical plugs with the exception that the initial plug angle downstream of the throat was 2.8° and changed abruptly to 15°.

The inner nozzle radius ratio was varied by using inner plugs with different diameters at the crown: the outer surface of the inner stream remained fixed. The outer nozzle radius ratio was varied by changing the shroud, with the outer plug geometry remaining the same. All three radius ratio shrouds had cylindrical inner surfaces extending from some distance upstream of the nozzle throat aft to the trailing edge. As a consequence of varying the outer radius ratio in this manner, the amount of boattail area and the boattail angle in-

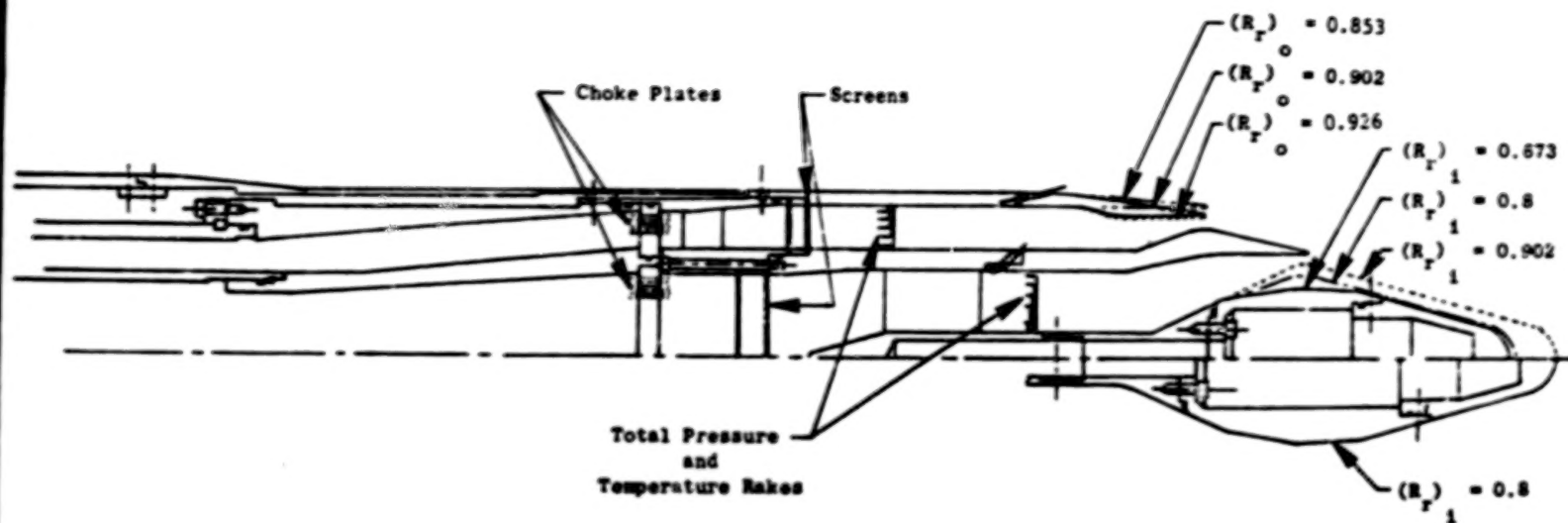
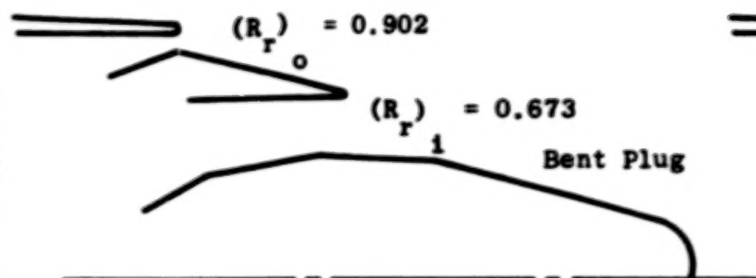


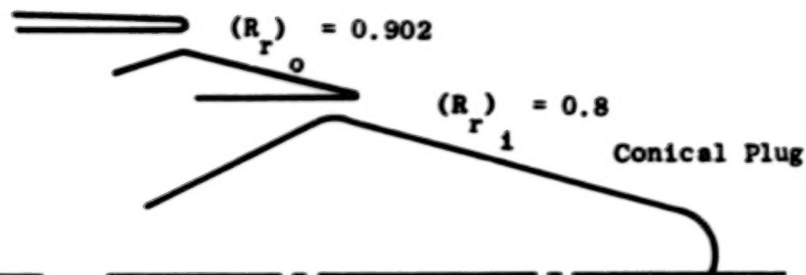
Figure 3. Schematic of Model Assembly.



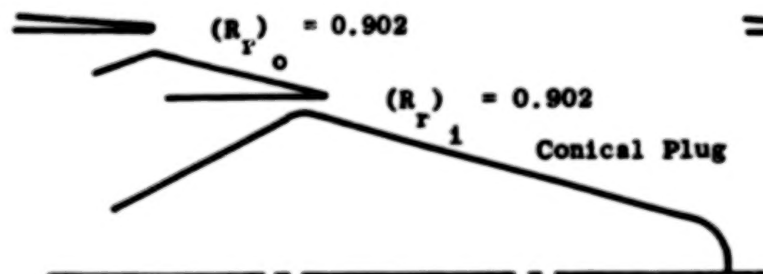
Configuration No. 1



Configuration No. 2



Configuration No. 3



Configuration No. 4

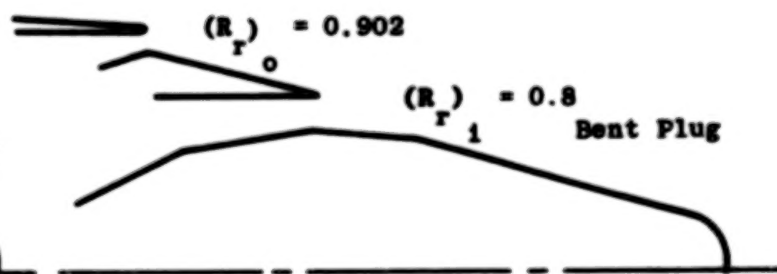
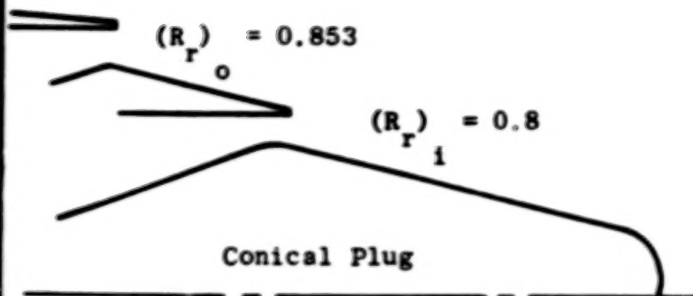
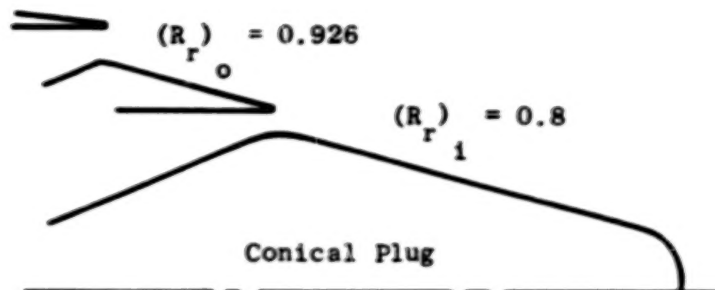


Figure 4. Model Schematics, Configurations 1-4.

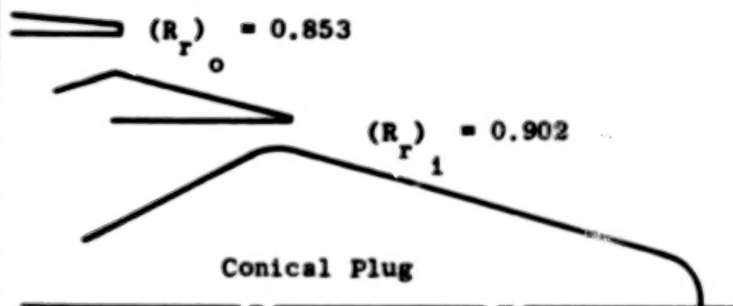
Configuration No. 5



Configuration No. 6



Configuration No. 7



Configuration No. 8

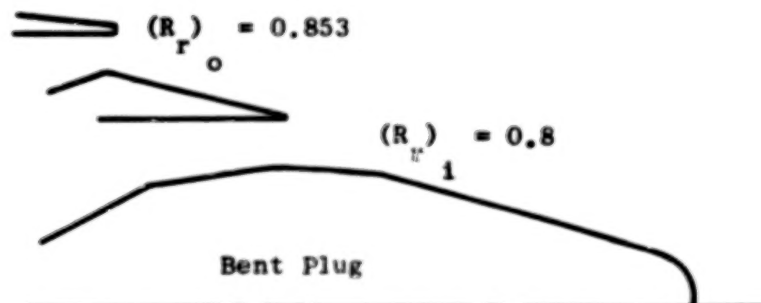


Figure 5. Model Schematics, Configurations 5-8.

creased and the outer nozzle throat area decreased as the radius ratio increased. A circular arc of 15.24 cm (6.0 in.) was used on all three shrouds in transitioning the outer surface from the 20.32 cm (8.0 in.) diameter cylindrical sting to the conical boattail angle. A table summarizing the key model parameters is given below.

Configuration Number	$(R_r)_o$	$(R_r)_i$	$A_o^* \text{ cm}^2 (\text{in.}^2)$	$A_i^* \text{ cm}^2 (\text{in.}^2)$	Inner Plug Geometry	Shroud Boattail Angle ( $^\circ$ )
1	0.902	0.673	45.451 ( 7.045)	70.819 (10.977)	Bent	8.0
2	0.902	0.8	45.451 ( 7.045)	46.684 ( 7.236)	Conical	8.0
3	0.902	0.902	45.451 ( 7.045)	24.181 ( 3.748)	Conical	8.0
4	0.902	0.8	45.451 ( 7.045)	46.684 ( 7.236)	Bent	8.0
5	0.853	0.8	74.232 (11.506)	46.684 ( 7.236)	Conical	4.5
6	0.926	0.8	32.968 ( 5.110)	46.684 ( 7.236)	Conical	9.7
7	0.853	0.902	74.232 (11.506)	24.181 ( 3.748)	Conical	4.5
8	0.853	0.8	74.232 (11.506)	46.684 ( 7.236)	Bent	4.5

In addition to the eight plug-nozzle model configurations, a Supersonic Tunnel Association (STA) model was also tested as a means of verifying the facility accuracy. A sketch of the STA model attached to the model support is shown in Figure 6. The throat diameter of this nozzle was 10.16 cm (4.0 in.) with the remaining dimensions scaled to this diameter as presented in Reference 1.

The plug nozzle model flow surfaces were instrumented with static pressure taps. Each shroud contained 12 external taps spaced axially, starting on the cylindrical section slightly upstream of the boattail arc and continuing aft to the tip of the shroud. The outer plug was instrumented with 13 static taps axially located on the outer surface starting from slightly upstream of the crown plug and running down to near the plug tip. The inner plug was instrumented with either 18, 19, or 20 taps, depending on the configuration, which were distributed axially from slightly upstream of the plug crown to the tip of the plug.

Photographs of several of the models and the STA nozzle assembled in the wind tunnel are shown in Figures 7 through 12. Detailed drawings of the model and adapter hardware are presented in Reference 2.

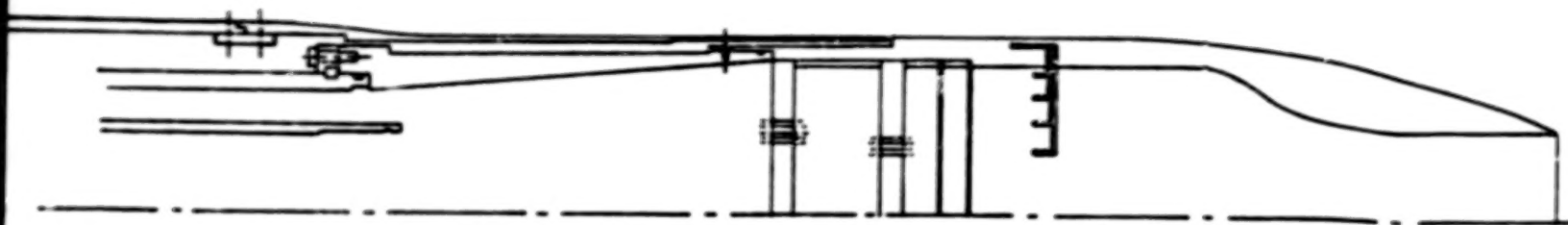


Figure 6. Supersonic Tunnel Association Model Assembly.

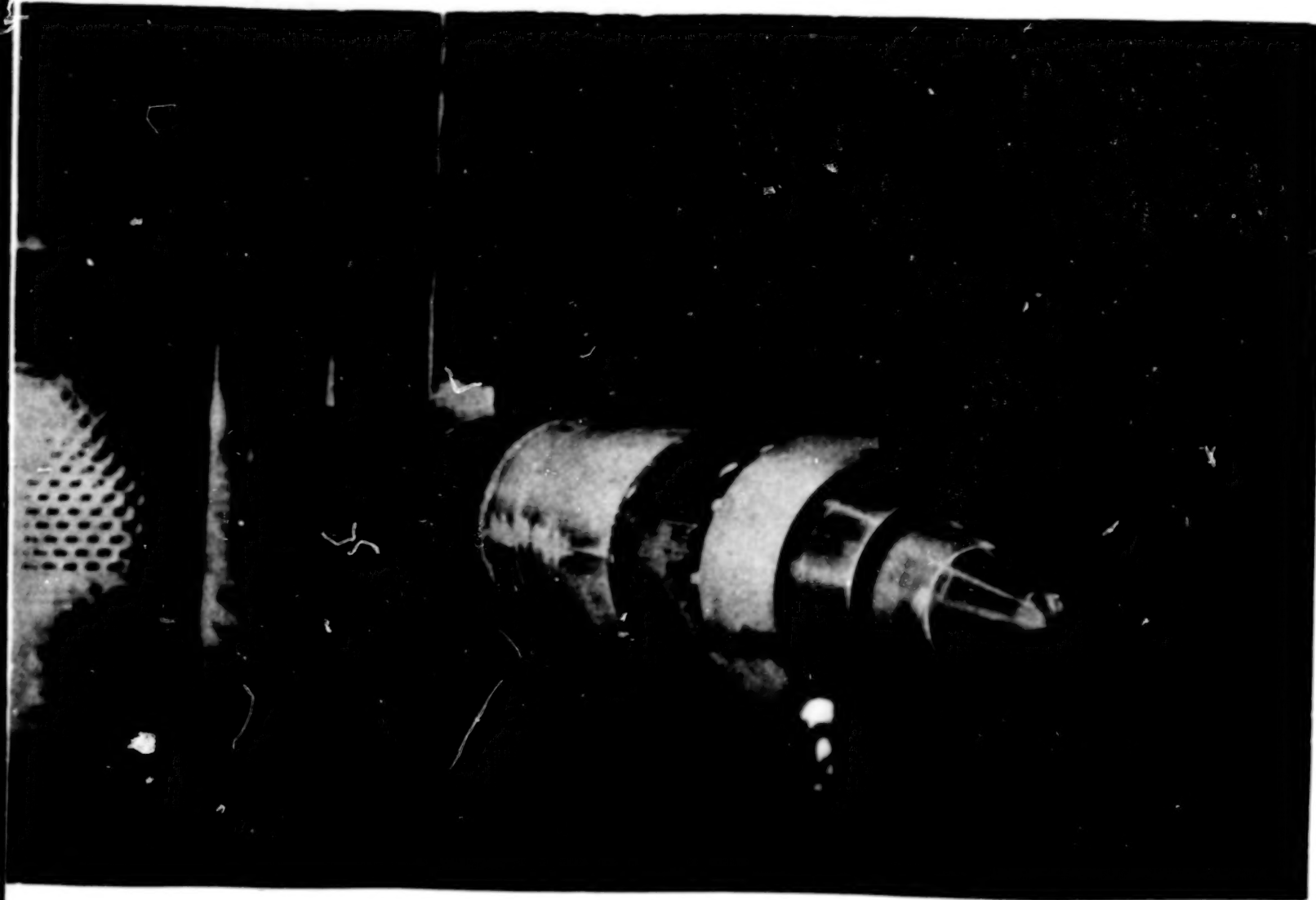


Figure 7. Configuration 2 Mounted in NASA Tunnel.

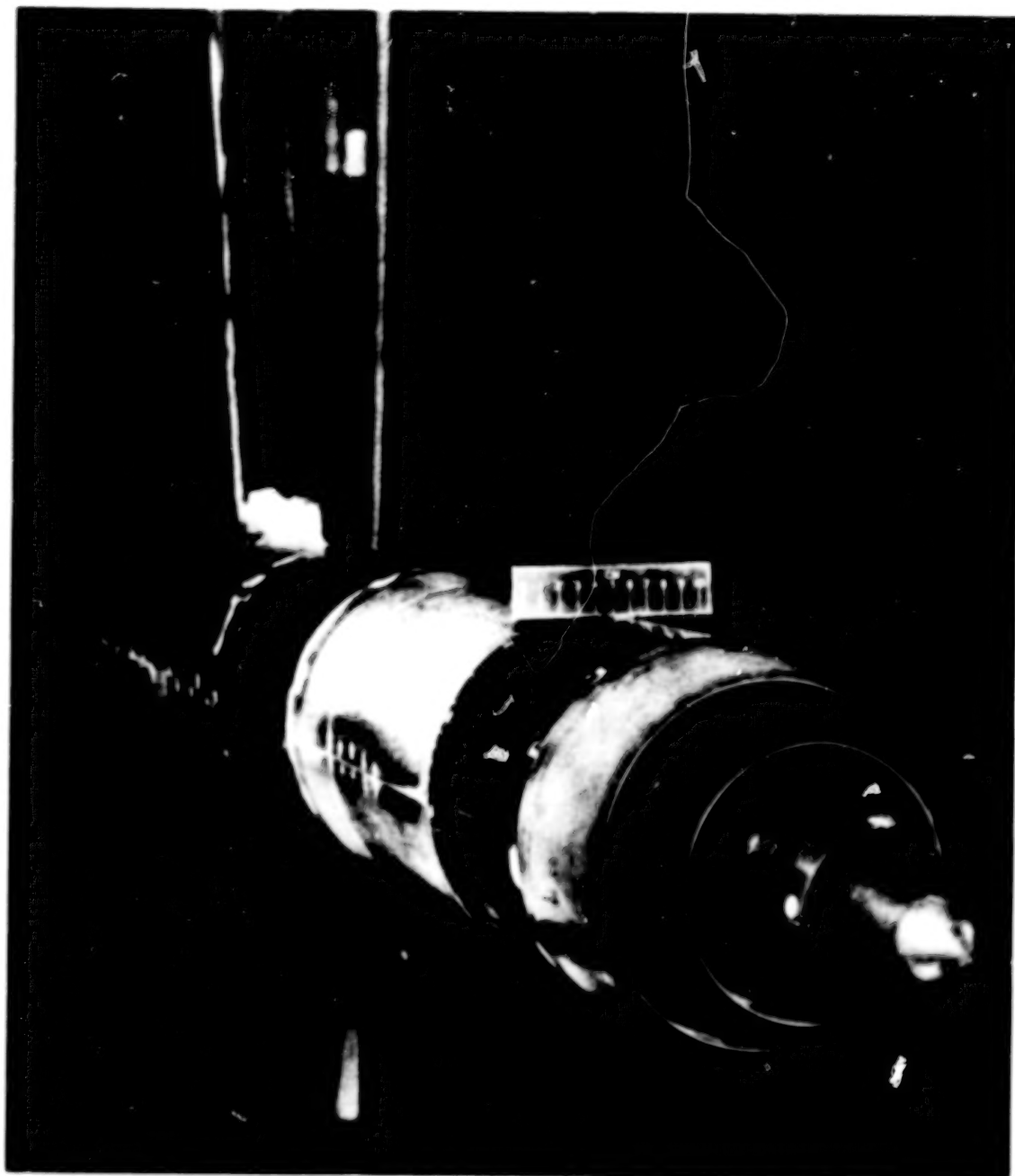


Figure 8. Configuration 4 Mounted in NASA Tunnel.

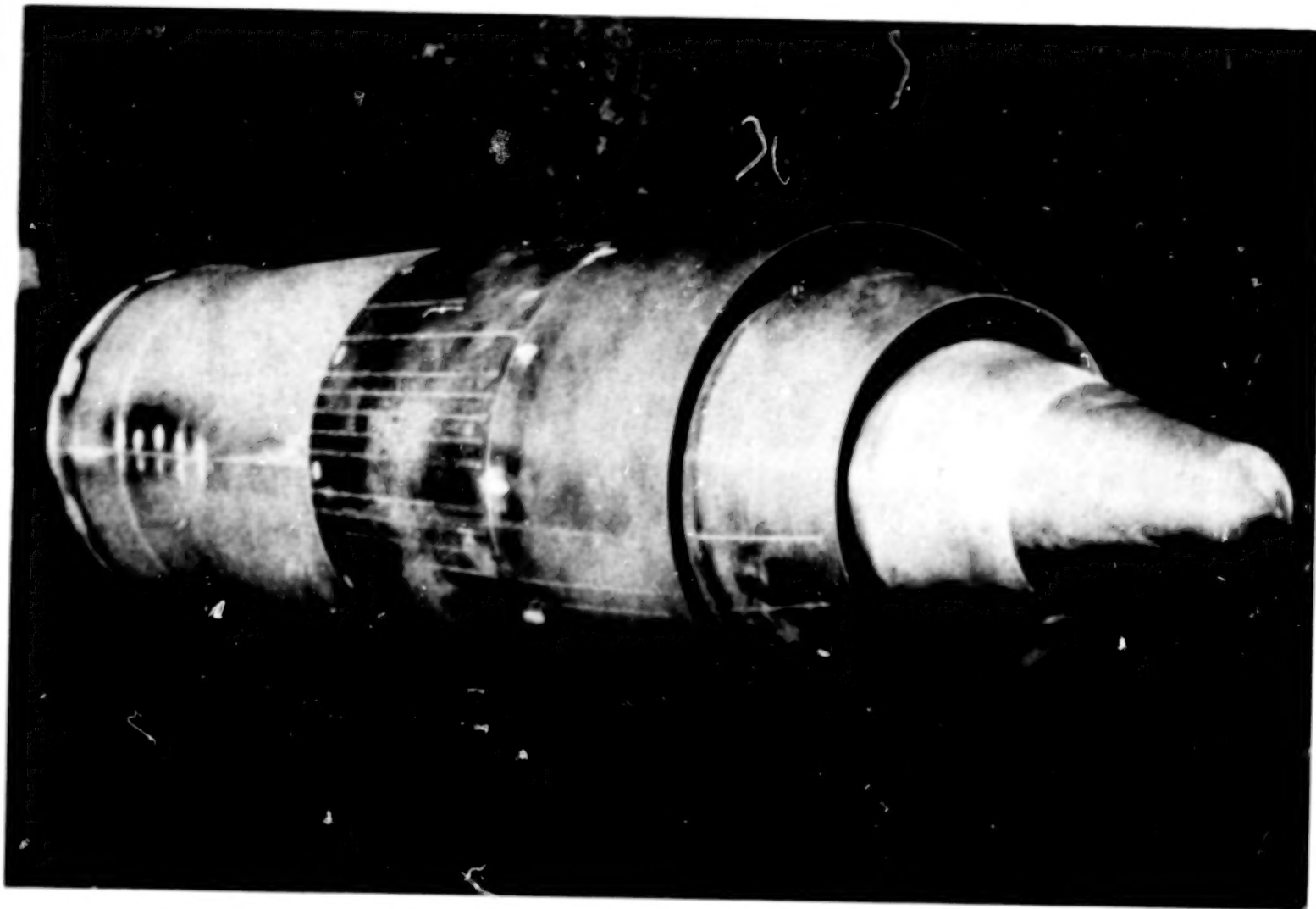


Figure 9. Configuration 5 Mounted in NASA Tunnel.



Figure 10. Configuration 6 Mounted in NASA Tunnel.



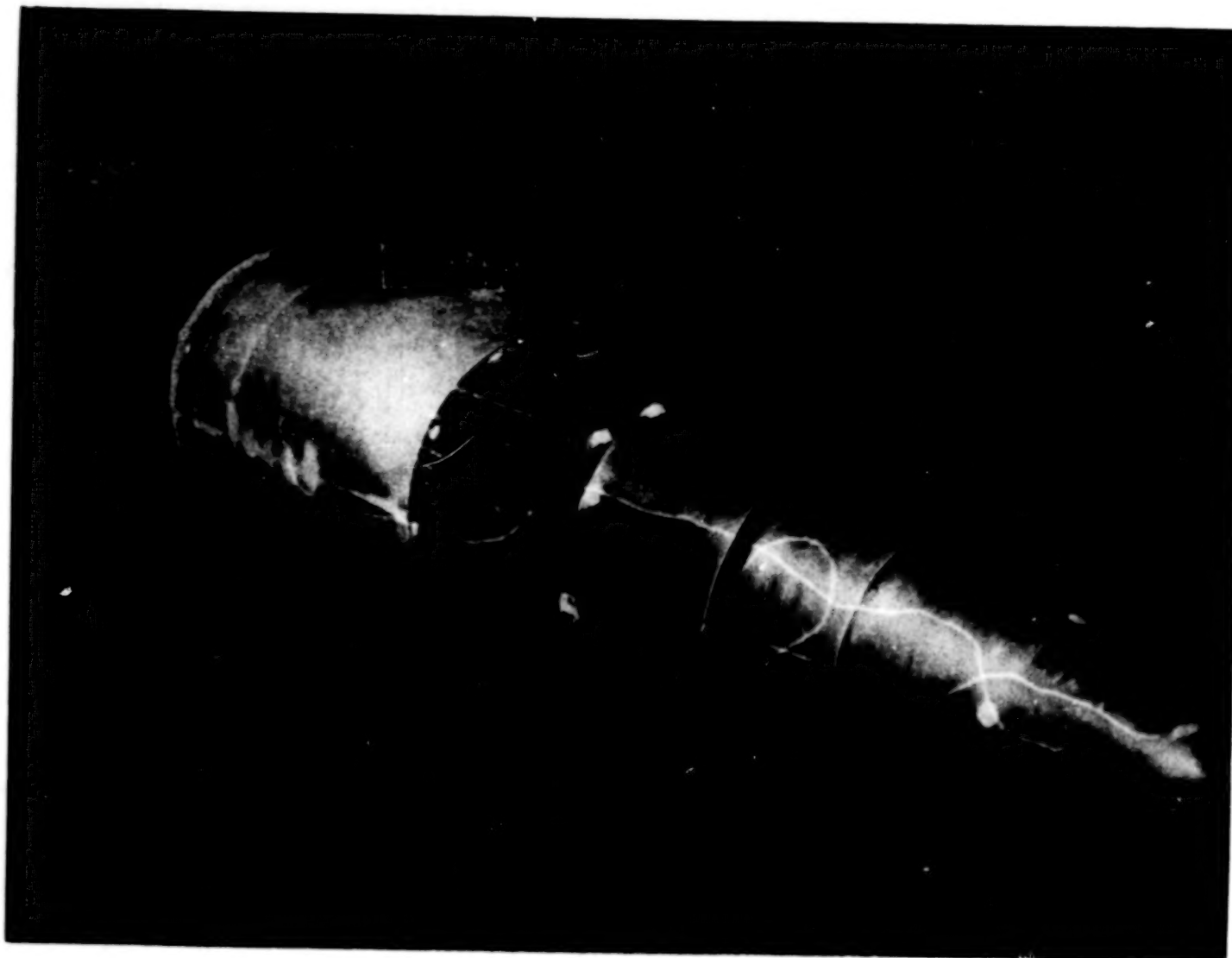


Figure 11. Configuration 7 Mounted in NASA Tunnel.

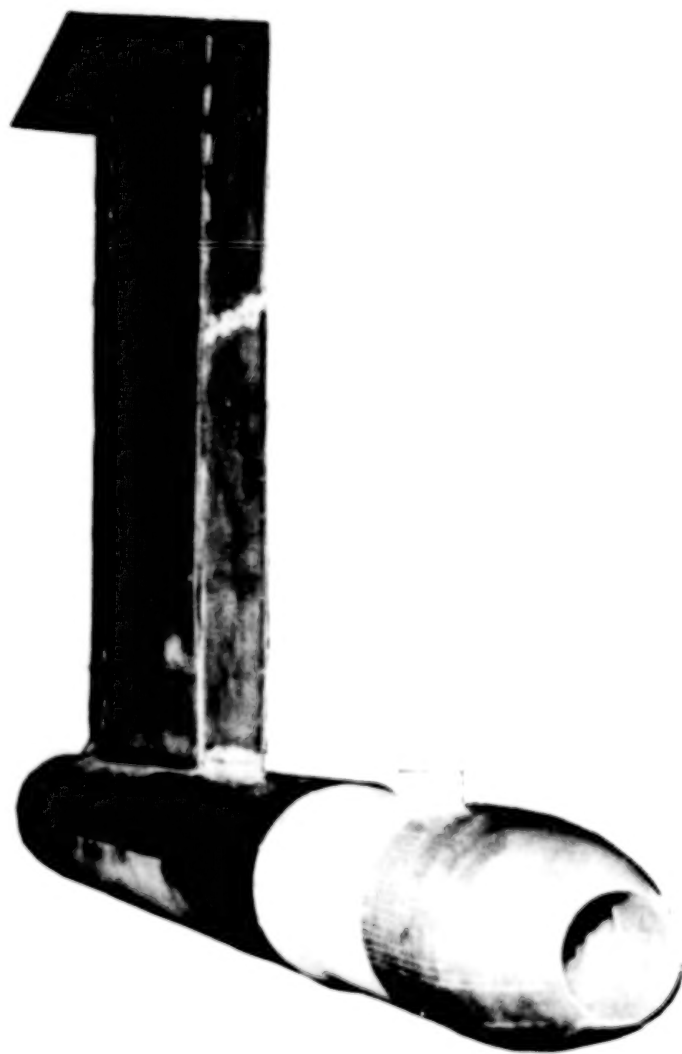


Figure 12. STA Nozzle on NASA Tunnel Mount.

## 5.0 DATA REDUCTION PROCEDURES

General descriptions of the methods used to determine model flow rates and nozzle thrust are contained in the following subsections. A more extensive detailing of the data reduction procedures is included in the appendix.

### 5.1 FLOW RATES

The mass flow through the outer nozzle was measured with a 3.1699 cm (1.248 in.) throat diameter choked venturi meter, located as shown in Figure 2. The flow rate was calculated using the measured gas total temperature and pressure,  $T_{T_{V_o}}$  and  $P_{T_{V_o}}$ , respectively, and the equation:

$$\dot{W}_o = C_{D_{V_o}} \frac{K_{V_o} P_{T_{V_o}} A_{V_o}}{\sqrt{T_{T_{V_o}}}} \quad (1)$$

where  $C_{D_{V_o}}$  is the venturi flow coefficient. The critical flow factor,  $K_{V_o}$ , was calculated as a function of total pressure and temperature to account for real gas effects as given in Reference 3.

The mass flow through the inner nozzle was measured with either of two choked venturi meters located as shown in Figure 2. The flow for high inner flow rates was measured using the 2.8951 cm (1.1398 in.) throat diameter venturi. The flow for the low inner flow rate testing was measured with the 1.0122 cm (0.3985 in.) throat diameter venturi. For both meters, the flow rate was computed from a calibration of the meters made by the manufacturer utilizing the measured venturi pressure and total temperature.

## 5.2 FLOW COEFFICIENTS

The flow coefficient of a nozzle is defined as the ratio of actual mass flow rate through the nozzle to the ideal isentropic flow rate at the temperature and pressure of the flow:

$$C_D = \frac{\text{measured } W}{\text{ideal } W} \quad (2)$$

The ideal weight flow for the outer nozzle was calculated from the relation

$$W_{I_o} = \frac{K_o A_o P_{T_o}}{\sqrt{T_{T_o}}} \frac{A^*}{A_o} \quad (3)$$

where  $A_o$ ,  $P_{T_o}$ , and  $T_{T_o}$  are the outer nozzle physical throat area, total pressure and total temperature, respectively. The critical flow factor,  $K_o$ , was corrected for real gas effects;  $A^*/A_o$  is the ratio of the flow area at sonic conditions to the outer nozzle throat area ( $A^*/A_o = 1.0$  for values of nozzle pressure ratios greater than 1.8929).

The inner nozzle ideal weight flow was calculated in identical fashion as the outer nozzle, but using the inner nozzle throat area and the inner flow pressure and temperature. For the low inner flow testing, the inner nozzle total pressures required to supply the low flow rates were generally lower than ambient pressure due to the pumping effect of the outer flow. In these cases, the ideal flow rate and flow coefficients are meaningless and were not calculated.

### 5.3 THRUST MEASUREMENTS

The thrust of the exhaust nozzles is defined as the axial exit momentum of the exhaust flow, plus the excess of exit pressure over ambient pressure times the exit area normal to the axis, minus the axial drag on the nozzle external surface, i.e.,

$$F = \int_{A_{\text{exit}}} d(WV)_{\text{axial}} + \int_{A_{\text{exit}}} (P - P_a) dA - D_{\text{external}} \quad (4)$$

The external drag consists of both the pressure drag on the boattail surface and the axial component of skin friction. Figure 13 shows a control volume applied to the test nozzles. Writing the momentum equation in the axial direction for this control volume demonstrates how the thrust was measured for the tests:

$$F = F_{LC} + F_{AS} + A_1(P_1 - P_a) + A_2(P_2 - P_a) + A_3(P_3 - P_a) + A_4(P_4 - P_a) \quad (5)$$

where  $F_{LC}$  is the axial force applied to the load cell and  $F_{AS}$  is the axial force applied at the boundary of the control volume by the air supply tubes. The static pressures  $P_1$ ,  $P_2$ ,  $P_3$ , and  $P_4$  were measured with static taps at each of the four areas (Figure 13). The force measuring system was calibrated by applying known forces and correlating this force against the load cell output, as previously described in Section 3.0.

An adjustment was made to the measured thrust to account for external friction drag on the cylindrical section upstream of the nozzle shroud. The axial force on this 20.32 cm (8.0 in.) diameter section, which extended from the metric-break to the attach-point of the nozzle shrouds, was not included in the nozzle net thrust. The friction drag was calculated by the equation:

$$D_f = \frac{\gamma}{2} P_a M_a^2 A_c C_f \quad (6)$$

where  $A_c$  is the wetted surface area of the cylindrical piece and  $C_f$  is the skin friction drag coefficient.

The thrust of the nozzles for this test was therefore given by

$$F = F_{LC} + F_{AS} + A_1(P_1 - P_a) + A_2(P_2 - P_a) + A_3(P_3 - P_a) + A_4(P_4 - P_a) + D_f \quad (7)$$

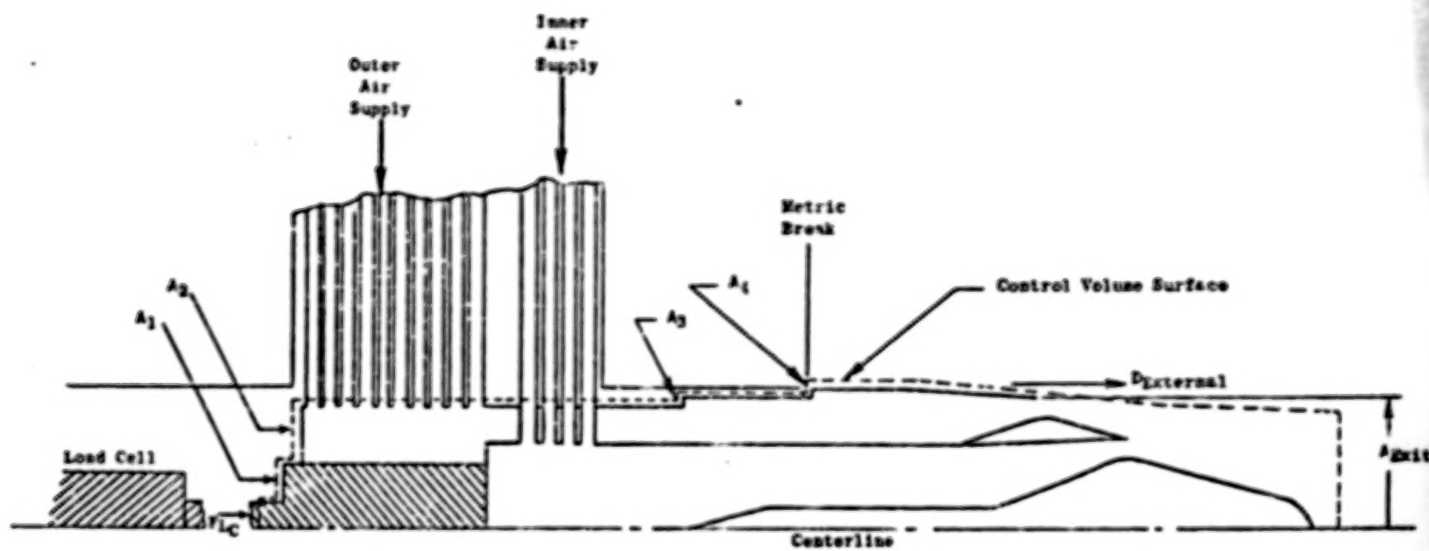


Figure 13. Control Volume Applied to Model Test Setup.

#### 5.4 THRUST COEFFICIENT

The thrust coefficient is the ratio of the measured nozzle thrust to the ideal thrust of the inner duct flow plus the ideal thrust of the outer duct flow. The ideal thrust for each stream equals the actual mass flow rate times the ideal velocity, i.e., the velocity of the stream expanded isentropically from the total pressure to the ambient pressure. The equation for the thrust coefficient is thus:

$$C_T = \frac{F}{W_o V_{I_o} + W_i V_{I_i}} \quad (8)$$

The ideal thrust for the nozzles was calculated using the dimensionless ideal-thrust function which is a function of only the nozzle pressure ratio.

During much of the low inner flow rate testing, the total pressure of the inner nozzle flow was lower than ambient. In these cases, the ideal thrust of the inner nozzle was set equal to zero.

For the static thrust tests of the STA model, a dimensionless stream-thrust parameter was also calculated as:

$$f_g = \frac{F + P_a A_g}{P_T A_g} \quad (9)$$

where  $A_g$  is the STA nozzle exit area.

#### 5.5 PRESSURE DATA

Total pressures in the models and static pressures on the model surfaces were measured with scanning value/transducer arrangements. The individual static pressure readings were also nondimensionalized by the ambient pressure. Axial pressure forces on the aft-facing portions of the shroud, outer plug, and inner plug were calculated by multiplying the difference between the static pressure at each tap and ambient by an incremental projected area represented by the particular tap and summing the products, i.e.,

$$F_p = \sum (P - P_a) \Delta A \quad (10)$$

These pressure forces were also nondimensionalized by the total ideal thrust of

the nozzle:

$$\frac{F_p}{W_1 V_{I_1} + W_o V_{I_o}}$$

(11)



## 6.0 TEST RESULTS AND DISCUSSION

### 6.1 DATA QUALITY

Prior to testing the plug nozzle models in the 8 x 6 foot tunnel, a Supersonic Tunnel Association (STA) model was run as a means of investigating the force and weight-flow measurement accuracy of the facility as built up for this test. The STA model assembly is shown in Figure 6, the model having a 10.16 cm (4.0 in.) diameter throat and a 20.32 cm (8.0 in.) maximum outside diameter, corresponding to the 20.32 cm (8.0 in.) maximum outside diameter of the plug nozzle models. Air could be supplied to the STA model using either the outer or inner flowpath as shown in the schematic of Figure 2. The tests were conducted with air supplied through either the 3.1699 cm (1.248 in.) diameter meter for the outer nozzle air supply or with air supplied by the larger of the two inner flowmeters, which was 2.8951 cm (1.1398 in.) in diameter. The smaller of the two inner flowmeters was not run with the STA model because sufficient air to choke the STA model could not be supplied. This did not compromise the completeness of the facility checkout with the STA nozzle because the small meter was used only to meter the flow for the low inner flow test points, where the flow rates ranged from 1% to 6% of the outer flow. Small errors in making this measurement could not affect the results.

The yardsticks against which the STA measurements were compared in order to determine the facility thrust and flow measurement accuracies were calculated values of STA thrust coefficient, flow coefficient, and dimensionless stream-thrust parameter for the static tests and previous measured values for wind-on testing. The calculated static values are derived from semiempirical methods of calculating standard ASME long radius nozzle performance, as described in Reference 4. These ASME equations are slightly modified to include the effect of a small difference in length of the internal flowpaths between the ASME and STA nozzles. The resulting equations, for nozzle pressure ratios equal to or greater than 1.89, are as follows:

$$C_D = 1 - 0.241 RN^{-0.2}$$

$$C_V = 1 - 0.143 RN^{-0.2}$$

(12)

$$f_g = G(1 + 1.4 C_D C_V)(0.52828)$$

where  $G = 1.00012 + 9.9112 \times 10^{-6} \times P_T$

and  $C_V$  is the peak thrust coefficient.

These methods are based on a large number of data and give the best possible determination of the actual static STA nozzle performance parameters. For the wind-on tests, the data are compared to previous results on the same STA model in the NASA Lewis 8 x 6 foot tunnel using different flowmetering and force measuring hardware. These previous tests are reported in Reference 5.

Comparisons of the measured static thrust and flow coefficients and stream-thrust parameter with the calculated values are shown in Figures 14 and 15 for the 3.1699 cm (1.248 in.) and 2.8951 cm (1.1398 in.) diameter meters, respectively. Figure 16 compares the measured thrust coefficient to previous test results at Mach numbers of 0.36, 0.40, and 0.45. Agreement between the measured values and the calculated or previously determined data is good, as is the repeatability of the data (5 to 8 static points and two wind-on points were taken at most nozzle pressure ratios). Repeatability of the wind-on data seemed to be better than the static data, possibly due to the increased tunnel vibration which would reduce hysteresis in the support bearings.

The number of repeat points taken at static conditions allowed a statistical evaluation of the data. Standard deviations and the bias of the mean value of the data from the "known" or calculated value were calculated by the following equations:

$$\text{Standard Deviation} = \sqrt{\frac{\sum (X_i - \bar{X})^2}{n - 1}} \quad (13)$$

$$\text{Bias} = \bar{X} - m$$

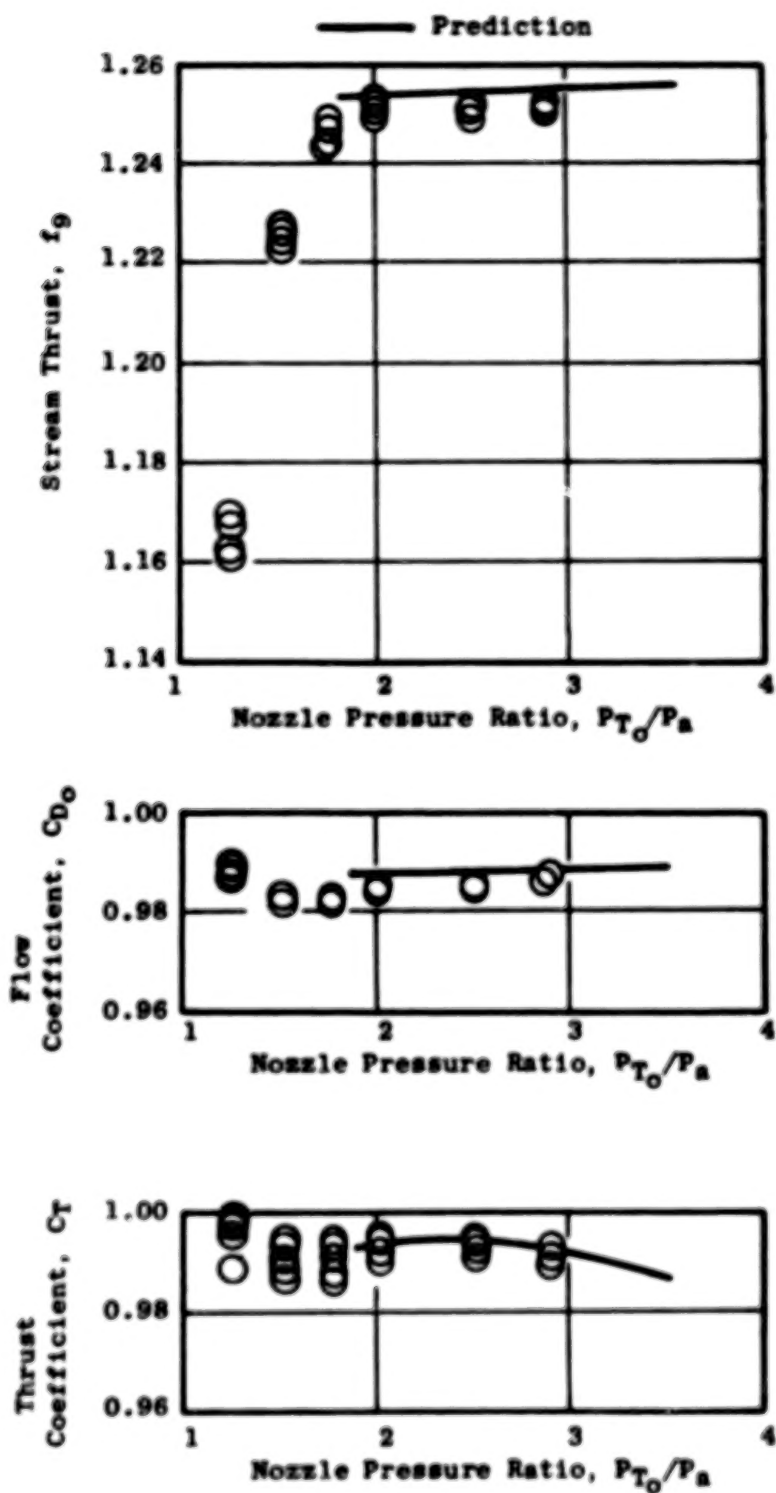


Figure 14. STA Static Performance with the 3.1699 cm (1.248 in.) Diameter Outer Flowmeter.

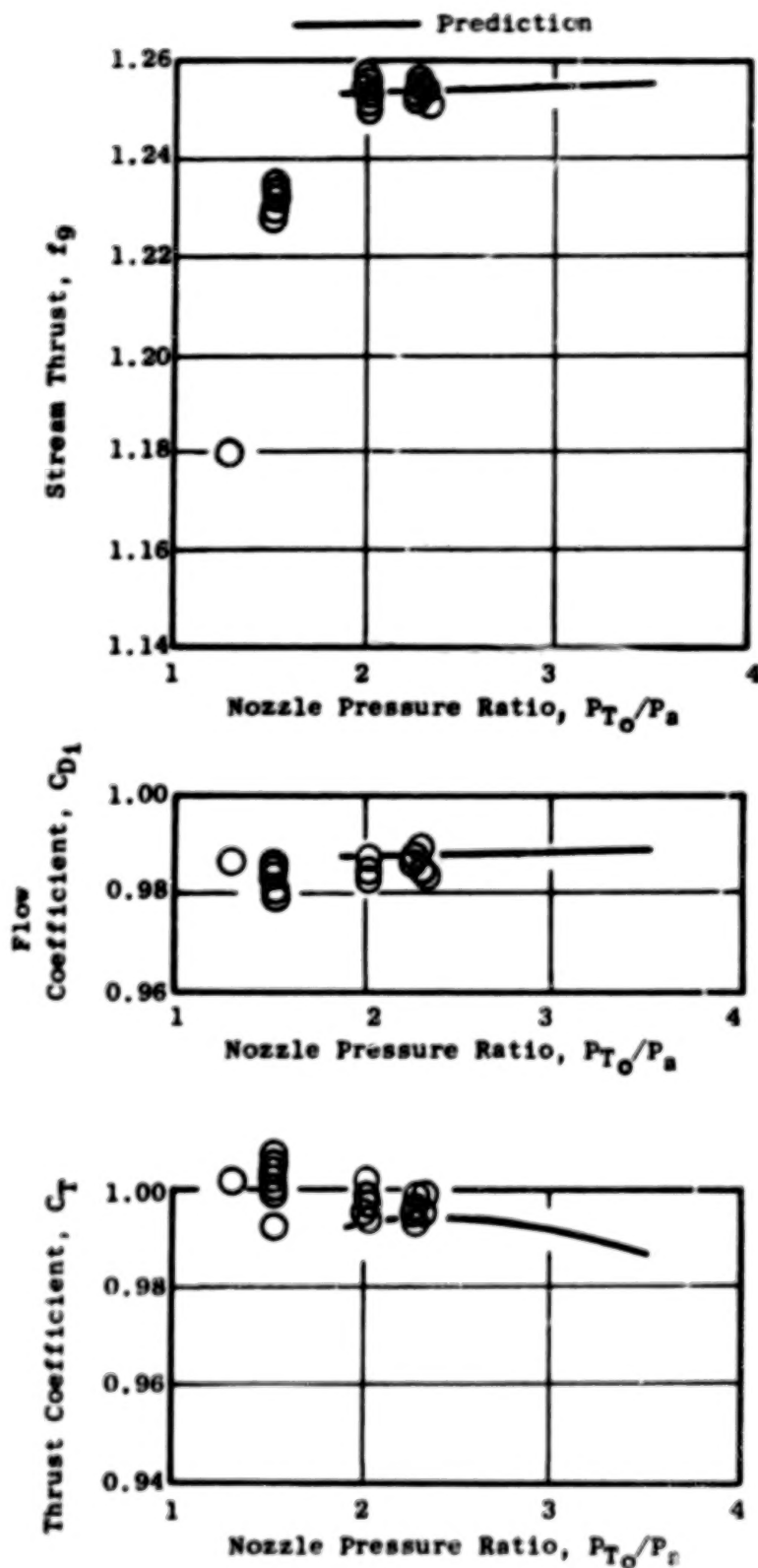


Figure 15. STA Static Performance with the 2.8951 cm (1.1398 in.) Diameter Inner Flowmeter.

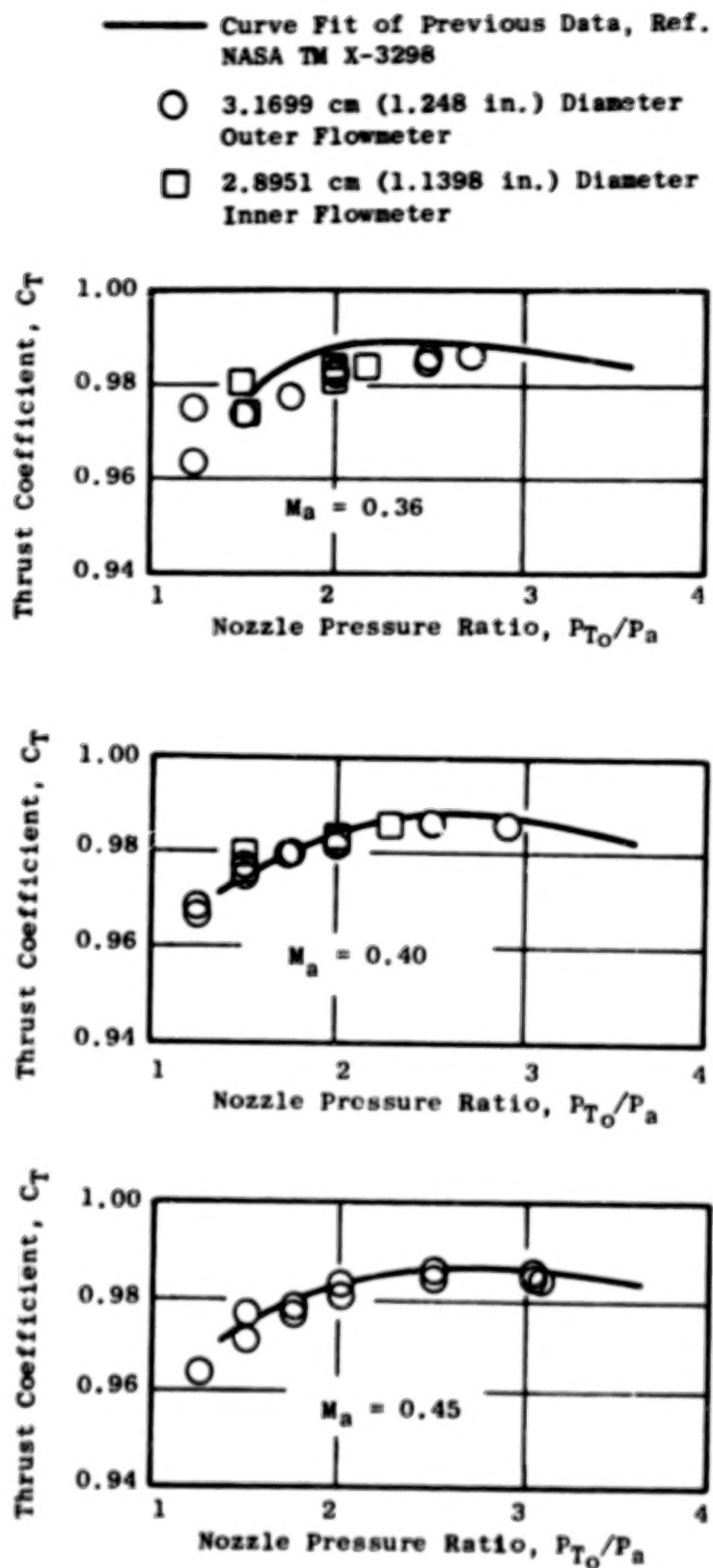


Figure 16. Wind-on STA Nozzle Thrust Coefficients.

where

$X_i$  = individual measured value of the parameter (e.g., thrust coefficient or flow coefficient)

$\bar{X}$  = mean of measured values of the parameter

$m$  = known value of parameter

$n$  = number of samples taken of the given parameter

Standard deviation calculations were made at each pressure ratio for which repeat points were taken. Bias calculations were made at each pressure ratio above 1.89 for which repeat points were taken, as the calculation procedure for the known values does not apply below this pressure ratio. The procedure for taking repeat points was to set each data point once in the order of increasing nozzle pressure ratio and then repeat each point going down in pressure ratio, the air shut off, and the process then repeated. In some instances either wind-on data or data using the other flowmeter were run in between repeating cycles.

The results of these calculations are shown in Figures 17 and 18 for the thrust coefficient and flow coefficient, respectively. The thrust coefficient deviation and bias were dependent on the magnitude of the nozzle thrust being measured by the force balance and are plotted as such in Figure 17. The flow coefficient parameters are shown as a function of the flowmeter total pressure over the range for which STA data were taken. The upper limit to the STA model airflow and force balance loading was the maximum supply pressure at the venturies, approximately 276-290 N/cm<sup>2</sup> (400-420 psia). Based on these results, the data accuracy and repeatability were felt to be generally better than  $\pm 0.5\%$ .

## 6.2 MODEL THRUST COEFFICIENTS

The eight model configurations were run at tunnel Mach numbers of 0, 0.36, and 0.45. The outer nozzle pressure ratio was varied from 1.5 to 3.5. Two separate regimes of inner nozzle flow conditions were investigated - a "low" or bleed flow regime where the inner flow was varied from zero-flow up to 6% of the flow in the outer nozzle, and a "high" flow region in which the inner stream pressure ratio was varied from 1.1 to 3.5.

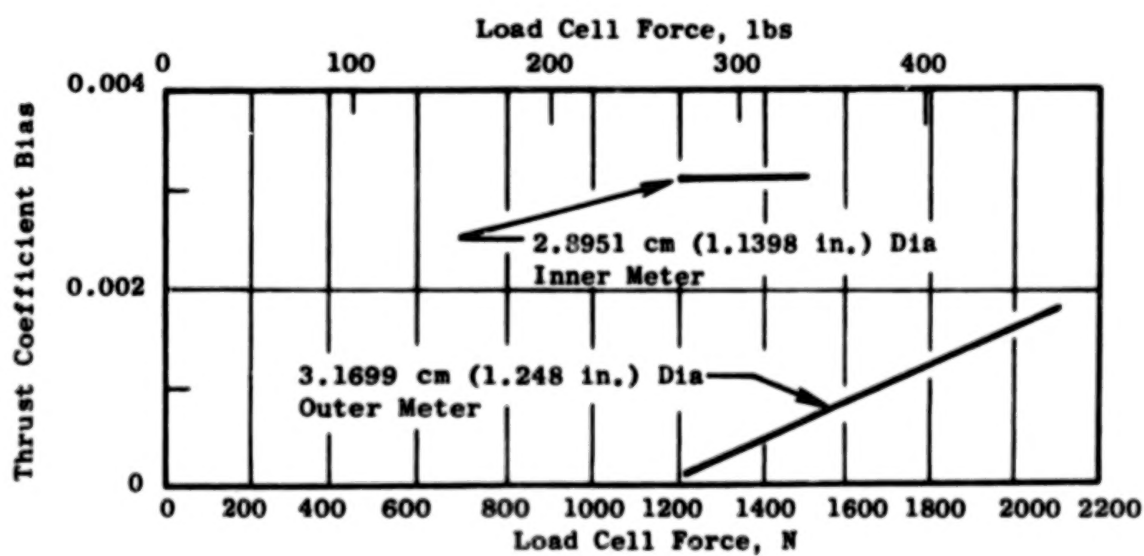
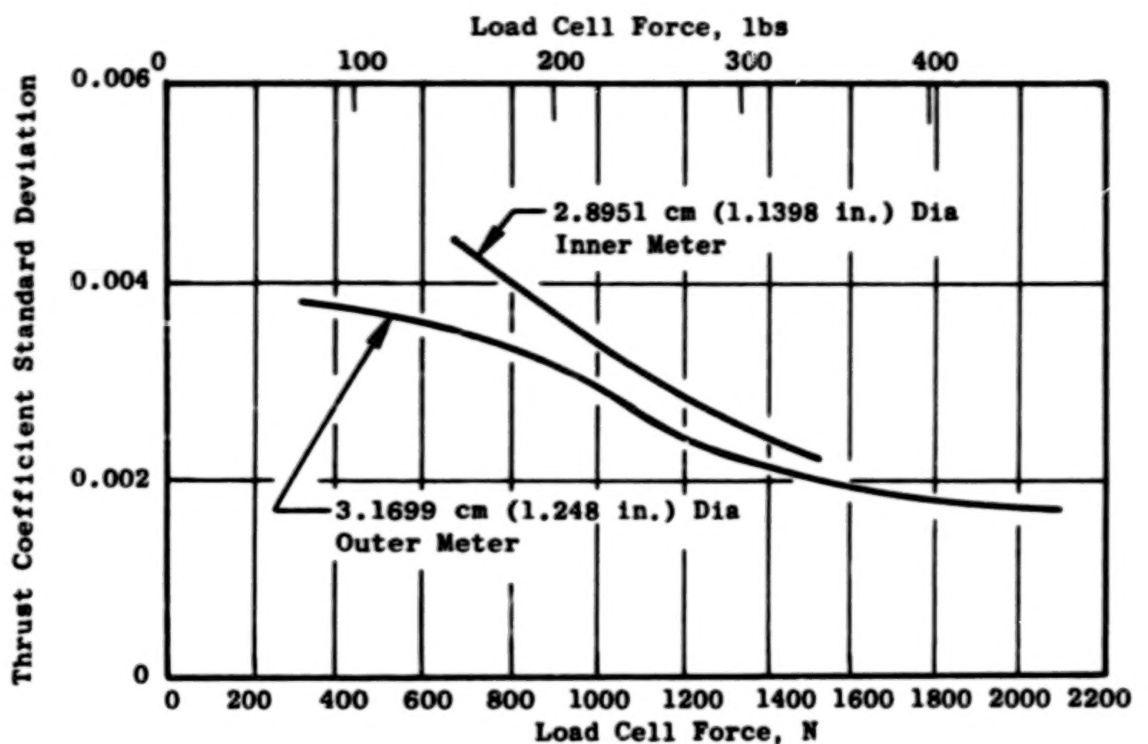


Figure 17. STA Nozzle Bias and Standard Deviation on Static Thrust Coefficient.

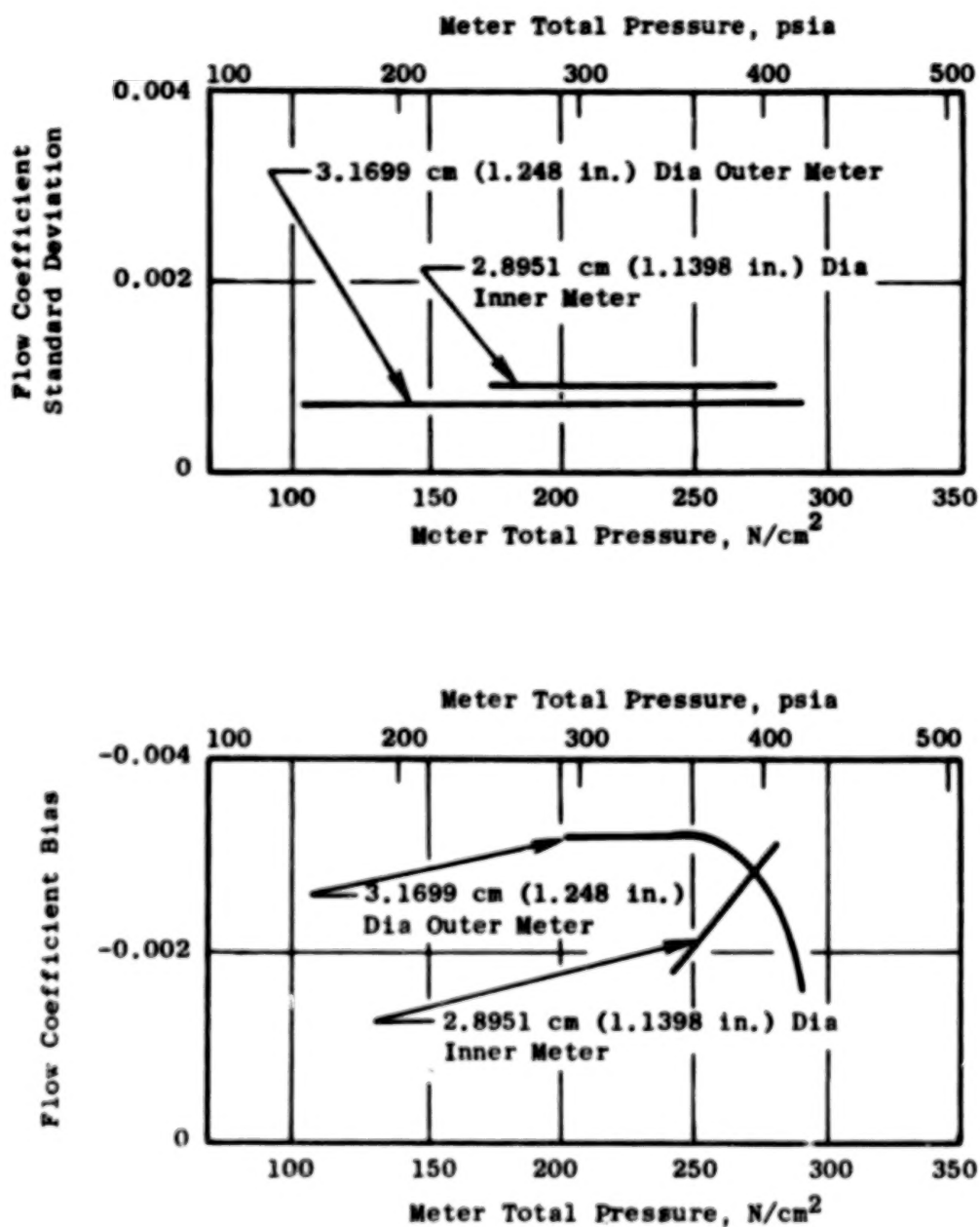


Figure 18. STA Nozzle Bias and Standard Deviation on Flow Coefficient.



The coefficients are plotted as functions of outer nozzle pressure ratio for lines of constant inner nozzle flow ratio for the low inner flow conditions and lines of inner nozzle pressure ratio for high flow rates. Typically, several repeat points were taken for each model: these are shown on the plots and depicted by flagged symbols. The repeatability was generally very good and was representative of the scatter experienced with the STA model as described in Section 6.1. At low balance loads (outer nozzle pressure ratios of 1.5 with low inner flow) during static testing, the differences between repeat points occasionally were greater than 1%. For the large majority of the test matrix, the spread between repeat points was consistently better than 0.5%.

Thrust coefficients for Configuration 1 [ $(R_r)_0 = 0.902$ ,  $(R_r)_1 = 0.673$ , bent inner plug] are shown in Figure 19 for high inner flow rates and Figure 20 for low inner flow rates. High inner flow thrust coefficients range between 0.95 and 0.972, with the peak performance occurring at an outer nozzle pressure ratio of 3.0 and an inner nozzle pressure ratio of 1.3. The low inner flow performance of Configuration 1 is quite low between 0.86 and 0.95 at a tunnel Mach number of 0.36. This performance increases rapidly both with increasing outer nozzle pressure ratio and inner nozzle flow rate.

Configuration 1 was a smaller scale version of a model which had previously been tested statically in another facility (see Reference 6): these same static points were repeated on Configuration 1 in the NASA Lewis tunnel. The results of the two tests are compared in Figure 21, which shows excellent agreement between the two facilities.

Configuration 2 [ $(R_r)_0 = 0.902$ ,  $(R_r)_1 = 0.8$ , conical inner plug] performance is shown in Figure 22 for high inner flow and in Figure 23 for low inner flow rates. This configuration exhibits high static performance from 0.97 to 0.986 with high inner flow rates. However, wind-on performance is lowered to 0.94 to 0.96. Low inner flow rate performance is again low, between 0.84 and 0.943 at Mach 0.36, and, like Configuration 1, is highly dependent on the inner flow rate and the outer nozzle pressure ratio.

High inner flow rate thrust coefficients for Configuration 3 [ $(R_r)_0 = 0.902$ ,  $(R_r)_1 = 0.902$ , conical inner plug] are presented in Figure 24. The

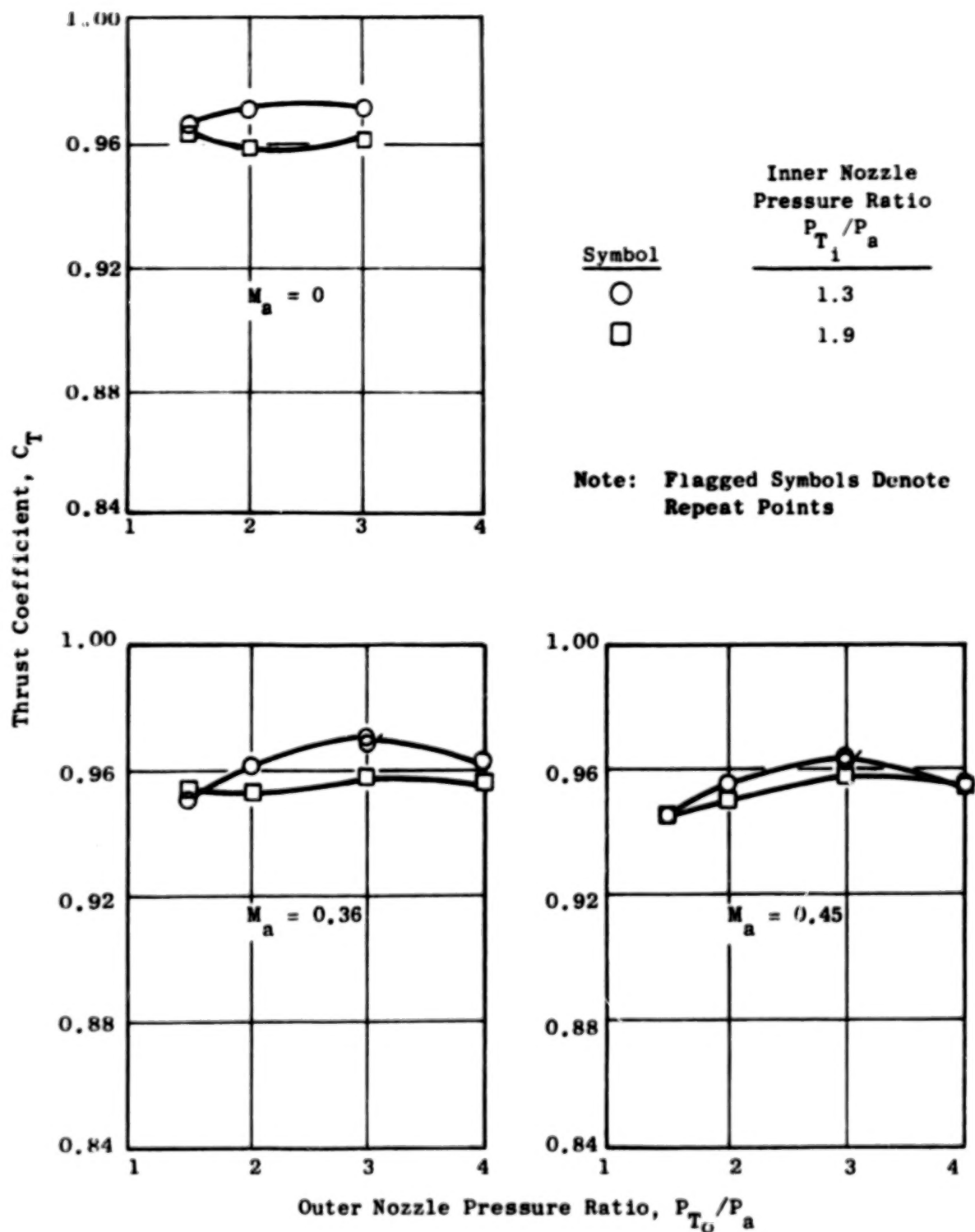


Figure 19. Thrust Coefficients for Configuration 1  $[(R_r)_0 = 0.902, (R_r)_1 = 0.673, \text{ Bent Inner Plug}]$  with High Inner Flow Rates.

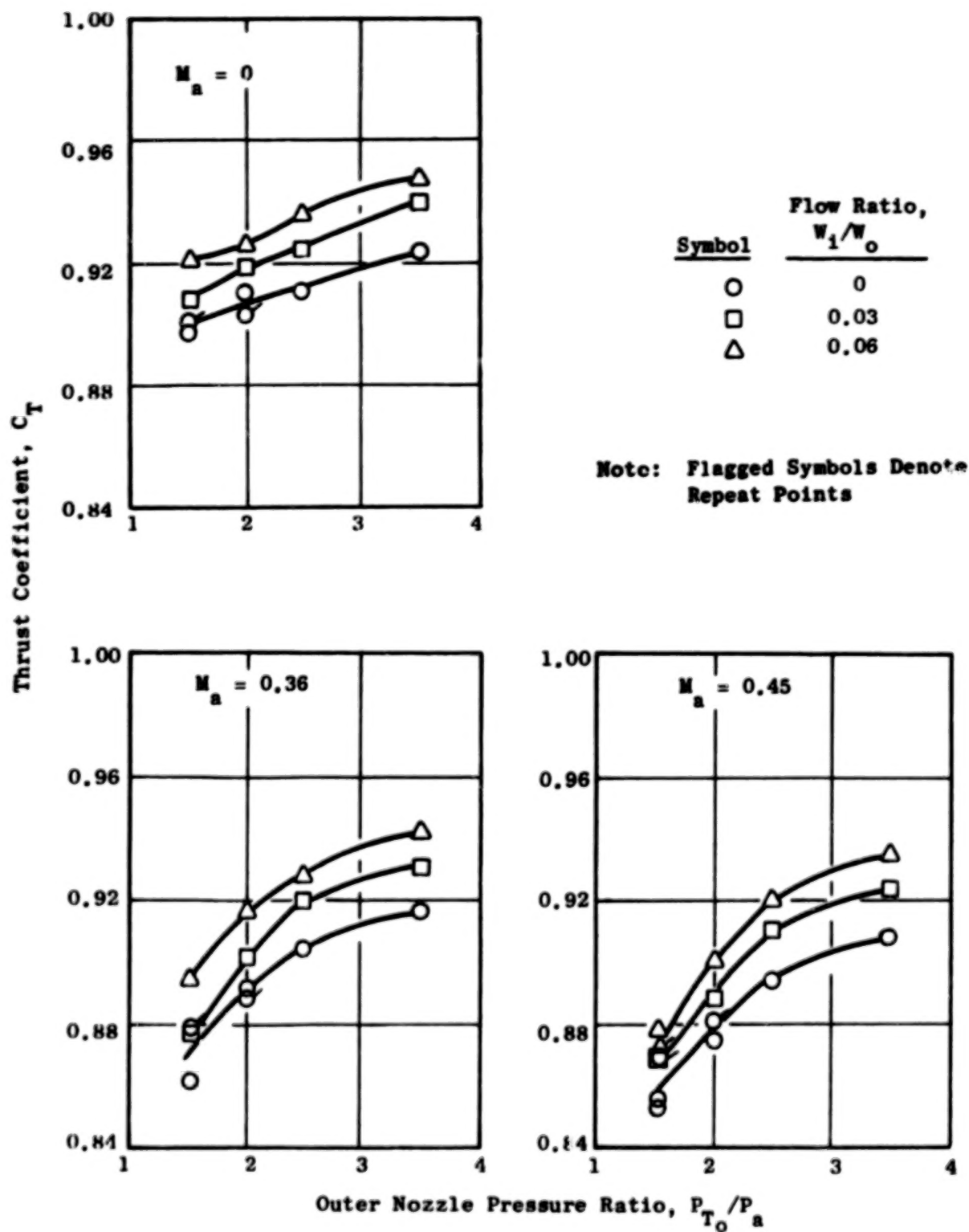


Figure 20. Thrust Coefficients for Configuration 1 [ $(R_r)_0 = 0.902$ ,  $(R_r)_1 = 0.673$ , Bent Inner Plug] with Low Inner Flow Rates.

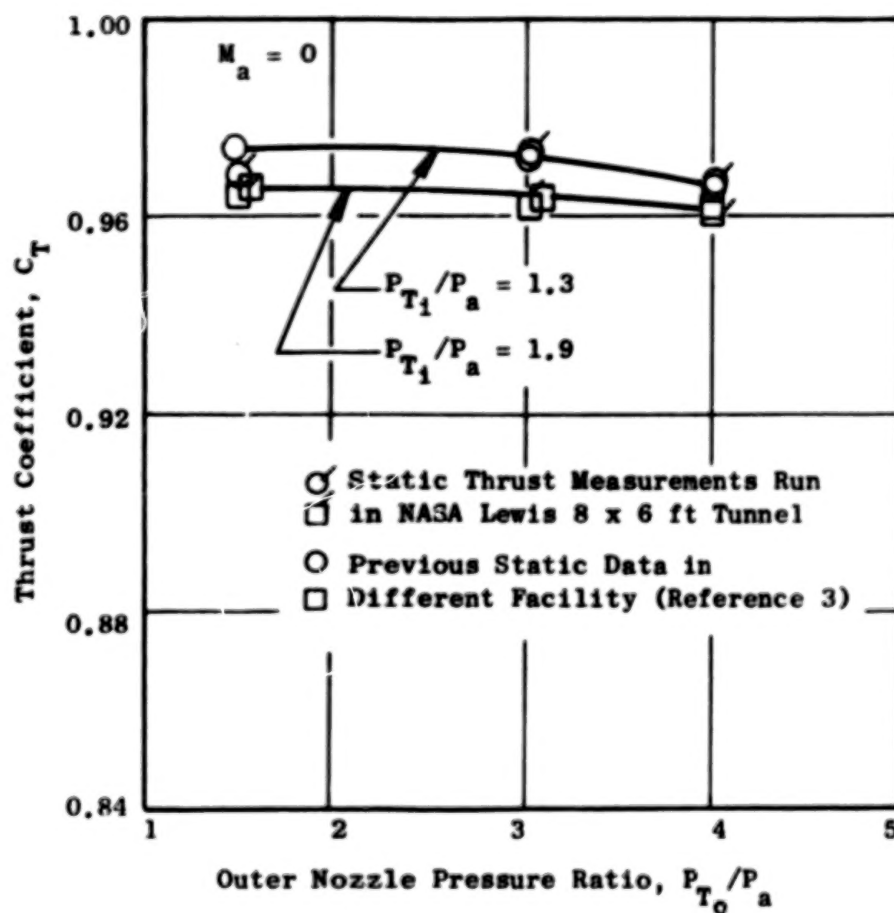


Figure 21. Configuration 1 Thrust Coefficients Compared to Previous Results.

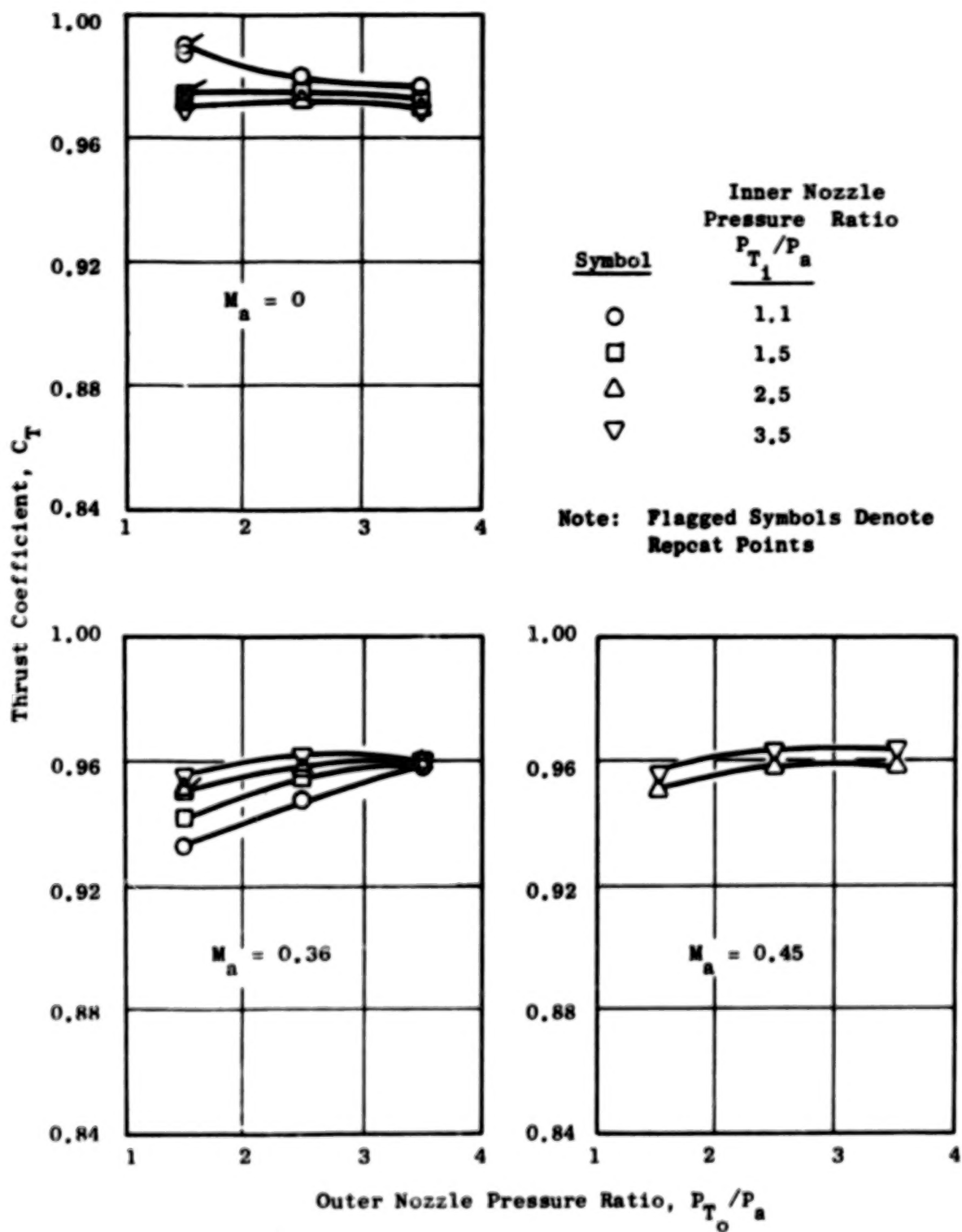
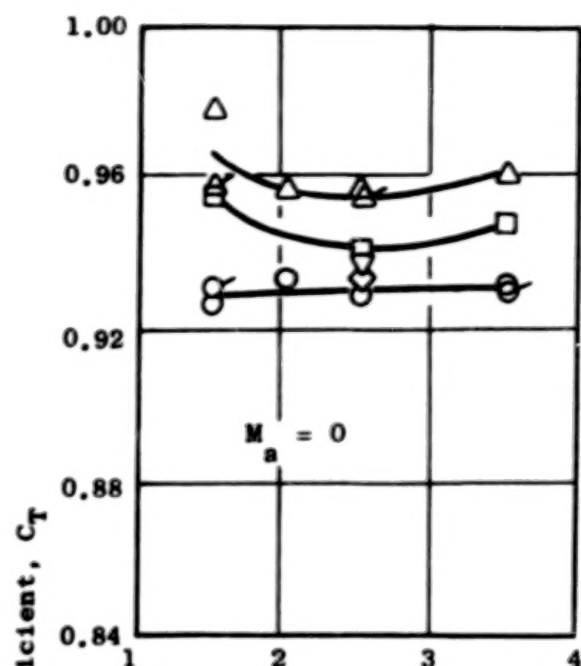
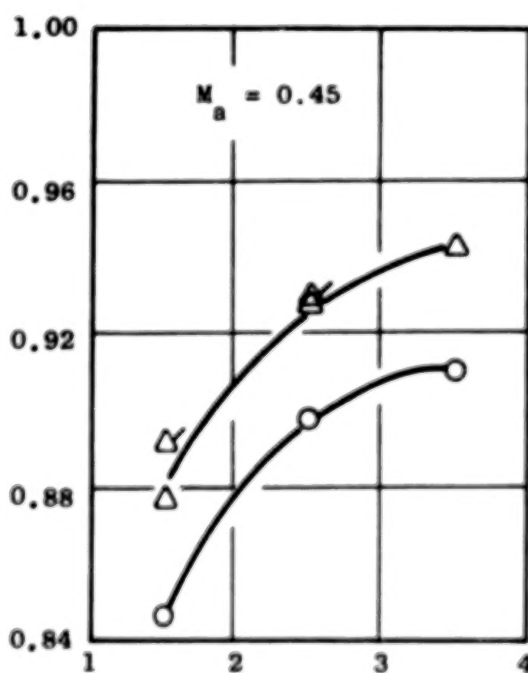
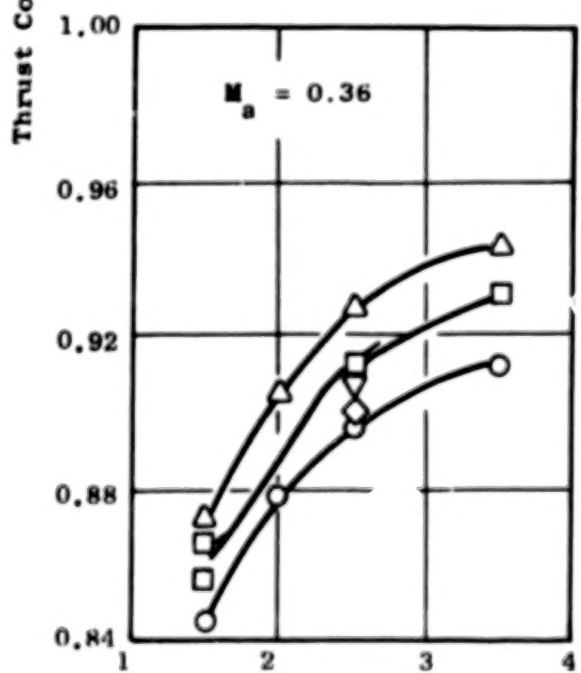


Figure 22. Thrust Coefficients for Configuration 2 [ $(R_r)_0 = 0.902$ ,  $(R_r)_1 = 0.8$ , Conical Inner Plug] with High Inner Flow Rates.



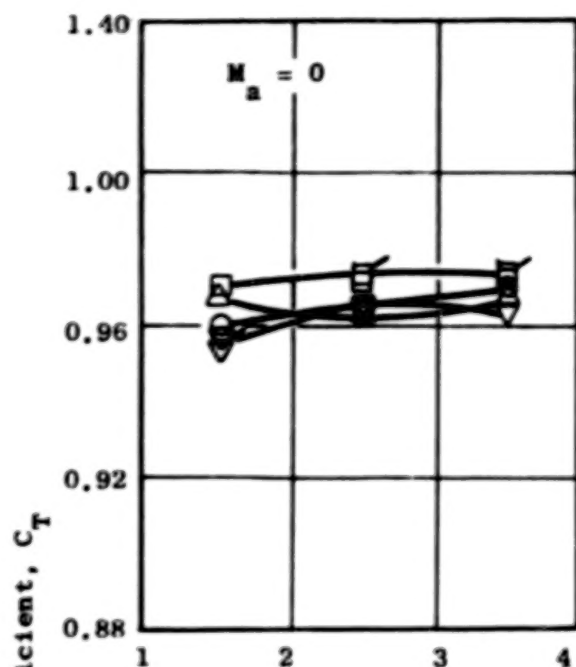
Symbol	Flow Ratio $W_1/W_0$
○	0
□	0.03
△	0.06
◇	0.01
▽	0.02

Note: Flagged Symbols Denote Repeat Points



Outer Nozzle Pressure Ratio,  $P_{T_c}/P_a$

Figure 23. Thrust Coefficients for Configuration 2  $[(R_r)_o = 0.902, (R_r)_i = 0.80, \text{Conical Inner Plug}]$  with Low Inner Flow Rates.



Symbol	Inner Nozzle Pressure Ratio $P_{T1}/P_a$
□	1.1
△	1.5
○	2.5
▽	3.5

Note: Flagged Symbols Denote Repeat Points

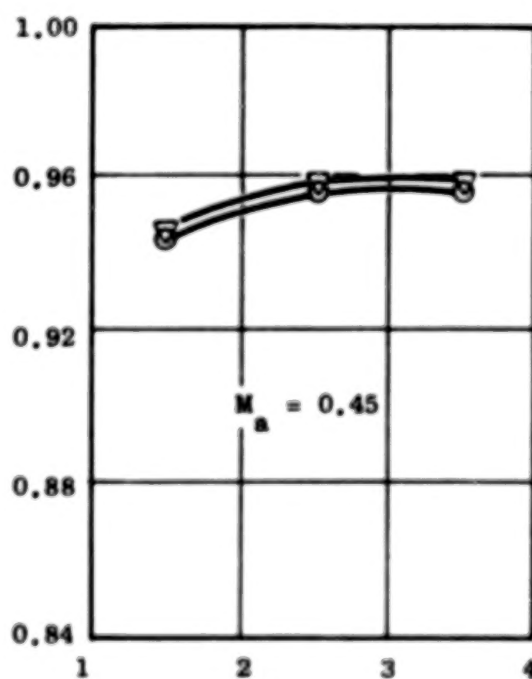
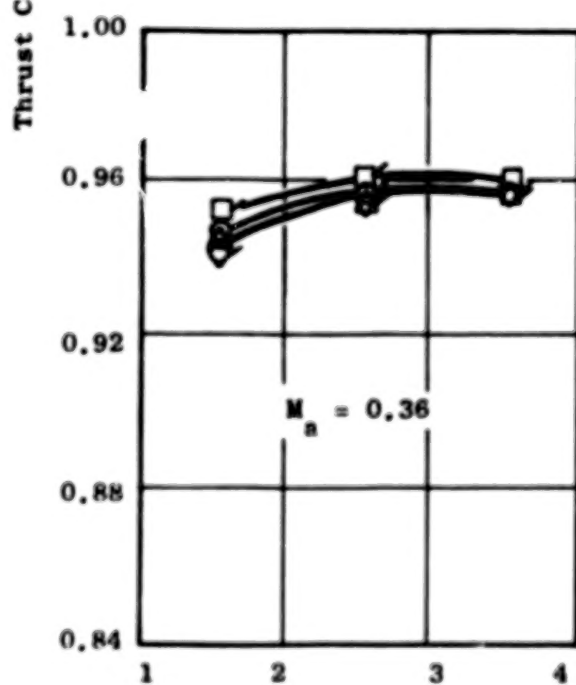


Figure 24. Thrust Coefficients for Configuration 3 [ $(R_r)_0 = 0.902$ ,  $(R_r)_1 = 0.902$ , Conical Inner Plug] with High Inner Flow Rates.

thrust coefficients peak at approximately 0.974 for static testing and 0.962 for an ambient Mach number of 0.36. The low inner flow rate performance for Configuration 3, shown in Figure 25, exhibits similar trends to Configurations 1 and 2 but attains better peak thrust. The measured wind-on thrust coefficient is approximately 0.96 with 6% inner bleed flow at an outer nozzle pressure ratio of 3.5.

Configuration 4 [ $(R_r)_0 = 0.902$ ,  $(R_r)_1 = 0.8$ , bent inner plug] performance is shown in Figures 26 and 27. This configuration incurs a performance penalty at the higher inner flow rates, i.e., inner nozzle pressure ratios of 2.5 and 3.5. Thrust coefficients at these conditions with an outer nozzle pressure ratio of 2.5 range from 0.946 to 0.954. This performance is lower than the respective values for Configurations 2 and 3 which have conical inner plug geometries. The bent inner plug of Configuration 4 creates a rapid expansion of the supersonic inner flow in the region of the plug angular change downstream of the inner nozzle throat. This results in a low pressure region on the plug and an associated thrust loss from the pressure drag. At the lower inner nozzle pressure ratios of 1.1 and 1.5, the inner flow remains subsonic so that the expansion at the corner is not severe and performance remains high. This difference in expansion characteristics can be seen in Figure 28 which shows the inner plug static pressure distributions for Configuration 4 with inner nozzle pressure ratios of 1.1 and 3.5. This effect is discussed in detail in Section 6.2.3.

Configuration 5 [ $(R_r)_0 = 0.853$ ,  $(R_r)_1 = 0.8$ , conical inner plug] demonstrated very good high inner flow rate performance, as shown in Figure 29. The static performance ranges from 0.965 to 0.982 and there is little decrease with wind-on conditions. Mach 0.36 thrust coefficients are between 0.97 and 0.975 at an outer nozzle pressure ratio of 2.5 for all the inner pressure ratios tested. The low inner flow rate performance for this configuration, presented in Figure 30, is also high, reaching 0.965 statically and 0.963 at Mach 0.36 for an outer nozzle pressure ratio of 2.5 and a 6% inner flow rate.

The performance for Configuration 6 [ $(R_r)_0 = 0.926$ ,  $(R_r)_1 = 0.8$ , conical inner plug], shown in Figures 31 and 32, is generally the lowest of



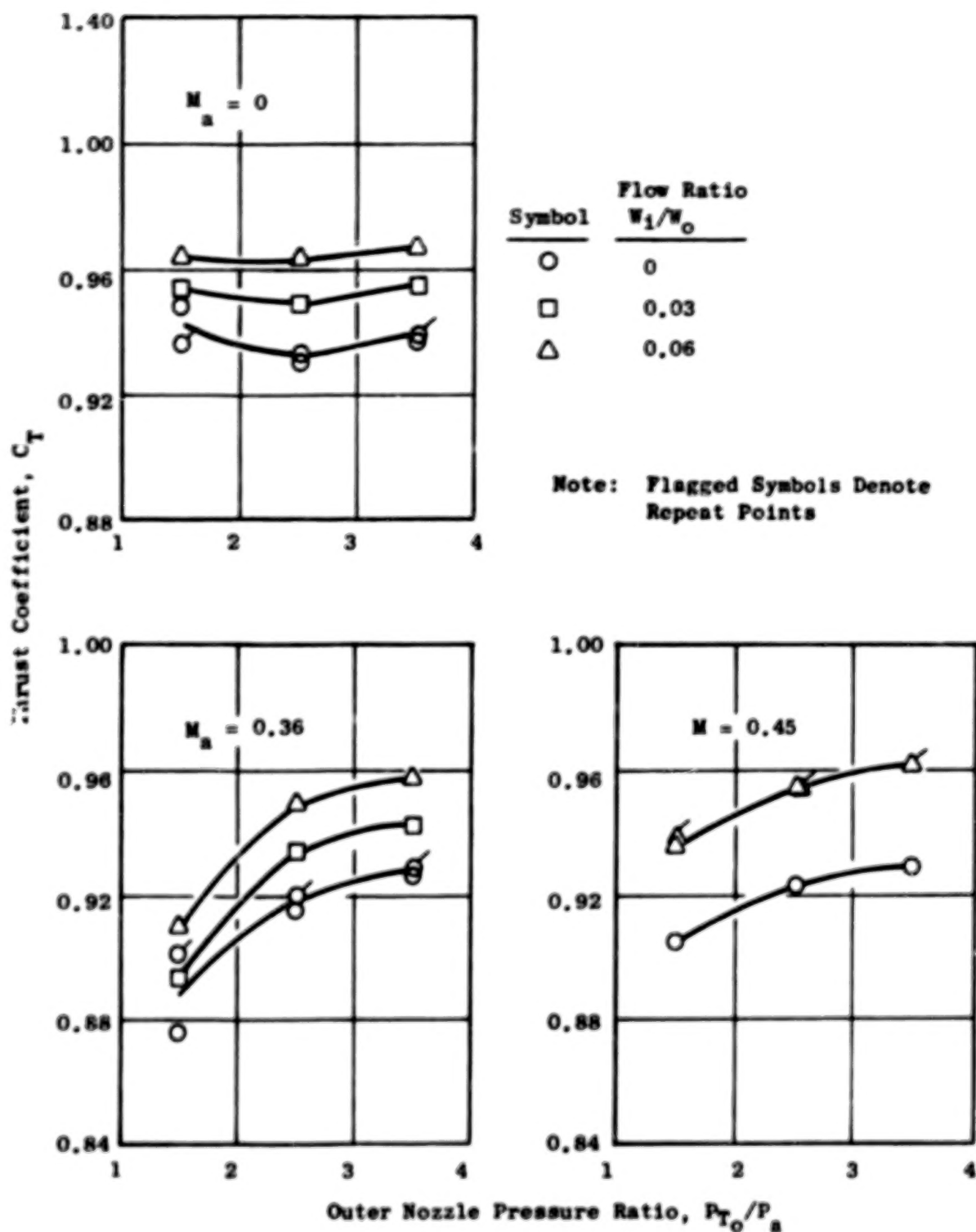


Figure 25. Thrust Coefficients for Configuration 3 [ $(R_r)_0 = 0.902$ ,  $(R_r)_i = 0.902$ , Conical Inner Plug] with Low Inner Flow Rates.

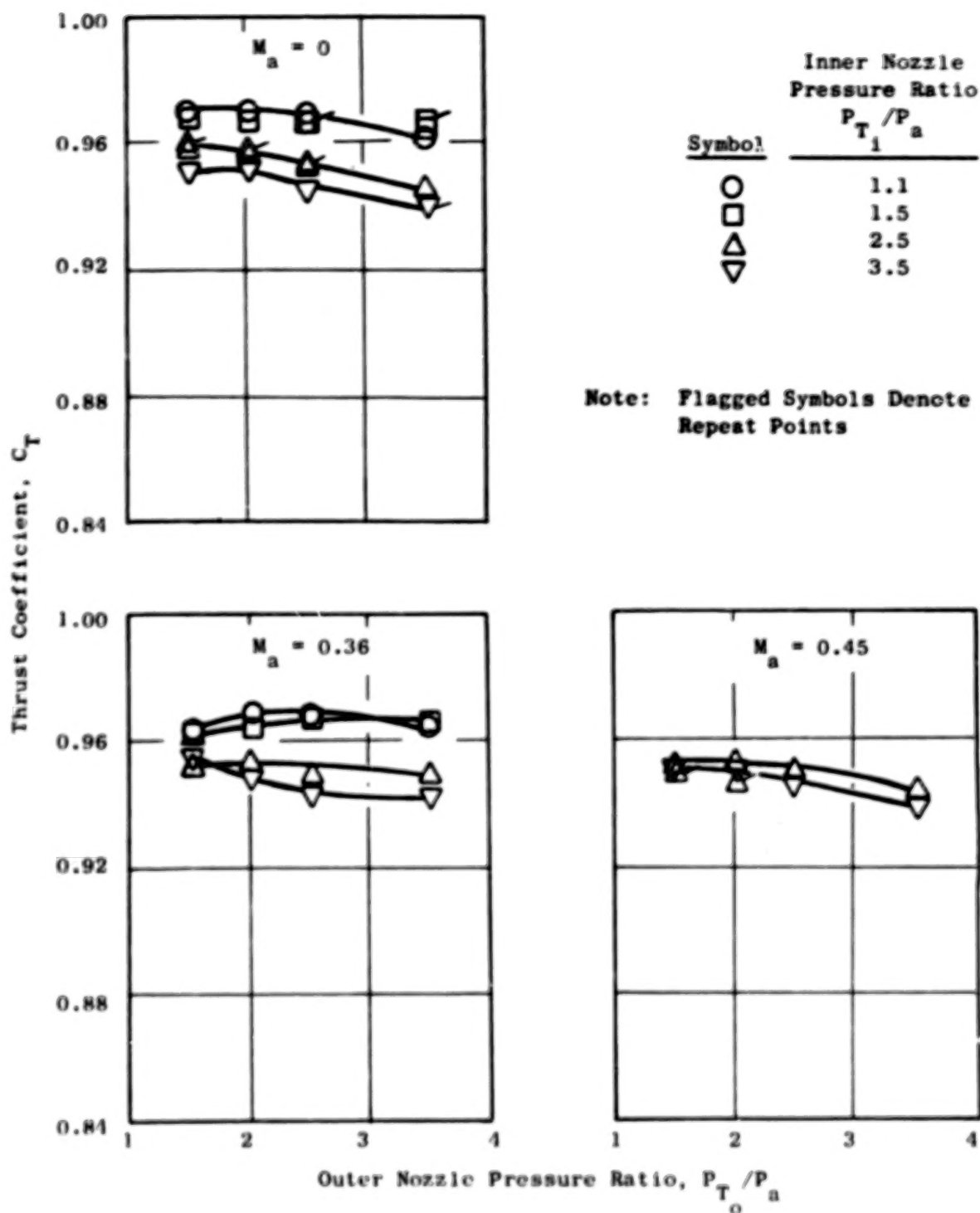


Figure 26. Thrust Coefficients for Configuration 4  $[(R_R)_0 = 0.902, (R_R)_1 = 0.8, \text{ Bent Inner Plug}]$  with High Inner Flow Rates.

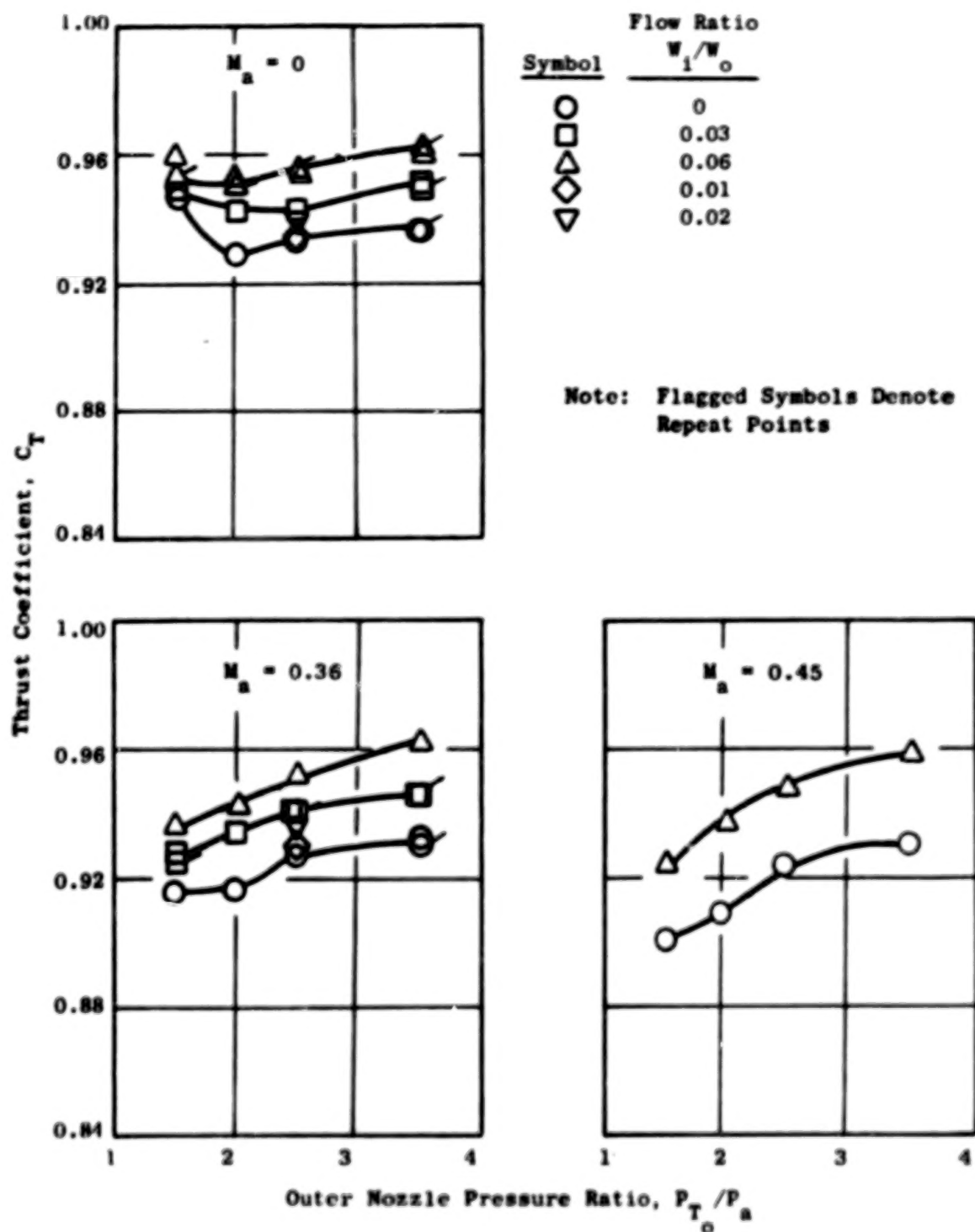


Figure 27. Thrust Coefficients for Configuration 4  $[(R_T)_o = 0.902, (R_T)_i = 0.8, \text{ Bent Inner Plug}]$  with Low Inner Flow Rates.

Note:  $X/DM = 0$  at Outer Nozzle Throat Axial Location  
 $DM = 0.203 \text{ m (8.0 in.)}$

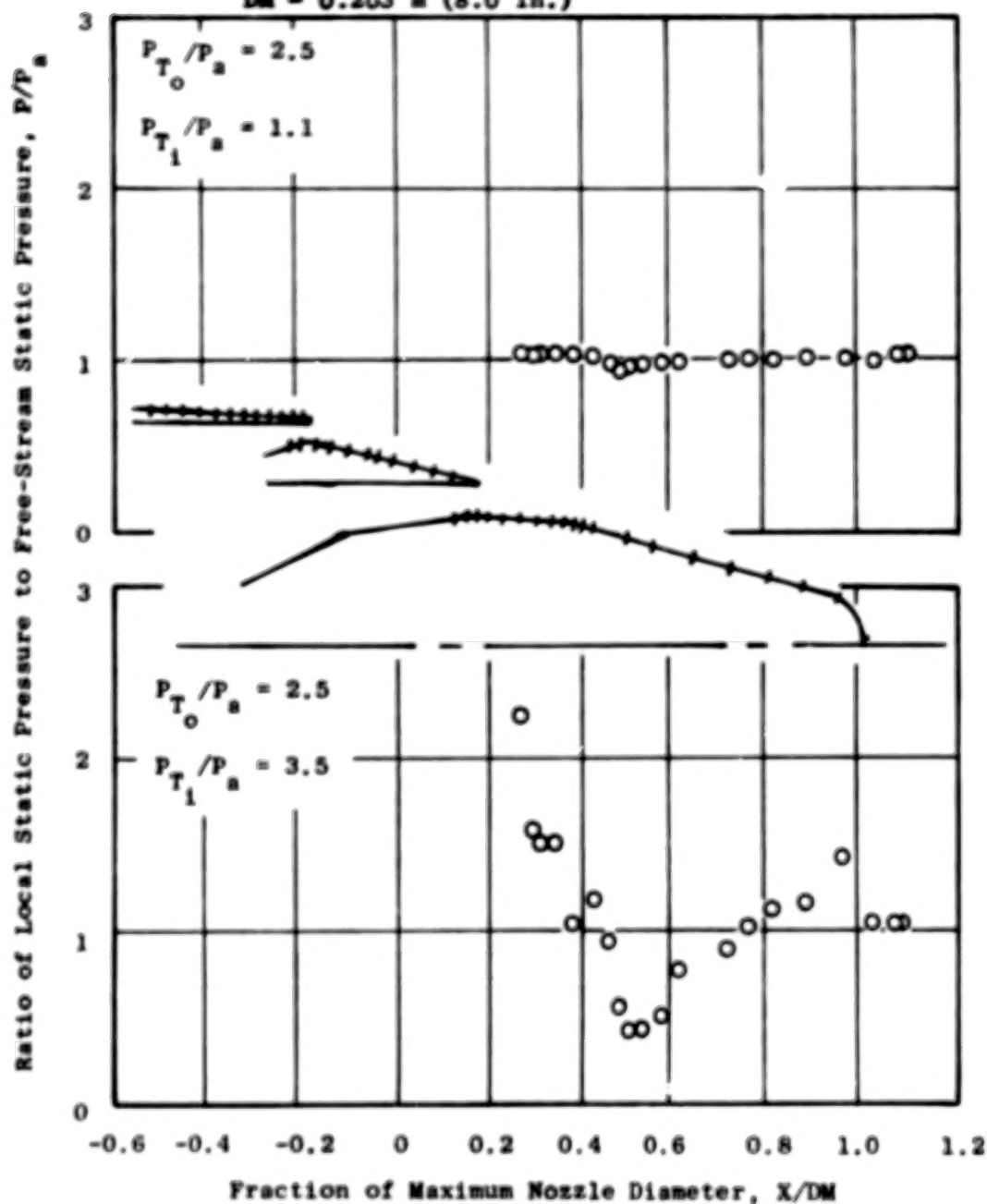


Figure 28. Inner Plug Pressure Distributions, Configuration 4  
 $[(R_r)_0 = 0.902, (R_r)_1 = 0.8, \text{ Bent Inner Plug}]$ .

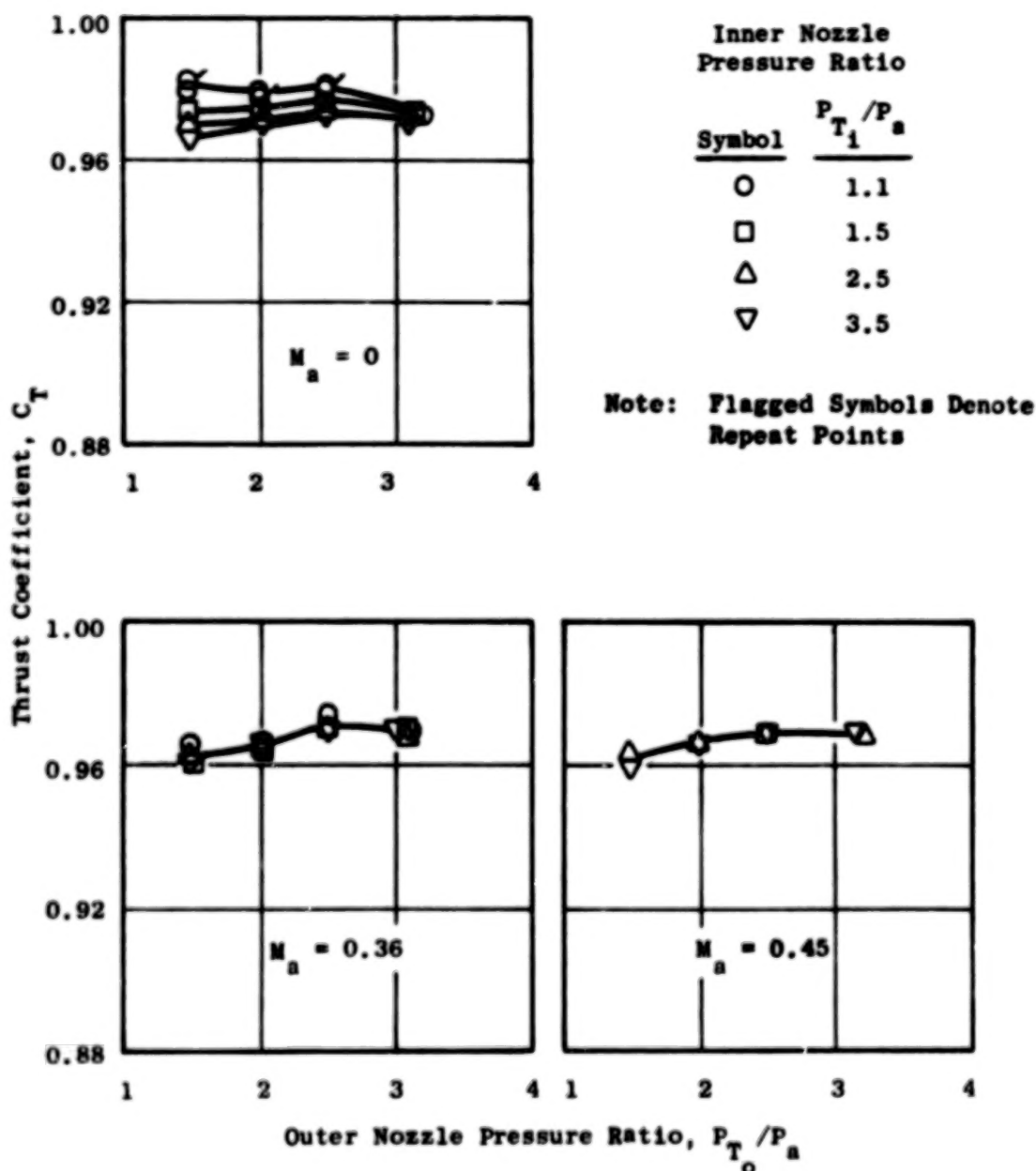


Figure 29. Thrust Coefficients for Configuration 5 [ $(R_r)_0 = 0.853$ ,  $(R_r)_1 = 0.8$ , Conical Inner Plug] with High Inner Flow Rates.

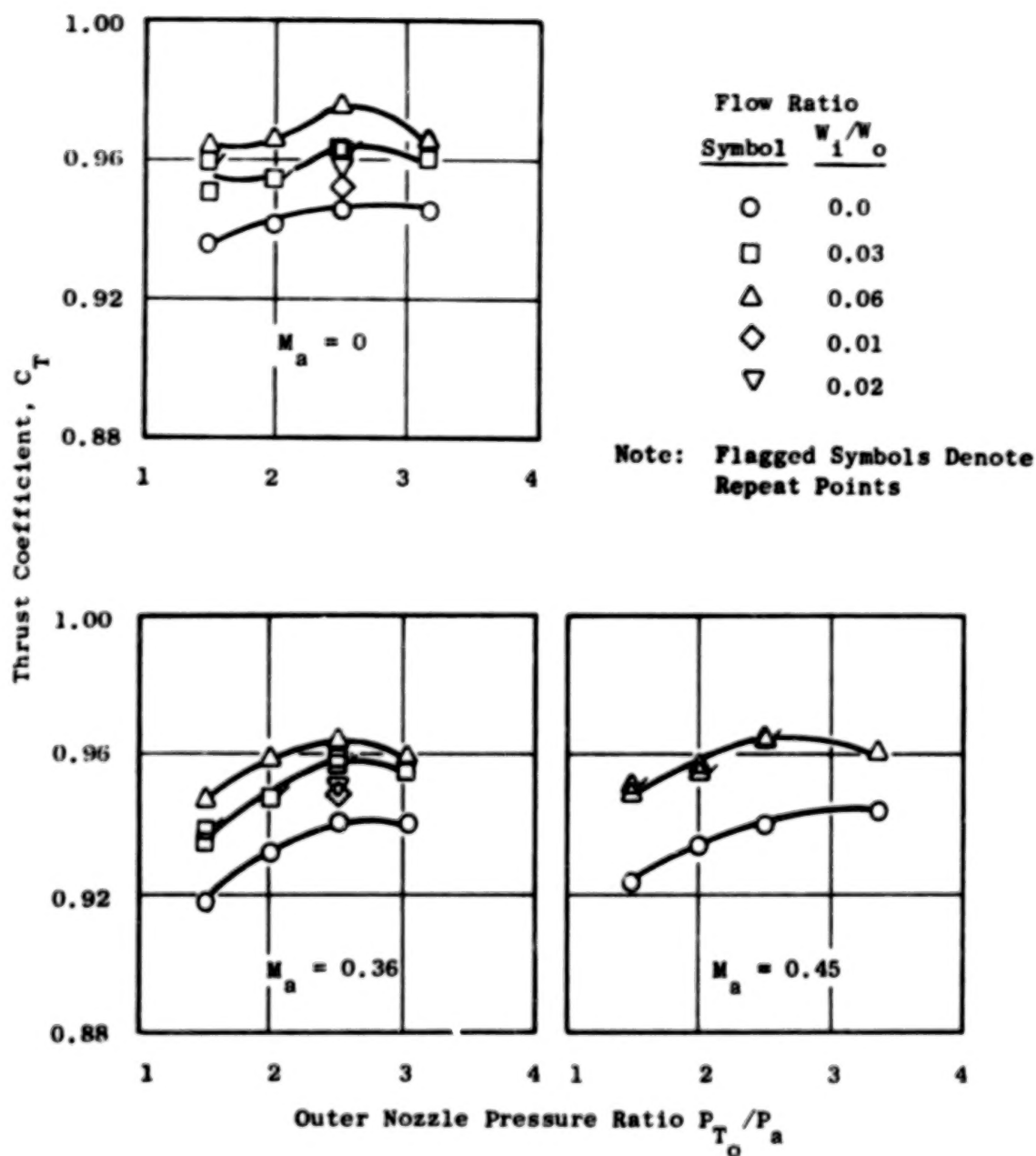


Figure 30. Thrust Coefficients for Configuration 5  $[(R_r)_0 = 0.853, (R_r)_1 = 0.8, \text{Conical Inner Plug}]$  with Low Inner Flow Rates.

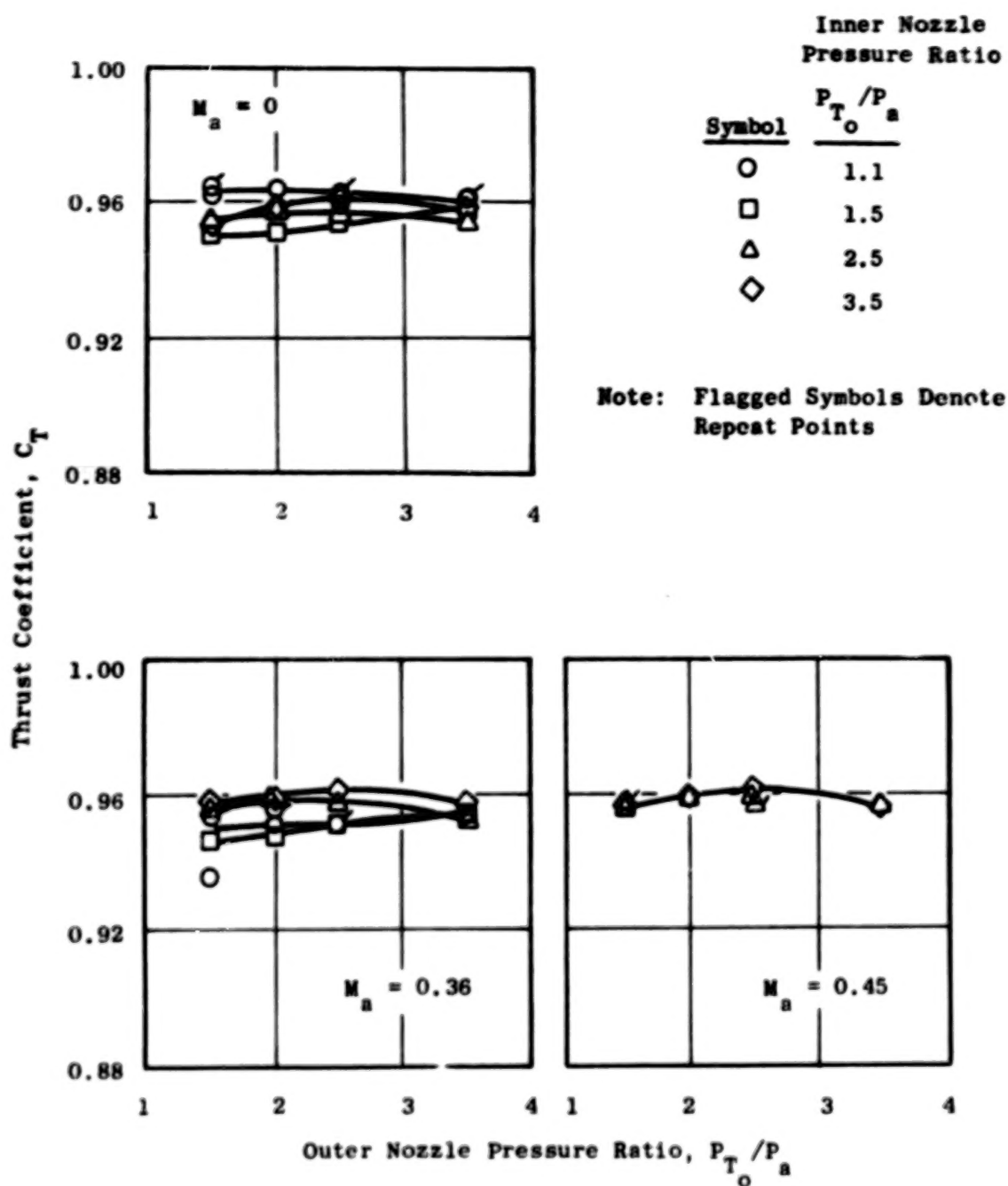


Figure 31. Thrust Coefficients for Configuration 6 [ $(R_r)_o = 0.926$ ,  $(R_r)_1 = 0.8$ , Conical Inner Plug] with High Inner Flow Rates.

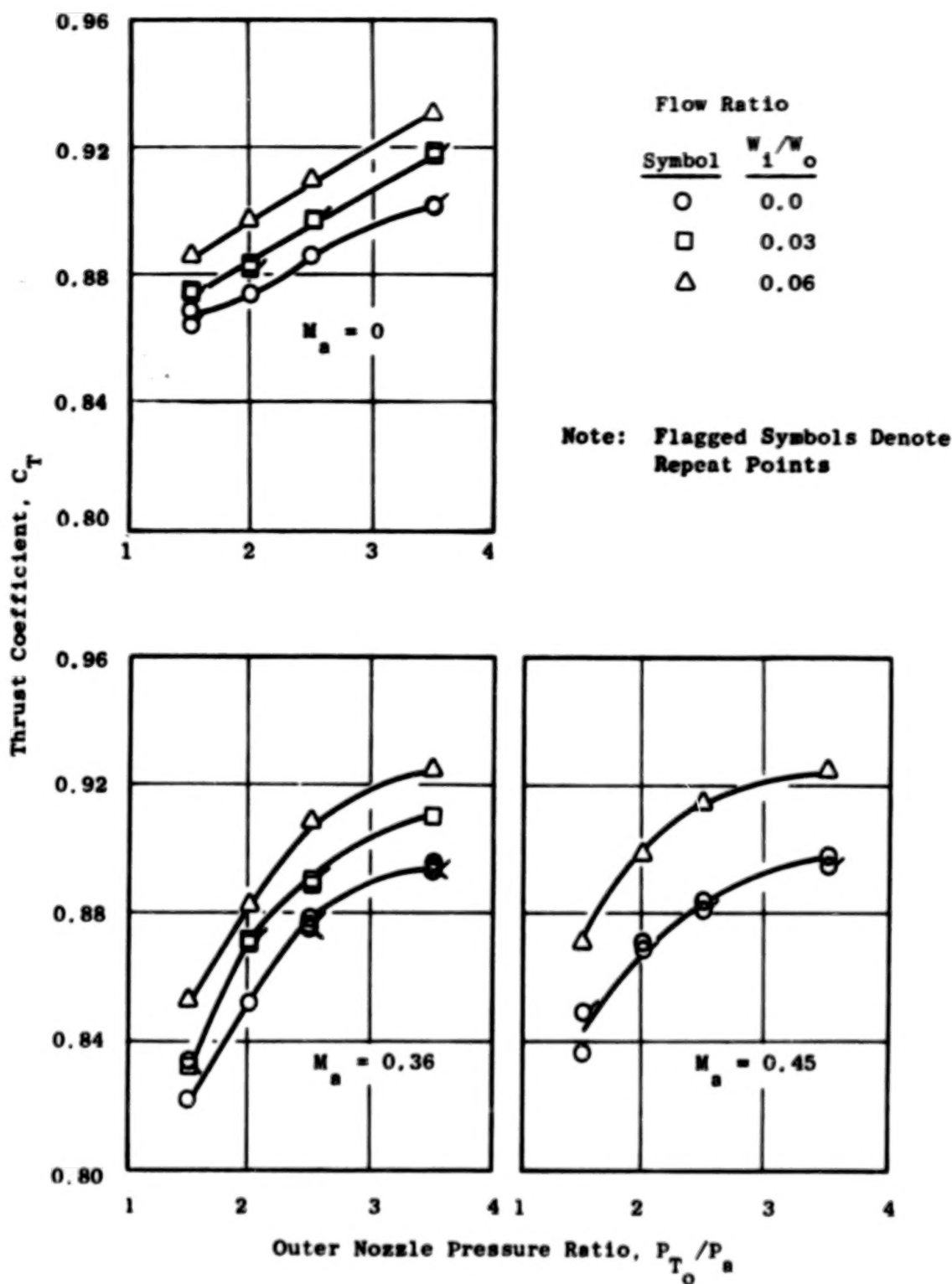


Figure 32. Thrust Coefficients for Configuration 6  $[(R_r)_0 = 0.926, (R_r)_1 = 0.8, \text{Conical Inner Plug}]$  with Low Inner Flow Rates.



all configurations tested. Peak high inner flow rate thrust coefficients are 0.965 statically and 0.961 with wind-on. Coefficients during low inner flow operation vary between 0.82 and 0.93.

Thrust coefficients are shown in Figures 33 and 34 for Configuration 7  $[(R_r)_o = 0.853, (R_r)_i = 0.902, \text{conical inner plug}]$ . This configuration exhibited the best performance of all configurations during low inner flow testing. The peak static thrust coefficient is 0.972 at an outer nozzle pressure ratio of 2.5 and a 6% inner flow rate: there is virtually no loss in performance as the ambient velocity is increased, with the thrust coefficient measuring 0.971 at the same nozzle conditions and a Mach number of 0.36.

Configuration 8  $[(R_r)_o = 0.853, (R_r)_i = 0.8, \text{bent inner plug}]$  exhibits high performance, shown in Figures 35 and 36, similar to Configuration 7 with one exception: the bent inner plug of Configuration 8 results in a performance loss at high inner nozzle pressure ratios. This also occurs on the bent plug configuration of Configuration 4.

The performance levels and trends exhibited by these models, as well as the effect of the major model configurational and operational variables, are discussed in the following subsections.

#### 6.2.1 Effect of Outer Nozzle Radius Ratio

The effect of outer nozzle radius ratio on nozzle performance can be seen by comparing Configurations 5, 2, and 6, which have an inner radius ratio of 0.8 conical plug and outer radius ratios of 0.853, 0.902, and 0.926, respectively. Also, Configurations 4 and 8 give comparisons of outer radius ratios 0.902 and 0.853 for the bent inner plug with a radius ratio of 0.8. Figure 37 shows thrust coefficient plotted as a function of outer radius ratio, using Configurations 5, 2, and 6, for low inner flow rates at an outer nozzle pressure ratio of 2.5. Both statically and at Mach 0.36, the thrust coefficient decreases rapidly as the radius ratio is increased above 0.853. Figure 38 shows a similar trend for these models with high inner flow rates, although the severity of the trend is reduced: 1-2% decrease in thrust coefficient in going from 0.853 to 0.926 radius ratio with high inner

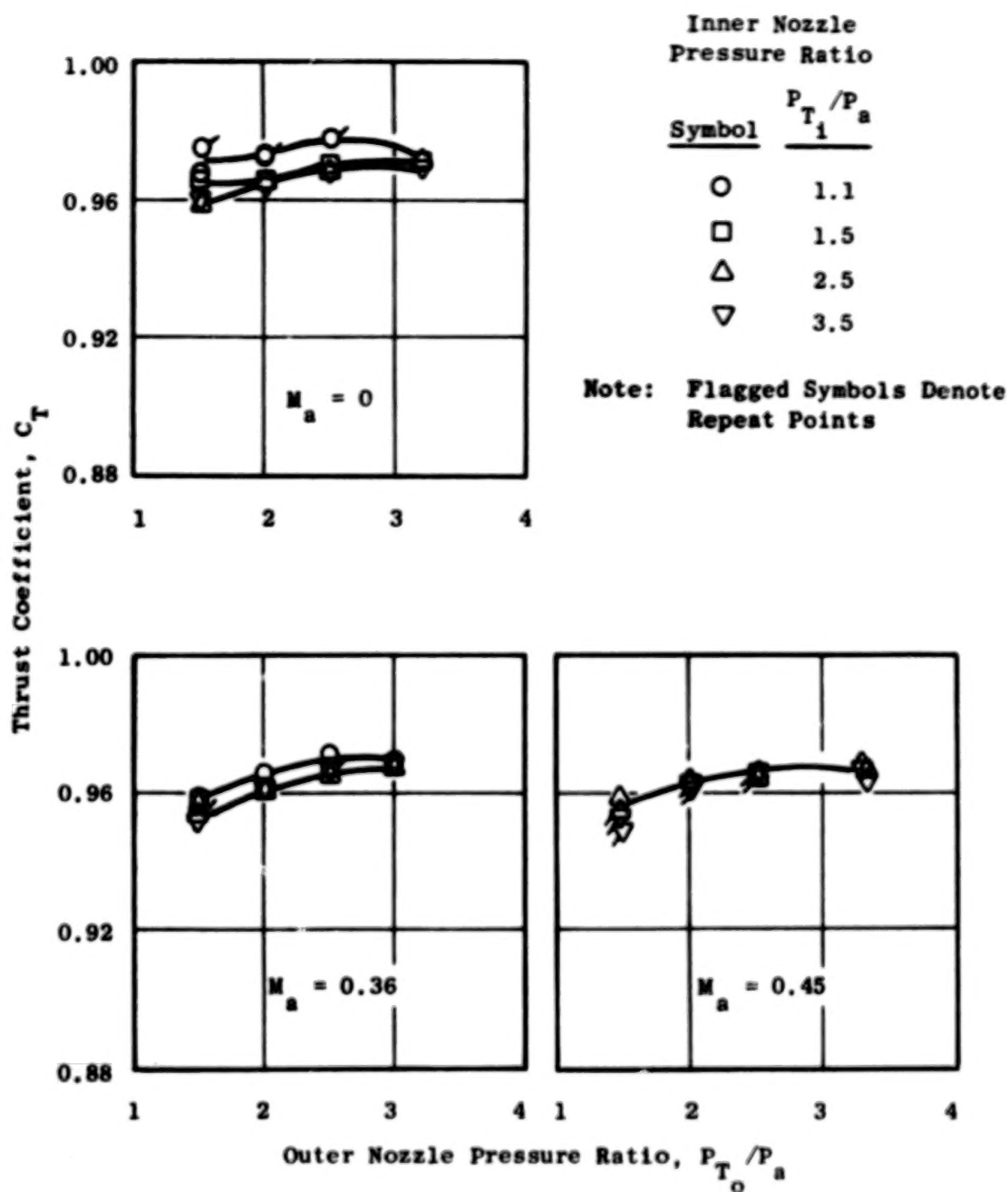


Figure 33. Thrust Coefficients for Configuration 7 [ $(R_r)_0 = 0.853$ ,  $(R_r)_1 = 0.902$ , Conical Inner Plug] with High Inner Flow Rates.

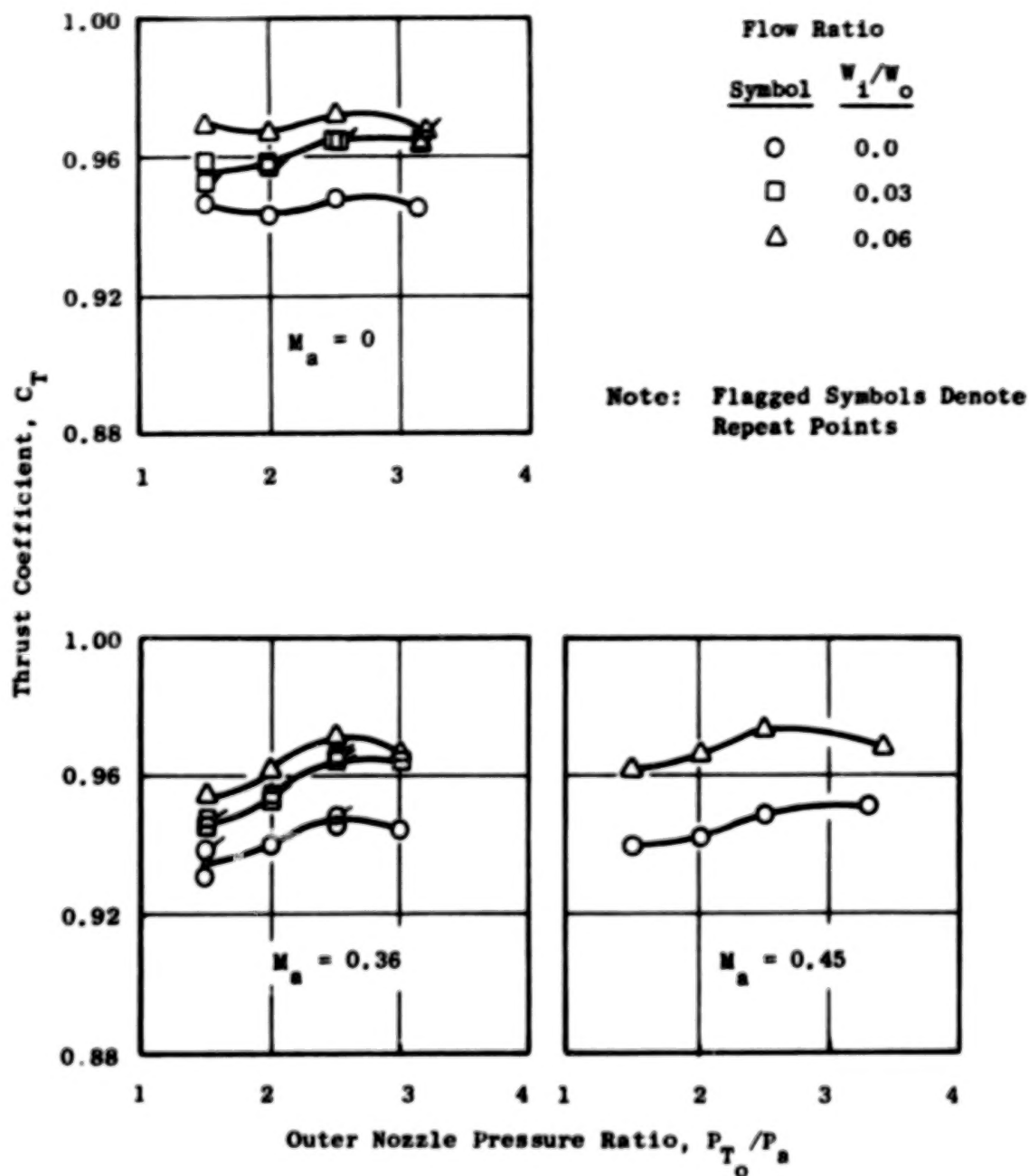


Figure 34. Thrust Coefficients for Configuration 7 [ $(R_T)_0 = 0.853$ ,  $(R_T)_1 = 0.902$ , Conical Inner Plug] with Low Inner Flow Rates.

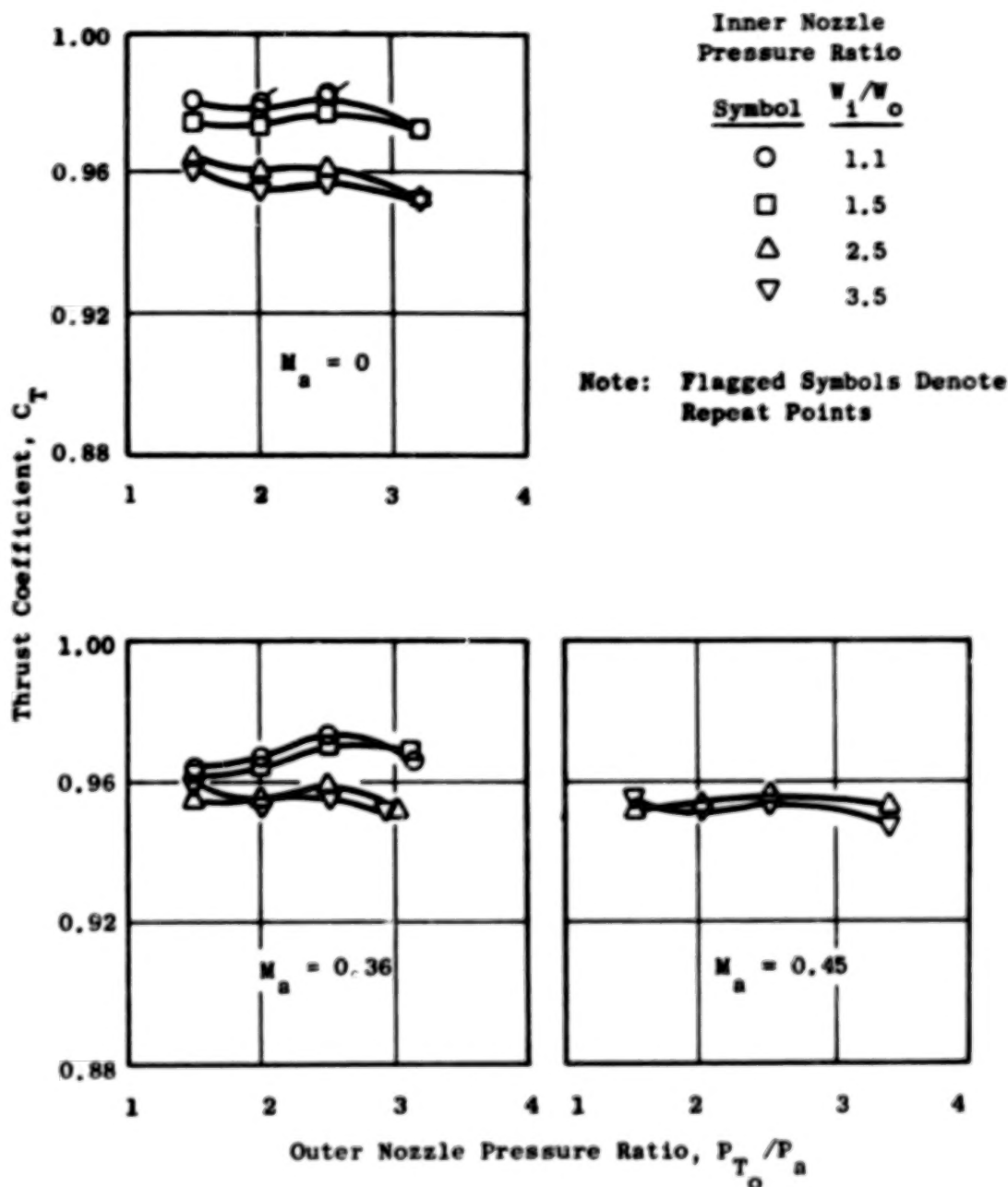


Figure 35. Thrust Coefficients for Configuration 8  $[(R_r)_0 = 0.853, (R_r)_1 = 0.8, \text{ Bent Inner Plug}]$  with High Inner Flow Rates.

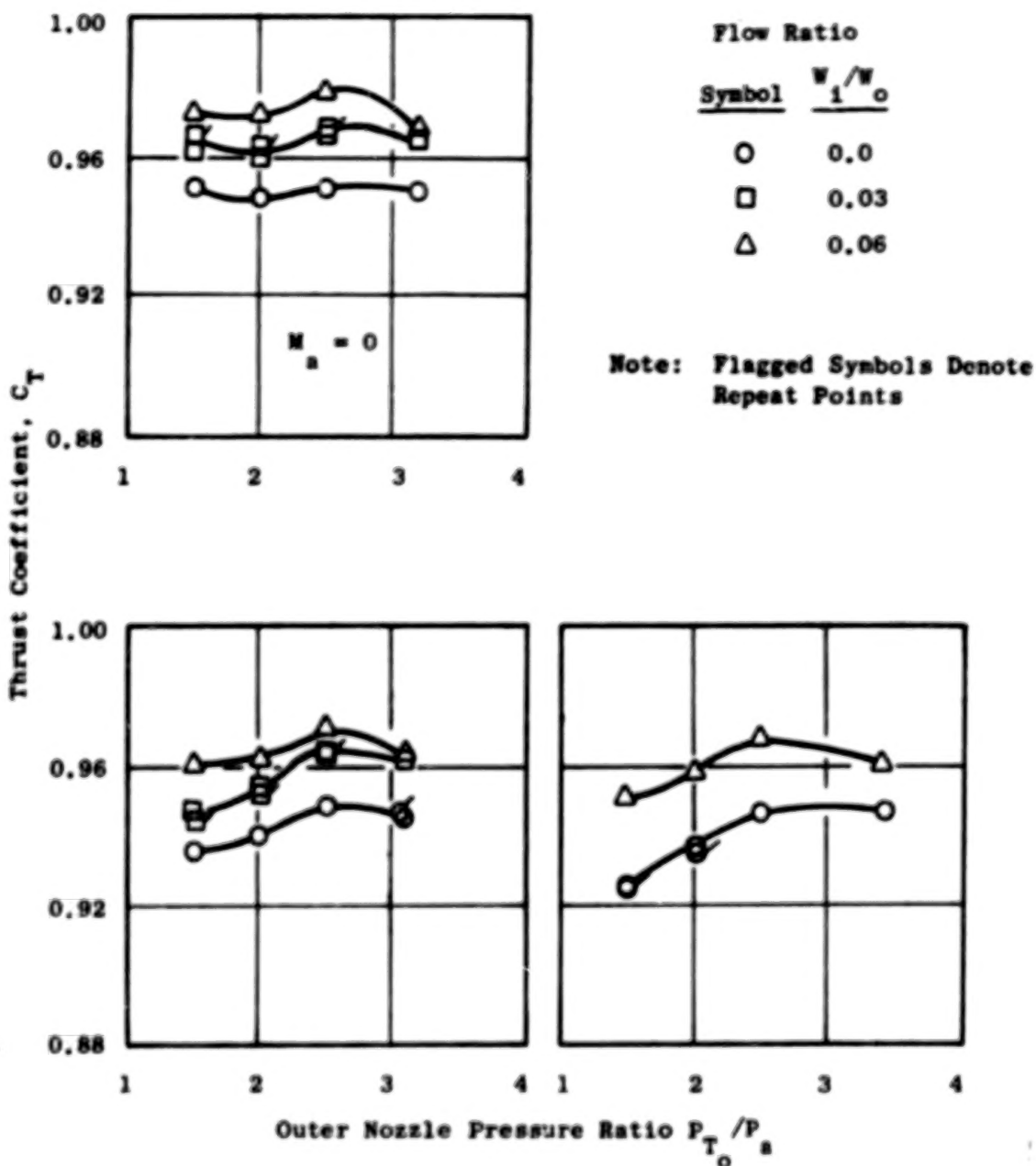


Figure 36. Thrust Coefficients for Configuration 8 [ $(R_F)_0 = 0.853$ ,  $(R_F)_1 = 0.8$ , Bent Inner Plug] with Low Inner Flow Rates.

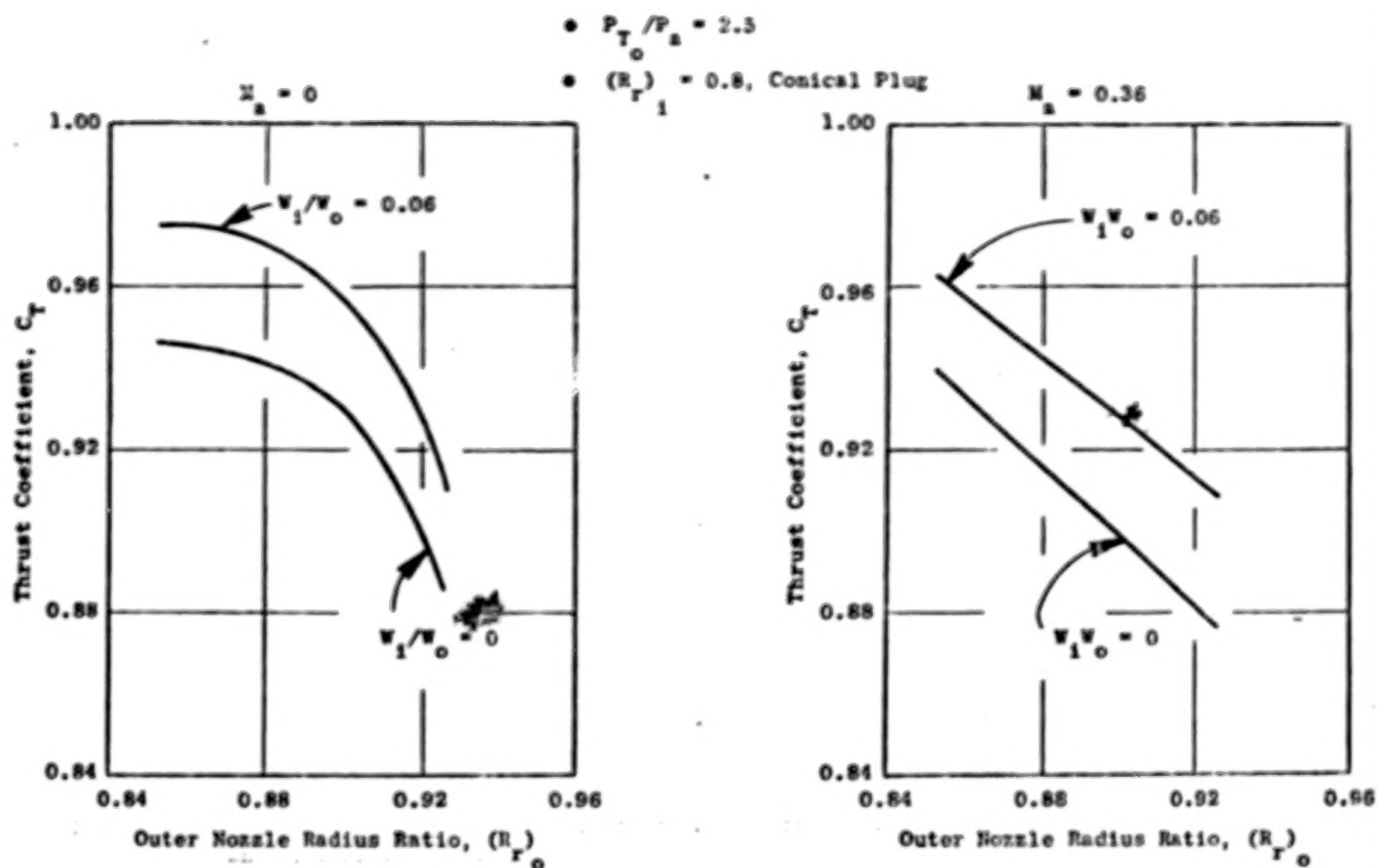


Figure 37. Thrust Coefficient as a Function of Outer Nozzle Radius Ratio for Low Inner Flow Rates and Conical Inner Plug.

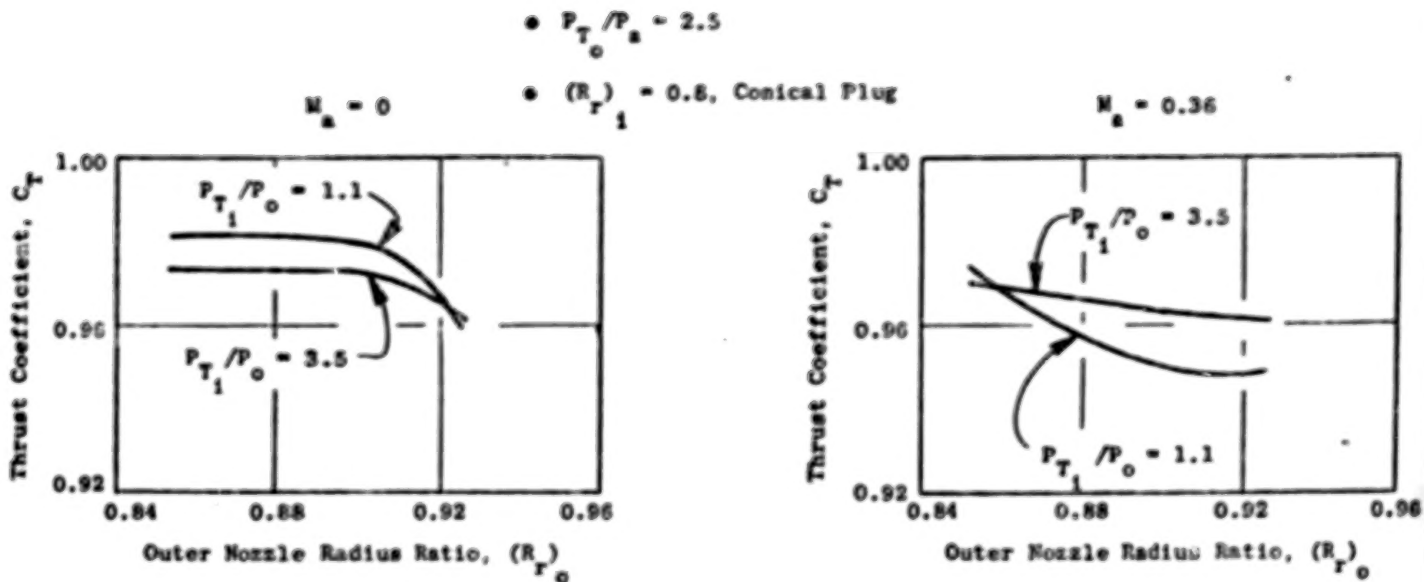


Figure 38. Thrust Coefficient as a Function of Outer Nozzle Radius Ratio for High Inner Flow Rates and Conical Inner Plug.

flow, compared to 5-6% decrease with low inner flow rates. Figures 39 and 40 show the same trend for the bent core plug geometry of Configurations 4 and 8. (The curves on Figures 39 and 40 are shown as a straight line connection between two points, radius ratio 0.853 and 0.902, merely as a way of illustrating the trend.)

The effect of increasing the outer nozzle radius ratio is to increase the plug size relative to the flow area, i.e., the ratio of plug expansion area and wetted surface area to the nozzle throat area increases. This results in an increased skin friction drag effect relative to ideal thrust, lowering the thrust coefficient. This effect is larger for the low inner flow tests due to the lower thrust levels of these models, i.e., the same amount of wetted areas for a model during both high and low-flow testing, but the skin friction is a greater percentage of the total nozzle thrust for the low-flow conditions. In addition, for low inner flow conditions, the inner duct creates a thrust loss, as will be discussed in Section 6.2.2. This loss becomes a larger percent of overall thrust as the outer radius ratio is decreased, causing the performance to drop.

As a consequence of the manner in which outer nozzle radius ratio was varied by changing the outer shroud, the higher radius ratio models had more projected boattail area. This contributes to the decreasing thrust coefficient at Mach 0.36 as shown in Figures 37 and 38, although this is obviously not a factor at the static conditions shown in the figures.

#### 6.2.2 Effect of Inner Nozzle Radius Ratio

The effect of inner nozzle radius ratio (or inner step height) can be illustrated by comparing Configurations 2 versus 3, for an outer radius ratio of 0.902 and conical inner plug geometry; Configurations 1 versus 4 for bent inner plug geometry; and Configurations 5 versus 7 for conical inner plugs at an outer radius ratio of 0.853. Figures 41 and 42 show the variation of thrust coefficient with inner radius ratio for these configurations with low inner flow rates. Since only two configurations are used to generate each line in these figures, the plot is shown as a straight line between the two points merely to indicate the direction of the trend.



- $P_{T_o}/P_a = 2.5$

- $(R_r)_1 = 0.8$ , Bent Plug

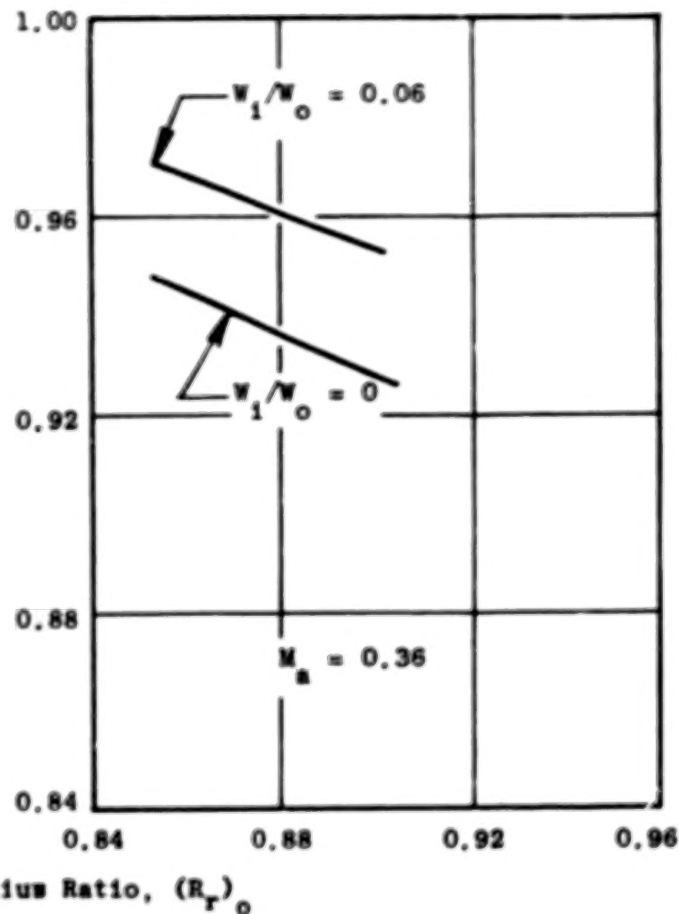
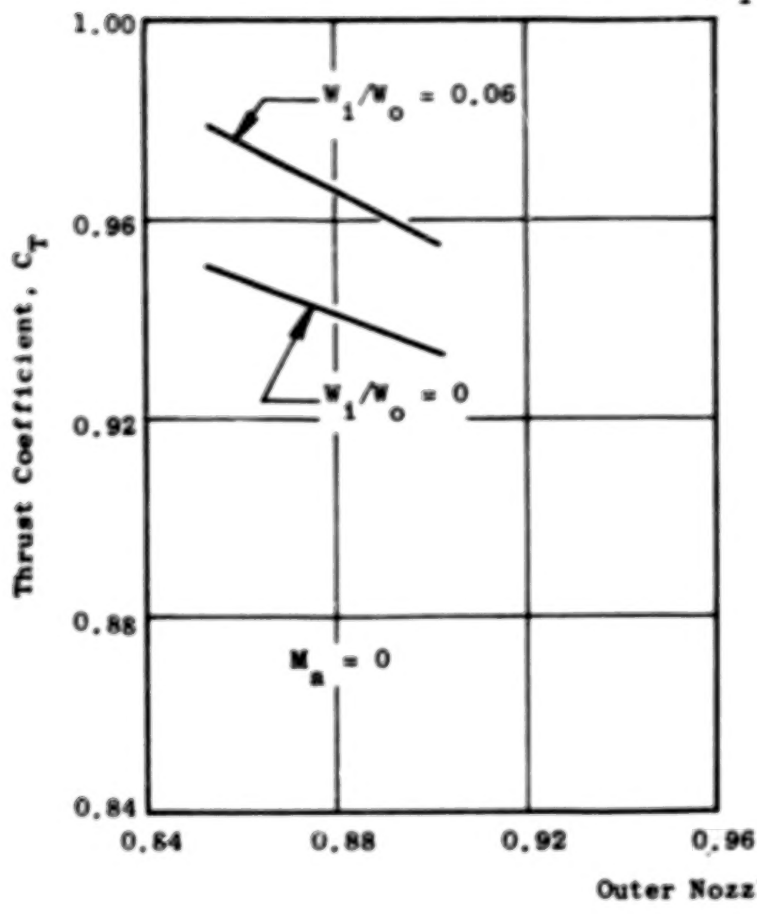


Figure 39. Thrust Coefficient as a Function of Outer Nozzle Radius Ratio for Low Inner Flow Rates and Bent Inner Plug.

$$\bullet \quad P_{T_0}/P_a = 2.5$$

$$\bullet \quad (R_r)_1 = 0.8, \text{ Bent Plug}$$

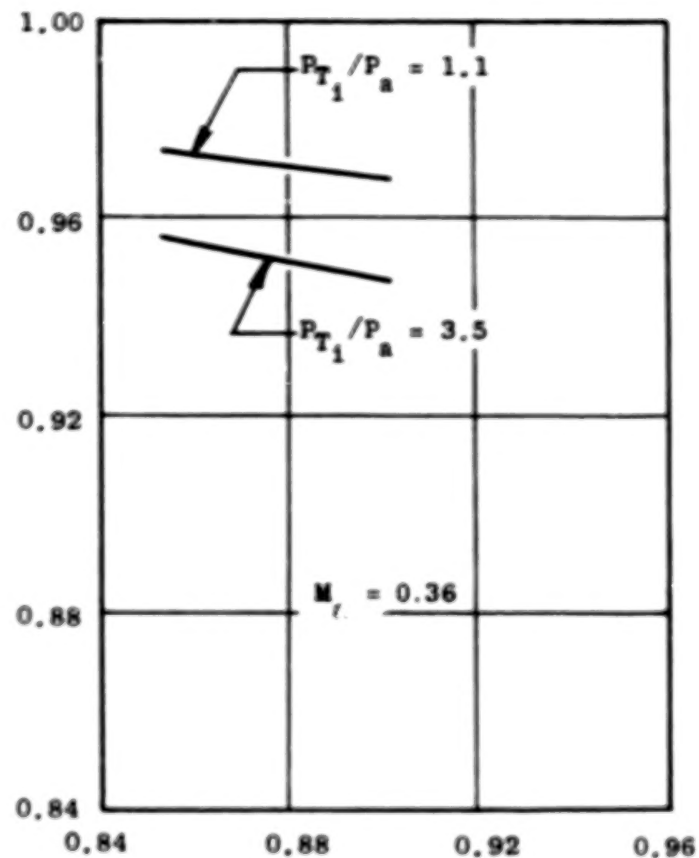
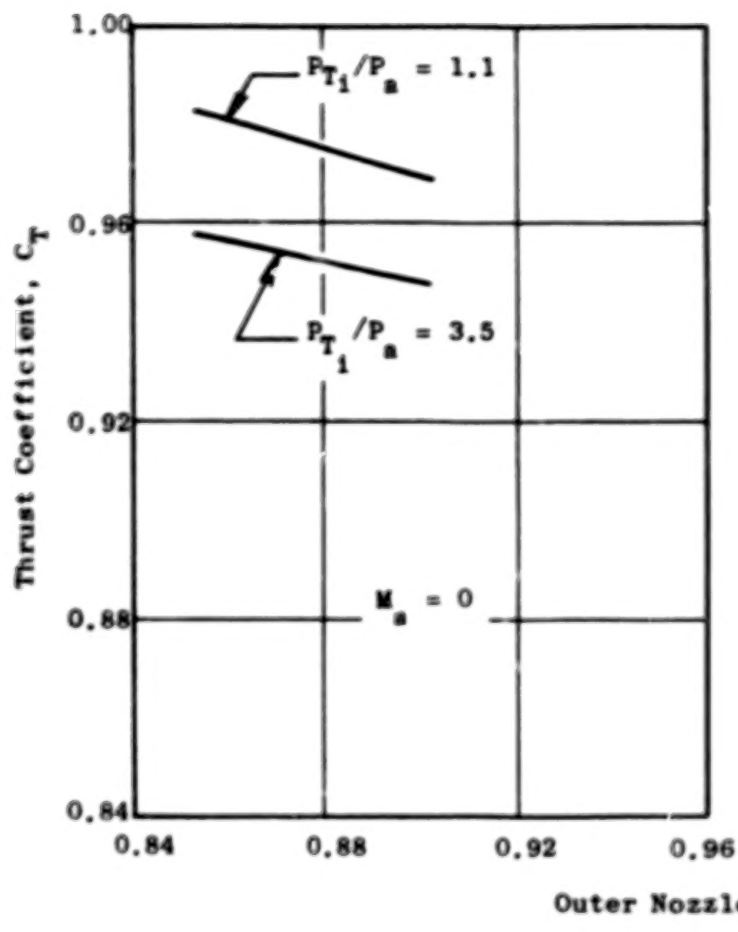


Figure 40. Thrust Coefficient as a Function of Outer Nozzle Radius Ratio for High Inner Flow Rates and Bent Inner Plug.

$$\bullet \quad P_{T0}/P_a = 2.5$$

$$\bullet \quad (R_r)_0 = 0.902$$

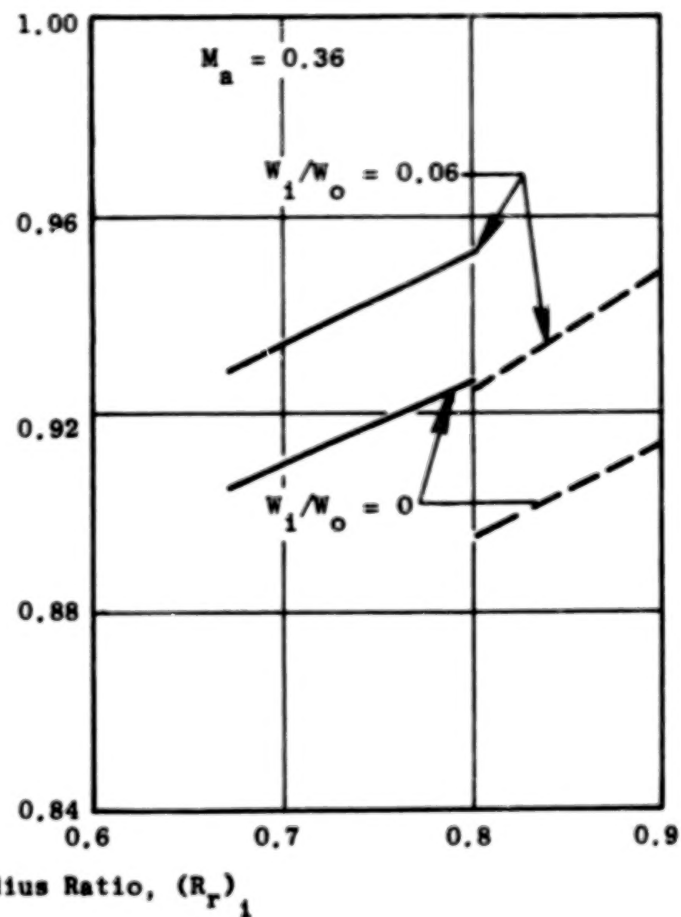
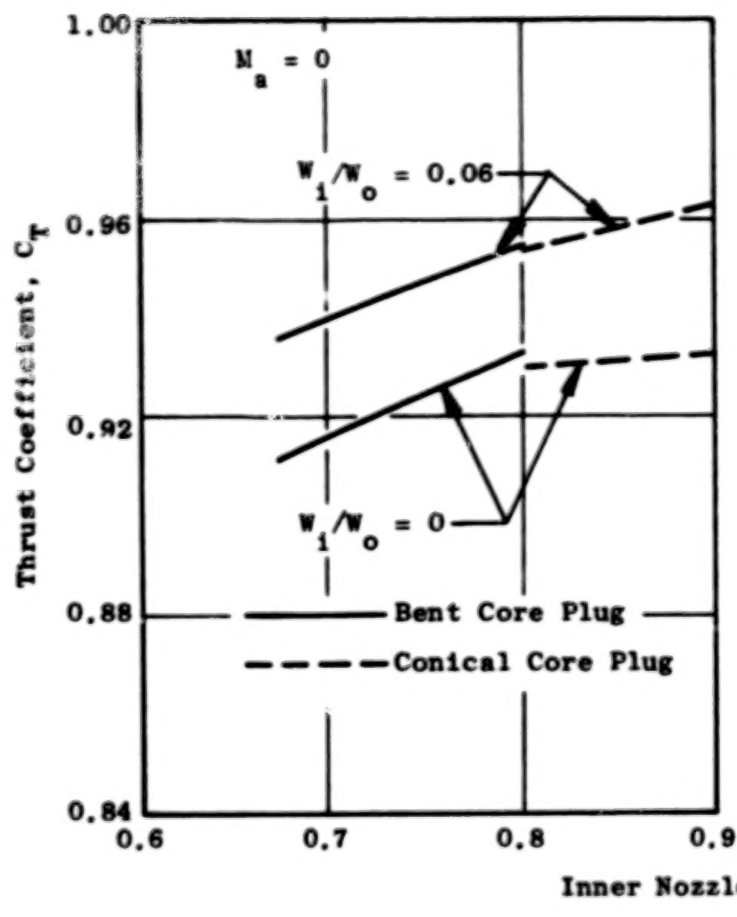


Figure 41. Thrust Coefficient as a Function of Inner Nozzle Radius Ratio for Low Inner Flow Rates,  $(R_r)_0 = 0.902$ .

$$\bullet P_{T_o}/P_a = 2.5$$

$$\bullet (R_r)_o = 0.853$$

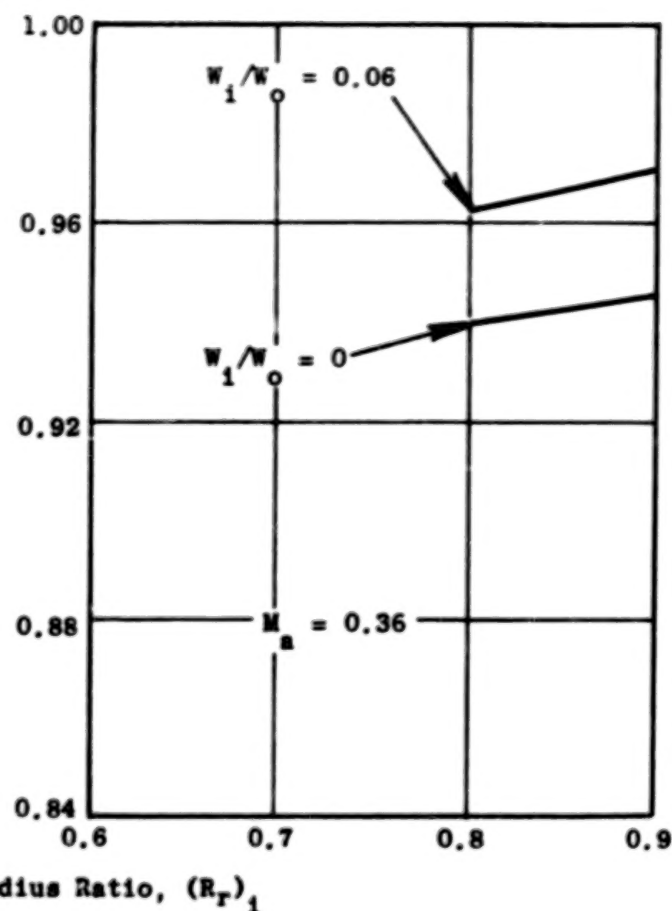
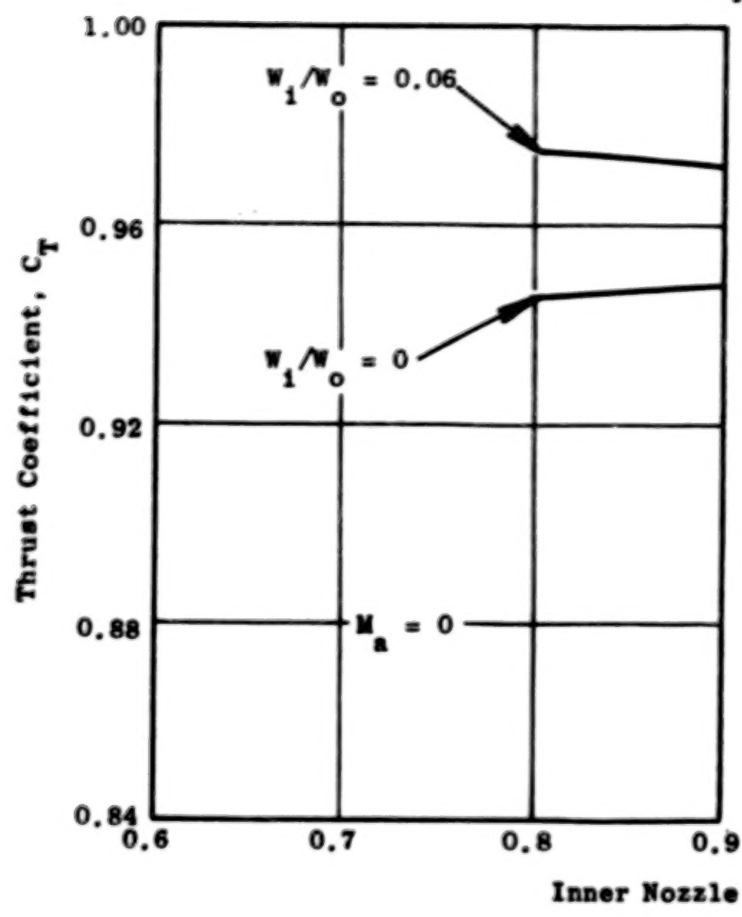


Figure 42. Thrust Coefficient as a Function of Inner Nozzle Radius Ratio for Low Inner Flow Rates,  $(R_r)_o = 0.853$ .

The thrust coefficient, in general, increases as the inner nozzle radius ratio is increased: this trend being more pronounced at Mach number 0.36 than during static operation. This trend is attributed to the fact that at the low inner flow rates the total pressure of the inner airstream is actually lower than the ambient static pressure due to the outer flow stream aspirating the inner stream. This subambient pressure region is a drag force, lowering the nozzle thrust coefficient. The higher inner nozzle radius ratio configurations have smaller inner throat areas, resulting in a smaller low pressure region and less drag. Also, the smaller step-height configurations recover higher pressure force on the inner plug with no change in the pressure forces on the outer plug and shroud. The low static pressures in the region of the inner nozzle throat can be seen in Figure 43 for Configuration 2  $[(R_r)_o = 0.902, (R_r)_i = 0.8, \text{conical inner plug}]$  with zero inner flow. The greater pressure recovery on the inner plug for smaller step heights is shown by comparing the static pressure distribution in Figure 43 with that of Configuration 3  $[(R_r)_o = 0.902, (R_r)_i = 0.902, \text{conical inner plug}]$  in Figure 44. The plug recompression occurs much earlier, thus acting on a larger projected area, for the 0.902 inner radius ratio than for the 0.80 ratio. Plots of the total inner plug pressure force from pressure integrations, and normalized by the nozzle ideal thrust (see Section 5.5), are shown in Figure 45 for models 2 and 3 demonstrating the increase in plug pressure recovery.

Plots for high inner flow rates showing the effect on thrust coefficient of inner nozzle radius ratio are presented in Figures 46 and 47. The effect here is less than for the low flow condition, and the trend is generally toward slightly decreasing thrust coefficient at the higher radius ratios. This is probably caused by the greater plug size at the larger radius ratio which increases the friction losses.

### 6.2.3 Effect of Inner Nozzle Flow Rate and Pressure Ratio

4 Figures 48 and 49 show nozzle thrust coefficient plotted as a function of inner-to-outer nozzle weight flow ratio for low inner flow rates. With zero inner flow, the outer stream pumping action lowers the static pressure

- $P_{T_o}/P_a = 2.5$

- $W_1/W_o = 0$

- $M_a = 0.36$

- $DM = 0.203 \text{ m (8.0 in.)}$

Symbol	Tap Location
--------	--------------

○	Outer Shroud
---	--------------

□	Outer Plug
---	------------

△	Inner Plug
---	------------

Note:  $X/DM = 0$  at Outer Nozzle Throat Axial Location

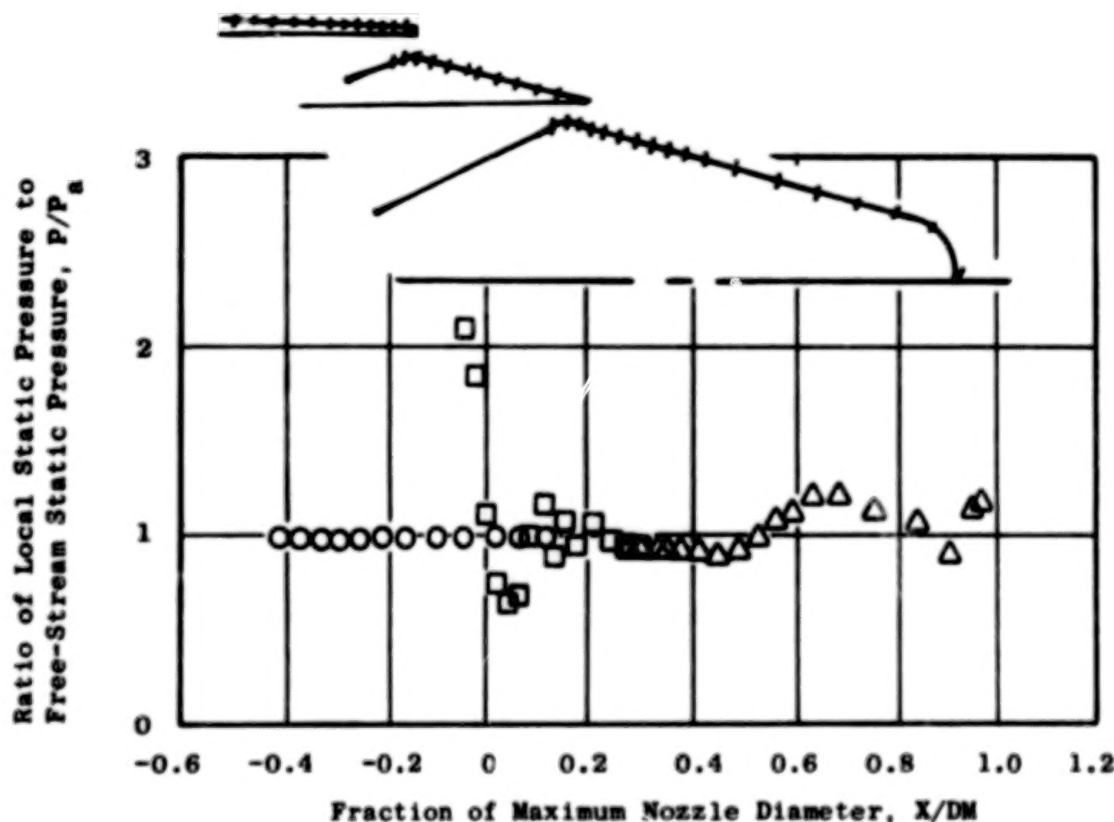


Figure 43. Static Pressure Distribution, Configuration 2 [ $(R_r)_o = 0.902$ ,  $(R_r)_i = 0.8$ , Conical Inner Plug] with Zero Inner Flow.

$$\bullet \quad P_{T_o}/P_a = 2.5$$

$$\bullet \quad W_1/W_o = 0$$

$$\bullet \quad M_a = 0.36$$

$$\bullet \quad DM = 0.203 \text{ m (8.0 in.)}$$

Symbol	Tap Location
--------	--------------

○	Outer Shroud
---	--------------

□	Outer Plug
---	------------

△	Inner Plug
---	------------

Note:  $X/DM = 0$  at Outer Nozzle Throat Axial Location

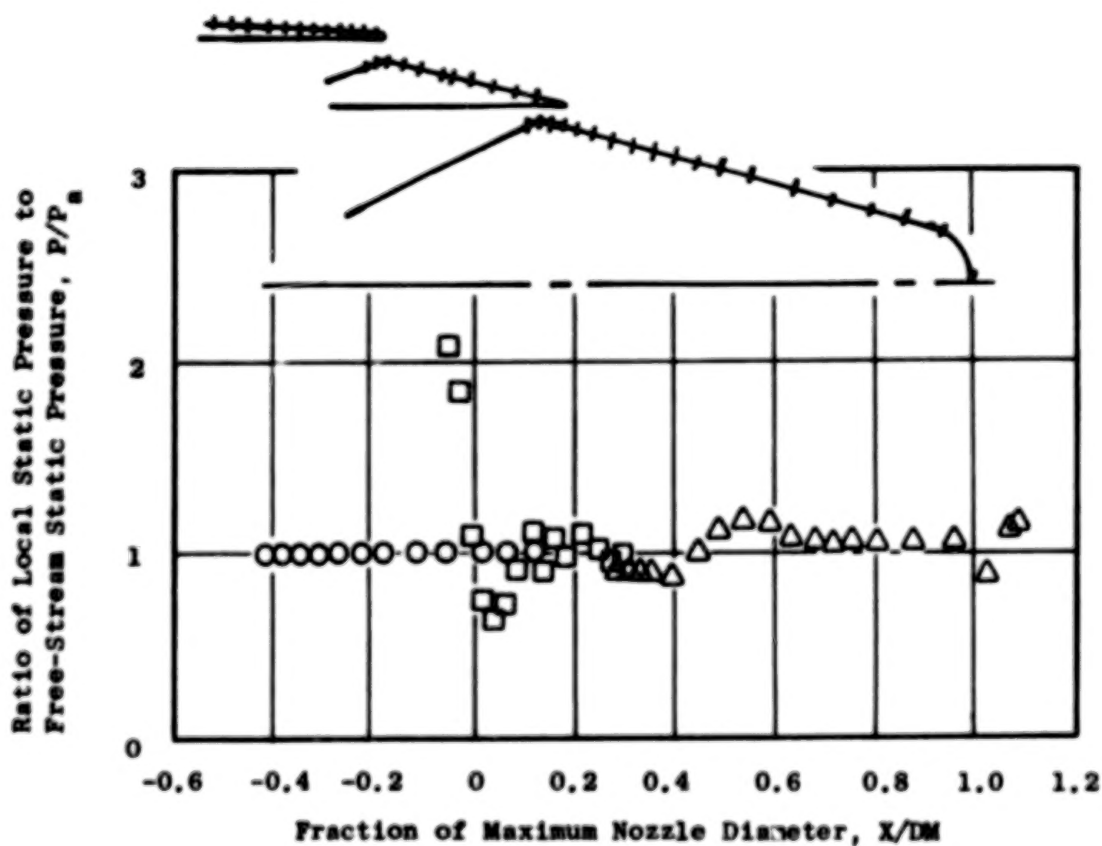


Figure 44. Static Pressure Distribution, Configuration 3 [ $(R_r)_o = 0.902$ ,  $(R_r)_i = 0.902$ , Conical Inner Plug] with Zero Inner Flow.

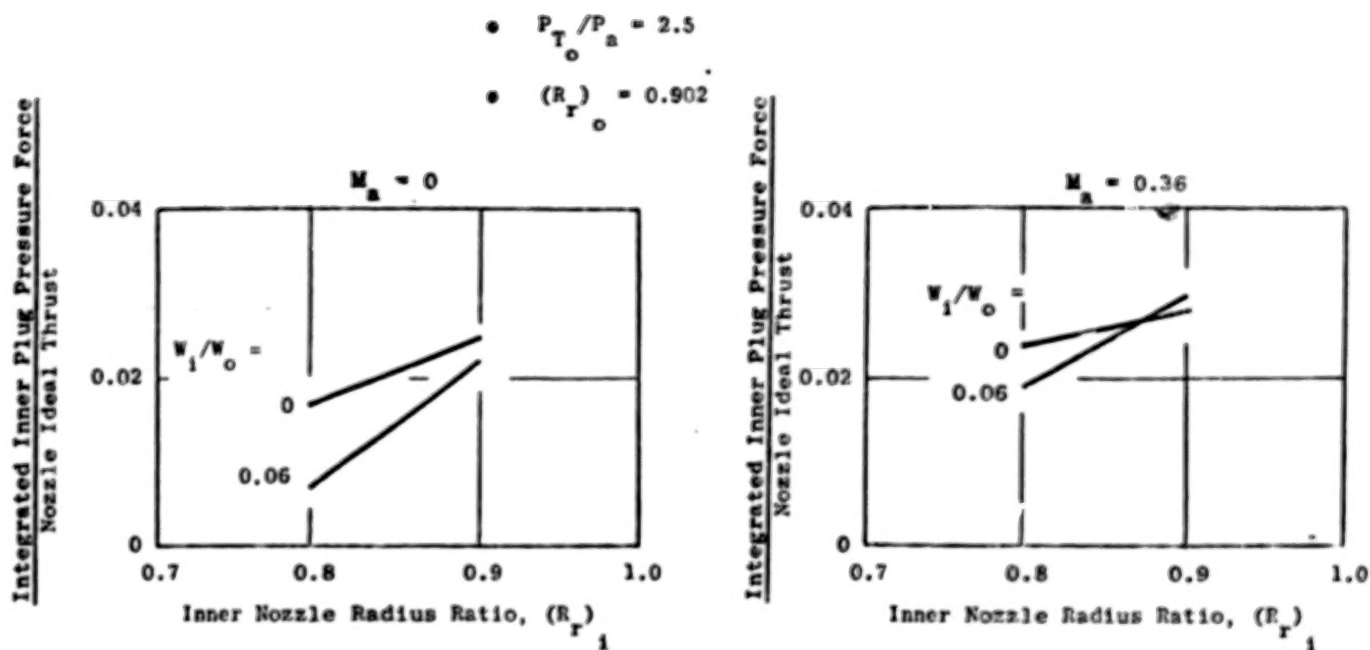


Figure 45. Integrated Inner Plug Pressure Force as a Function of Inner Nozzle Radius Ratio for Low Inner Flow Rates.



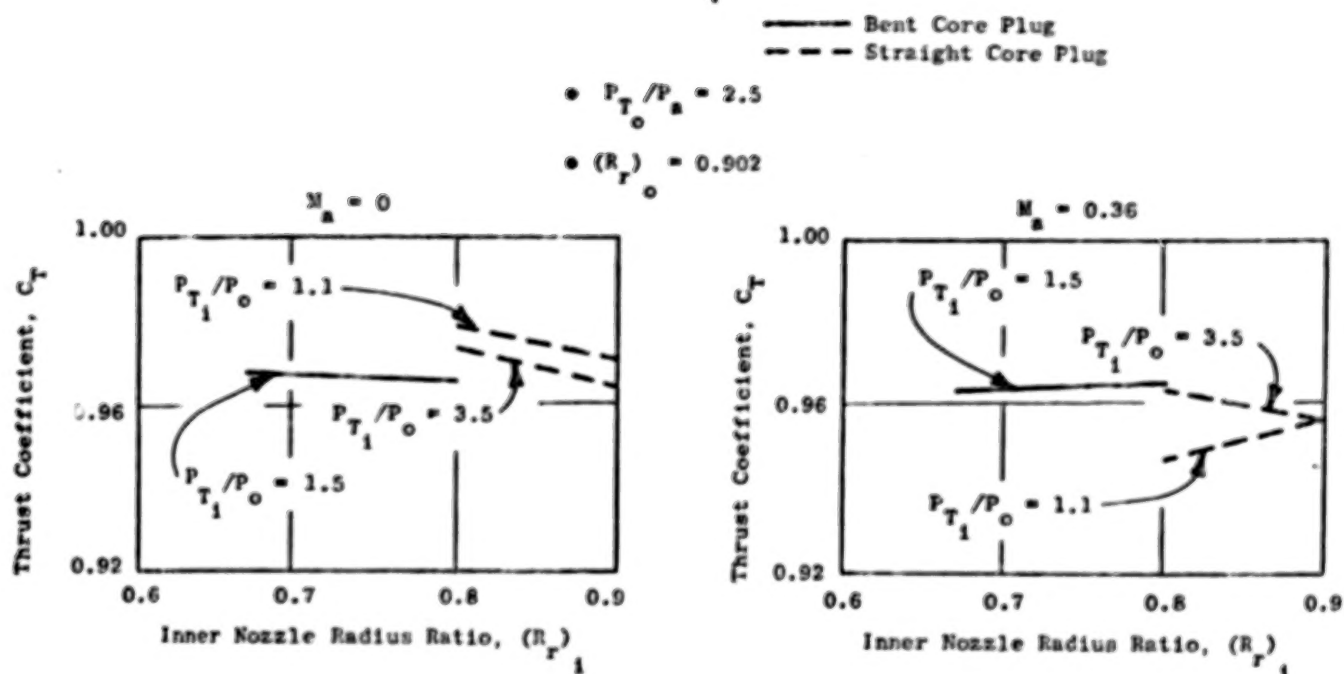


Figure 46. Thrust Coefficient as a Function of Inner Nozzle Radius Ratio for High Inner Flow Rates,  $(R_r)_o = 0.902$ .

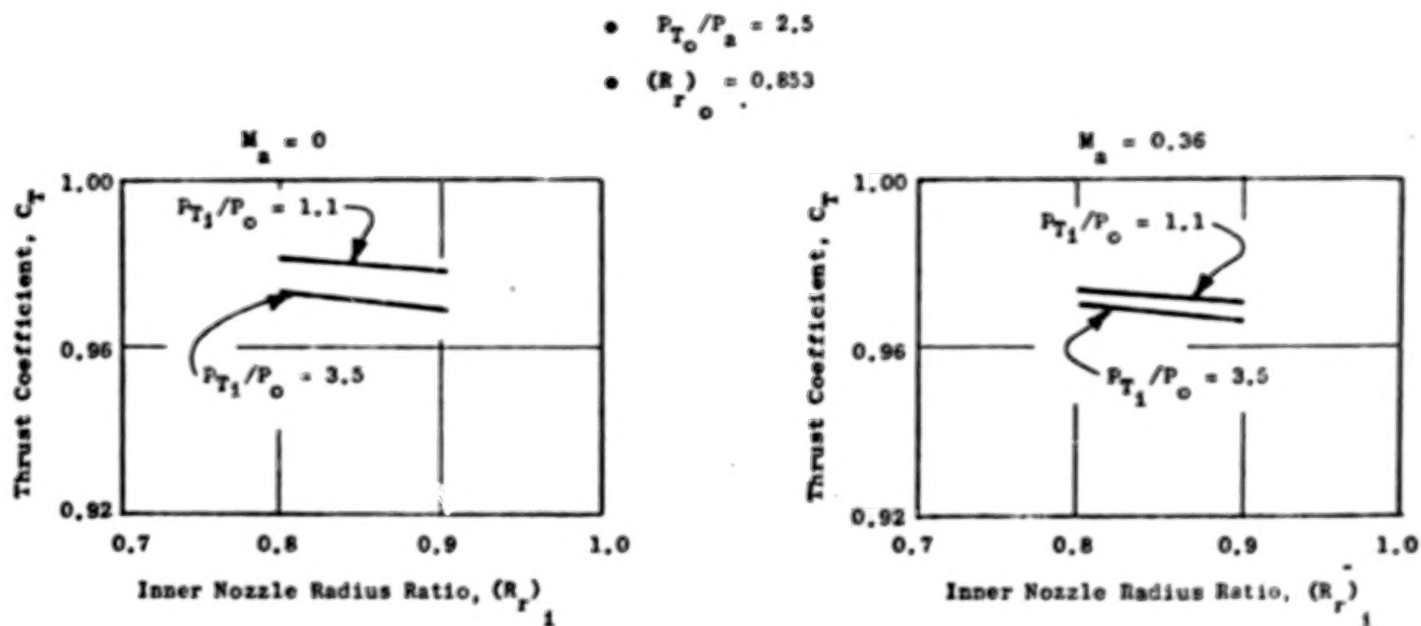


Figure 47. Thrust Coefficient as a Function of Inner Nozzle Radius Ratio for High Inner Flow Rates,  $(R_{r_0}) = 0.853$ .

- $M_a = 0$
- $P_{T_o}/P_a = 2.5$

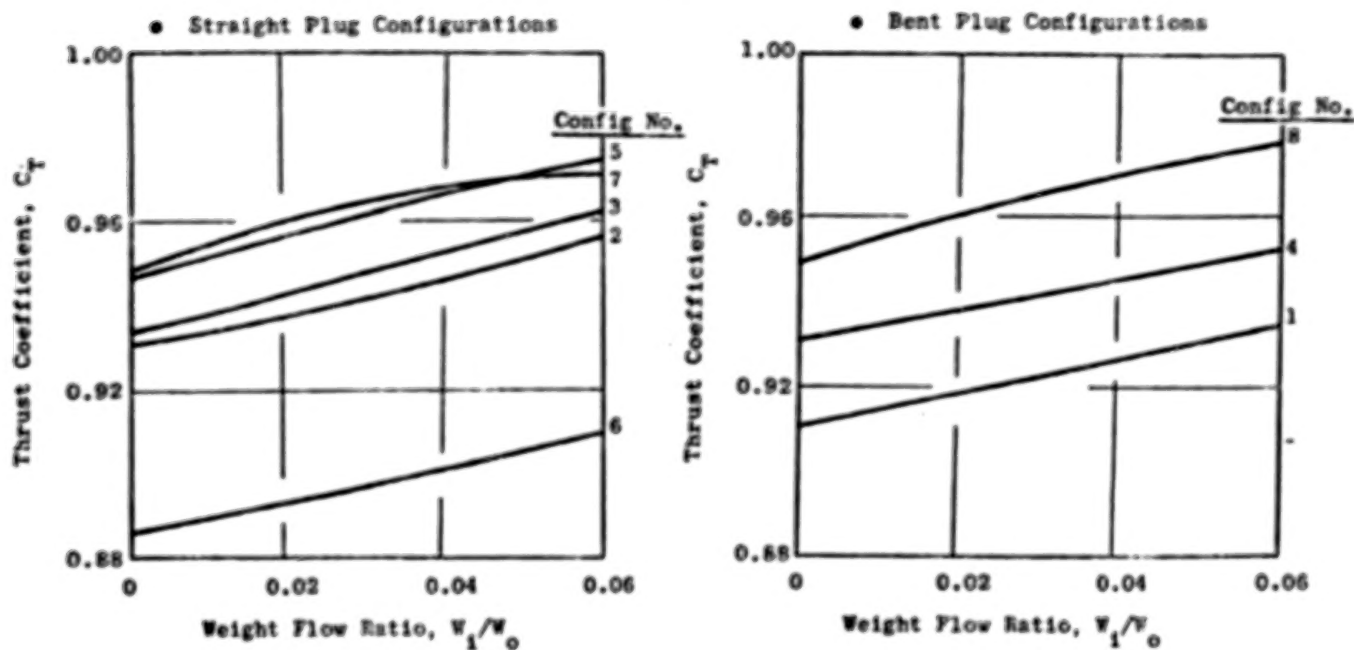


Figure 48. Thrust Coefficient as a Function of Inner Weight Flow for Low Inner Flow Rates,  $M_a = 0$ .

$$\bullet M_a = 0.36$$

$$\bullet P_{T_0}/P_a = 2.5$$

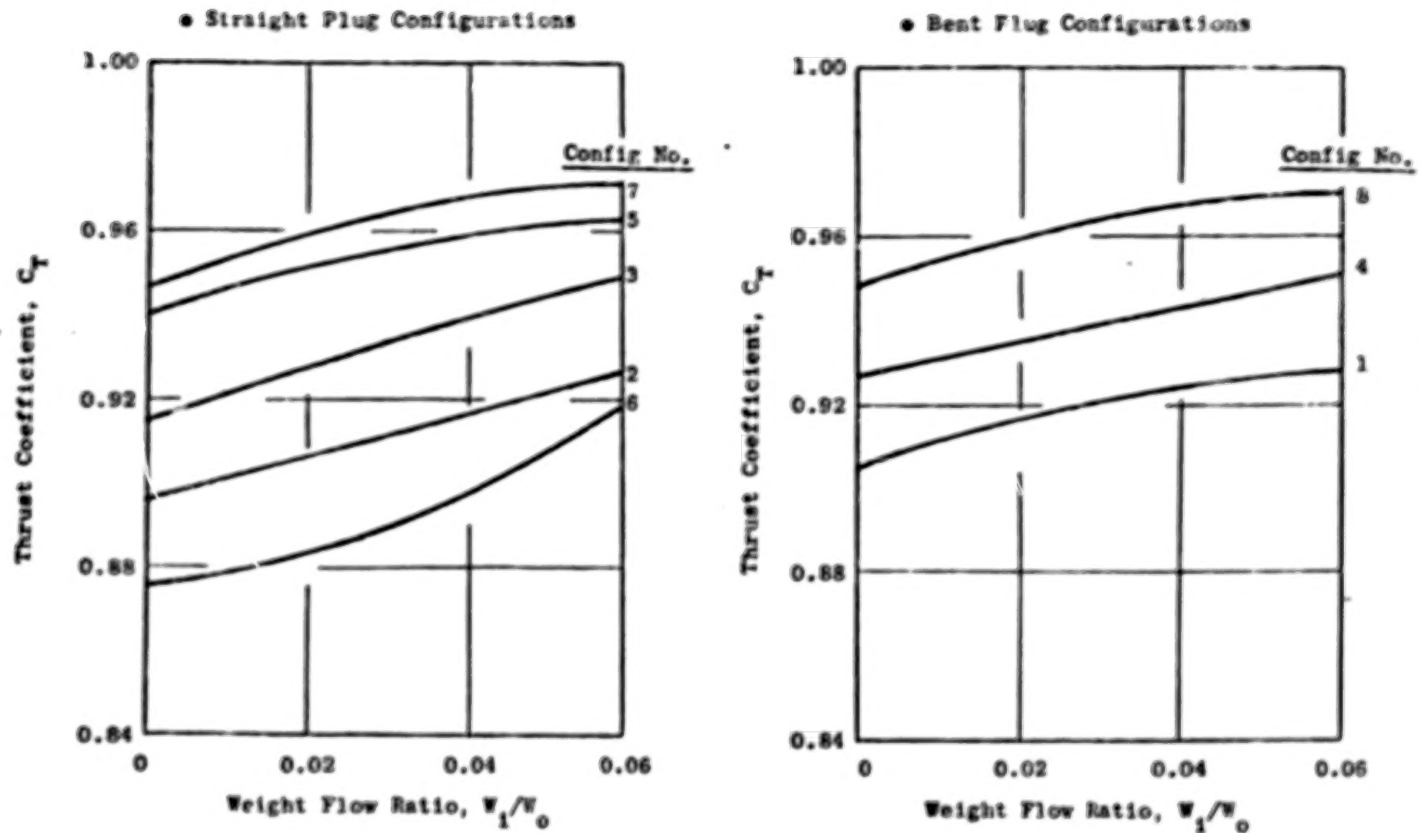


Figure 49. Thrust Coefficient as a Function of Inner Weight Flow for Low Inner Flow Rates,  $M_a = 0.36$ .

in the region of the inner nozzle throat (i.e., minimum physical area) to lower than ambient levels. In this instance, the cavity pressure upstream of the inner nozzle throat, as measured by the total pressure rakes, ranges from 0.85 to 0.92 of the ambient pressure. This subambient pressure is a drag force reflected in a loss in thrust coefficient. As the inner flow rate increases from zero, the total pressure of the inner stream and the static pressure in the region of the throat steadily increase. The total-to-ambient pressure ratio at 6% flow ratio ranges from 0.96 to 1.02. This steady decrease in pressure drag is reflected by the steadily increasing thrust coefficient for all configurations, as depicted in Figures 48 and 49. The increase in static pressure in the throat region of the inner nozzle, as the inner weight flow ratio is increased successively from 0 to 0.03 and to 0.06, is demonstrated in Figure 50 which shows the static pressure distributions for Configuration 6.

The variation of thrust coefficient with inner nozzle pressure ratio for high inner flow rates is illustrated in Figures 51 and 52 for all configurations at an outer nozzle pressure ratio of 2.5. The thrust coefficient does not vary greatly with inner pressure ratio for the conical plug configurations but steadily decreases with increasing inner pressure ratio for the bent inner plug geometries. This is due to expansion around the corner in the plug downstream of the throat, resulting in a low pressure area, the severity of which increases as the inner nozzle pressure ratio increases. This is illustrated in Figure 53 where the integrated pressure force on the inner plug divided by the total nozzle ideal thrust is plotted against inner nozzle pressure ratio for Configurations 2 (conical plug) and 4 (bent plug) for an outer pressure ratio of 2.5 and tunnel Mach number of 0.36. The decrease in plug pressure force as a percentage of ideal thrust is seen to be initially much more rapid for the bent plug, being 1% lower in plug thrust than the conical plug at an inner pressure ratio of 1.1 and 3% lower at a pressure ratio of 2.5.

Static pressure distributions for Configurations 2 and 4 at Mach 0.36, with an outer nozzle pressure ratio of 2.5 and inner nozzle pressure ratios of 1.1, 2.5, and 3.5, are shown in Figures 54, 55, and 56. For the inner pressure ratio 1.1 shown in Figure 54, the conical plug, Configuration 2,

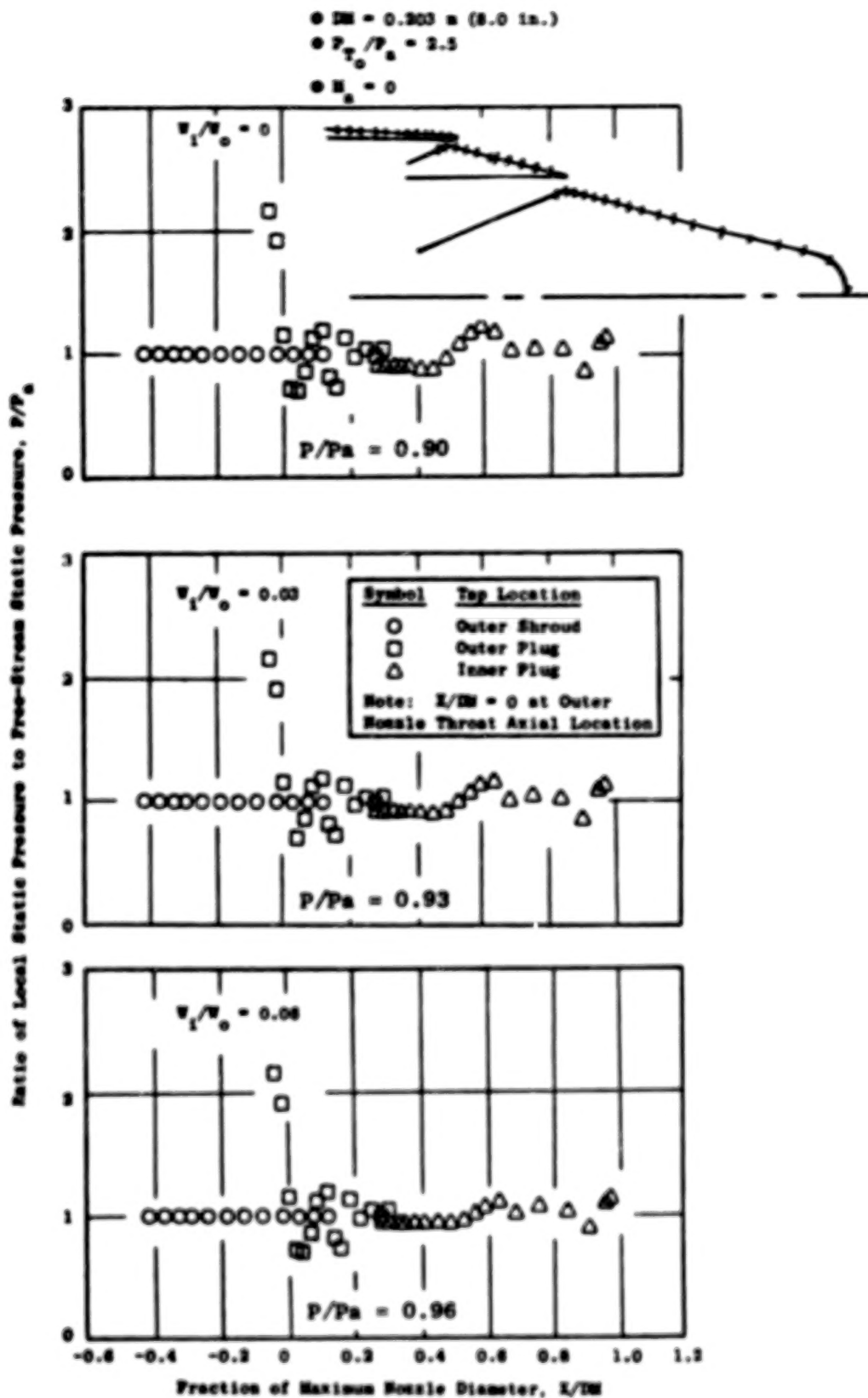
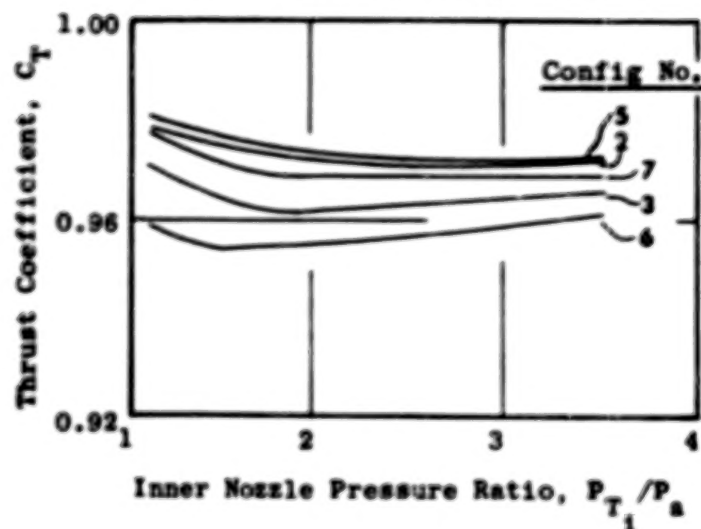


Figure 50. Static Pressure Distributions, Configuration 6 [ $(R_r)_0 = 0.926$ ,  $(R_r)_1 = 0.8$ , Conical Inner Plug] for Low Inner Flow Rates.

- $M_a = 0$
- $P_{T_0}/P_a = 2.5$

• Straight Plug Configurations



• Bent Plug Configurations

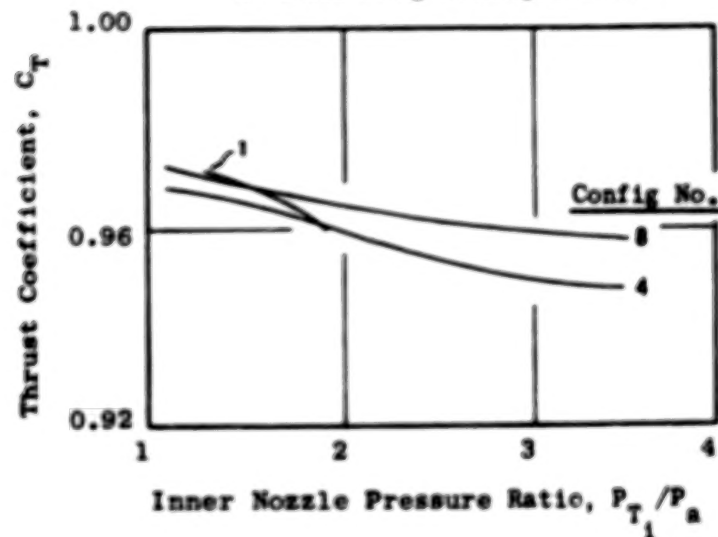


Figure 51. Thrust Coefficient as a Function of Inner Nozzle Pressure Ratio for High Inner Nozzle Pressure Ratio for High Inner Flow Rates,  $M_a = 0$ .

$$\bullet M_a = 0.36$$

$$\bullet P_{T_o}/P_a = 2.5$$

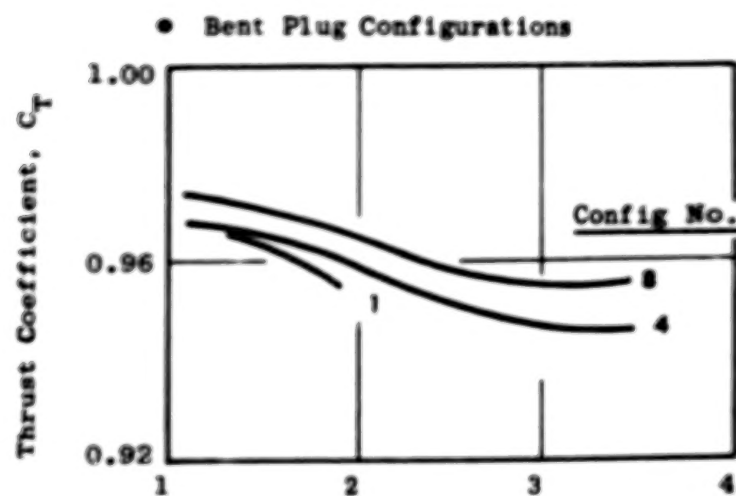
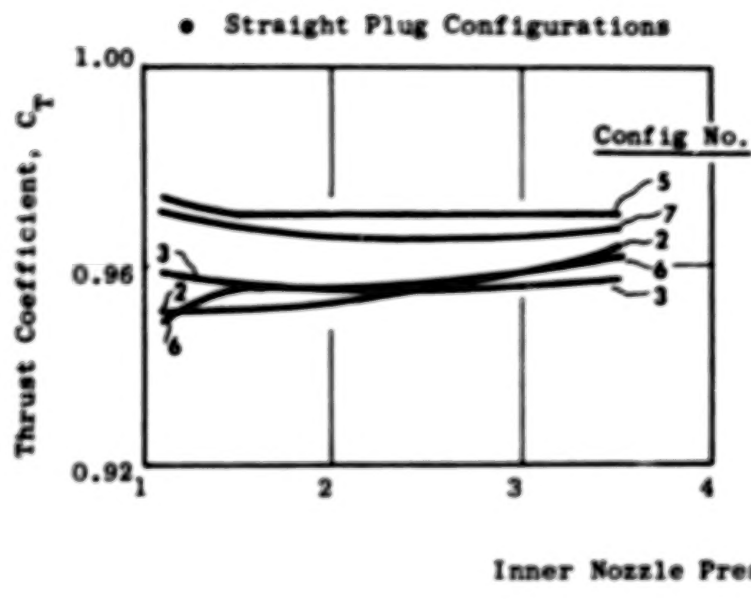


Figure 52. Thrust Coefficient as a Function of Inner Nozzle Pressure Ratio for High Inner Flow Rates,  $M_a = 0.36$ .



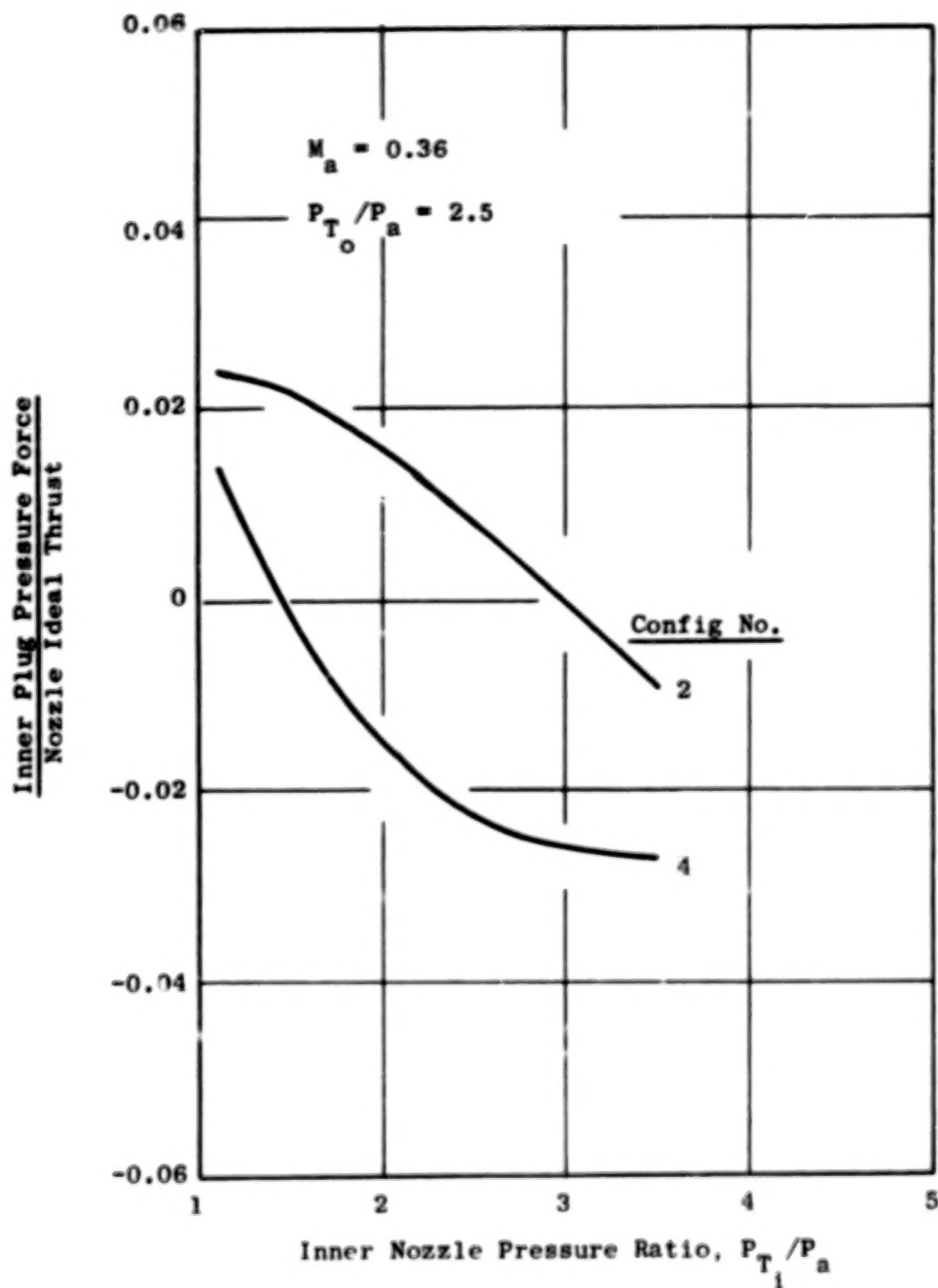


Figure 53. Inner Plug Integrated Pressure Force as a Function of Inner Nozzle Pressure Ratio for High Inner Flow Rates.

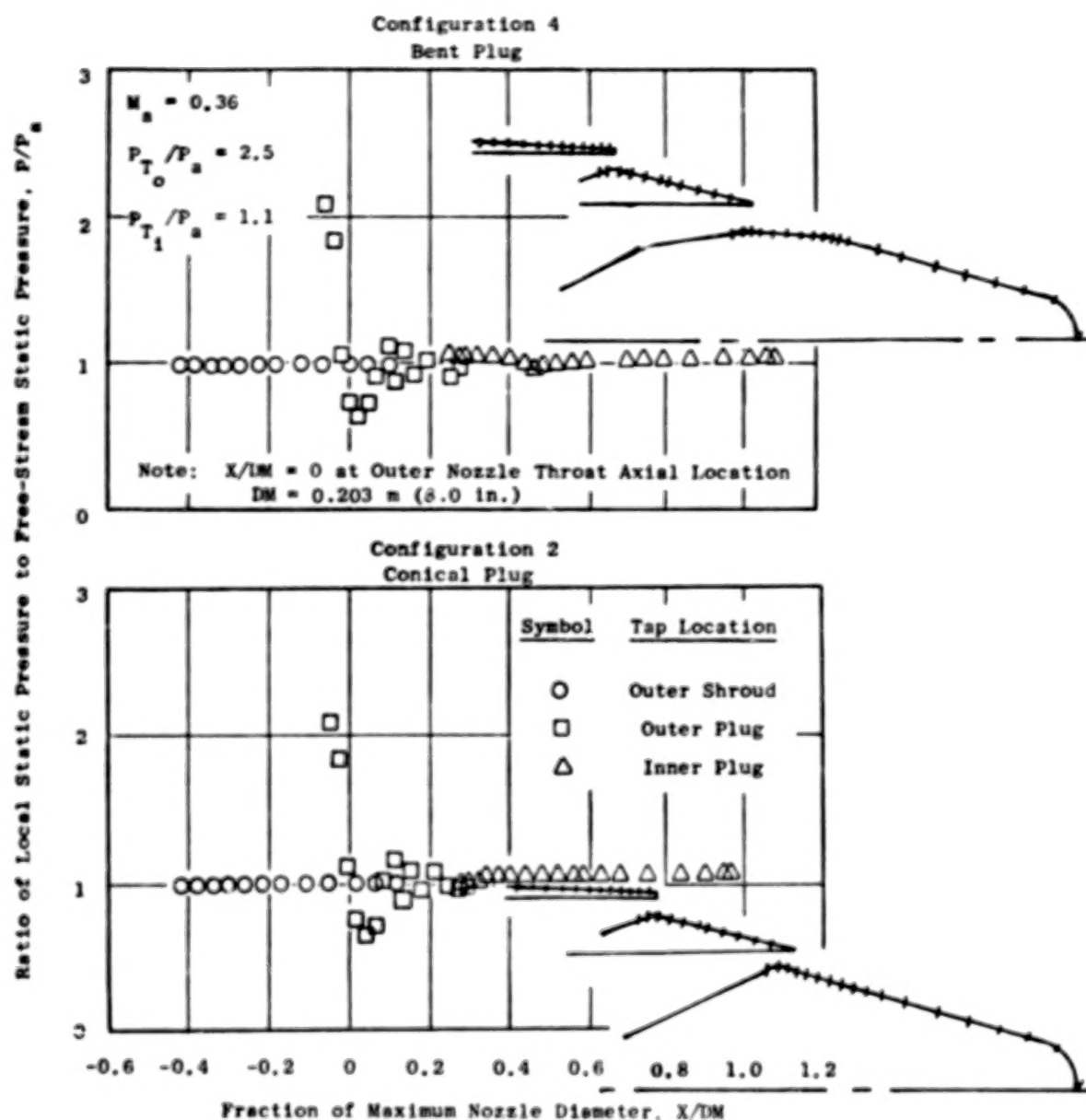


Figure 54. Static Pressure Distributions, Configurations 2 and 4, High Inner Flow,  $P_{T_i}/P_a = 1.1$ .

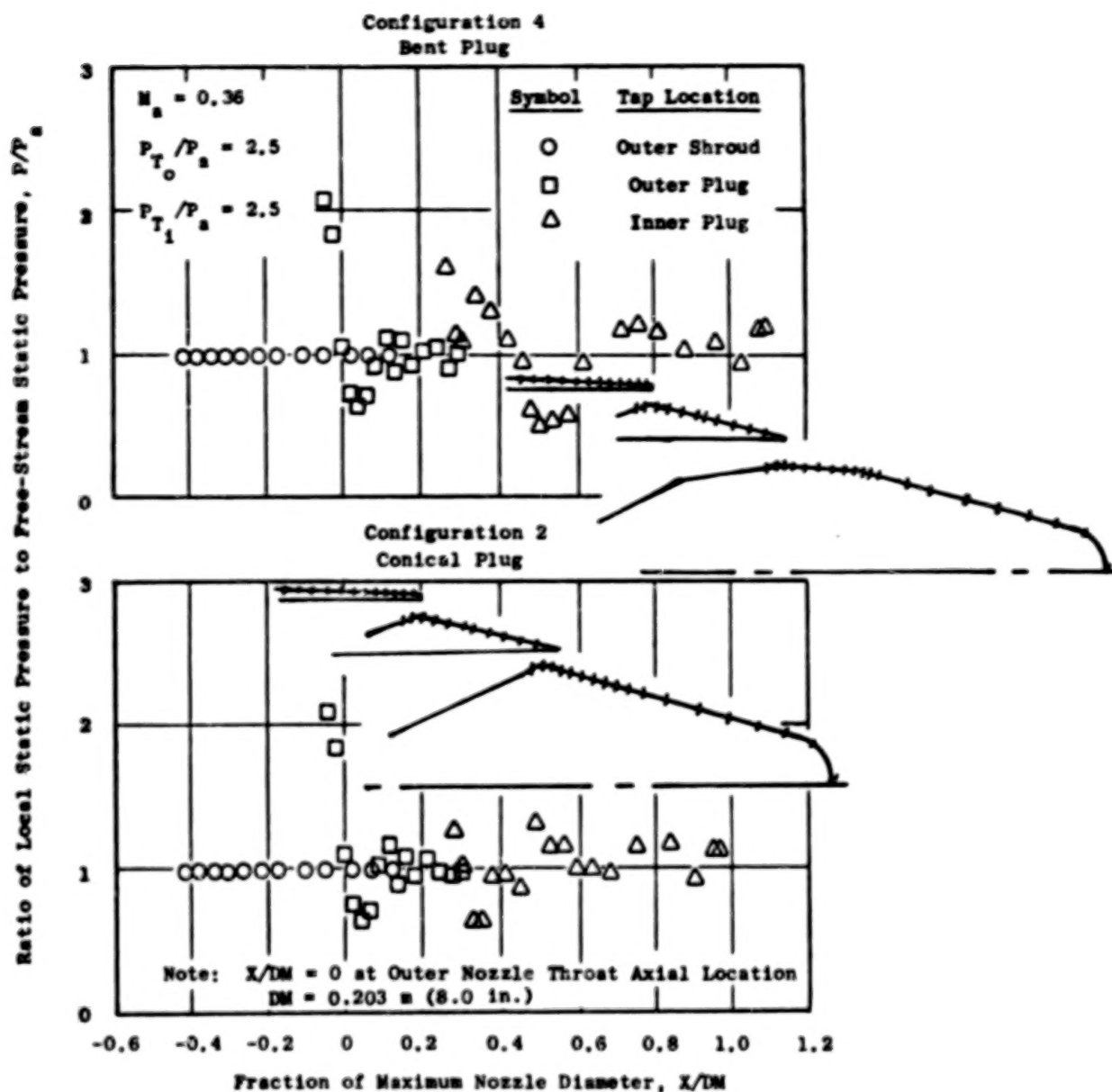


Figure 55. Static Pressure Distributions, Configurations 2 and 4, High Inner Flow,  $P_{T1}/P_a = 2.5$ .

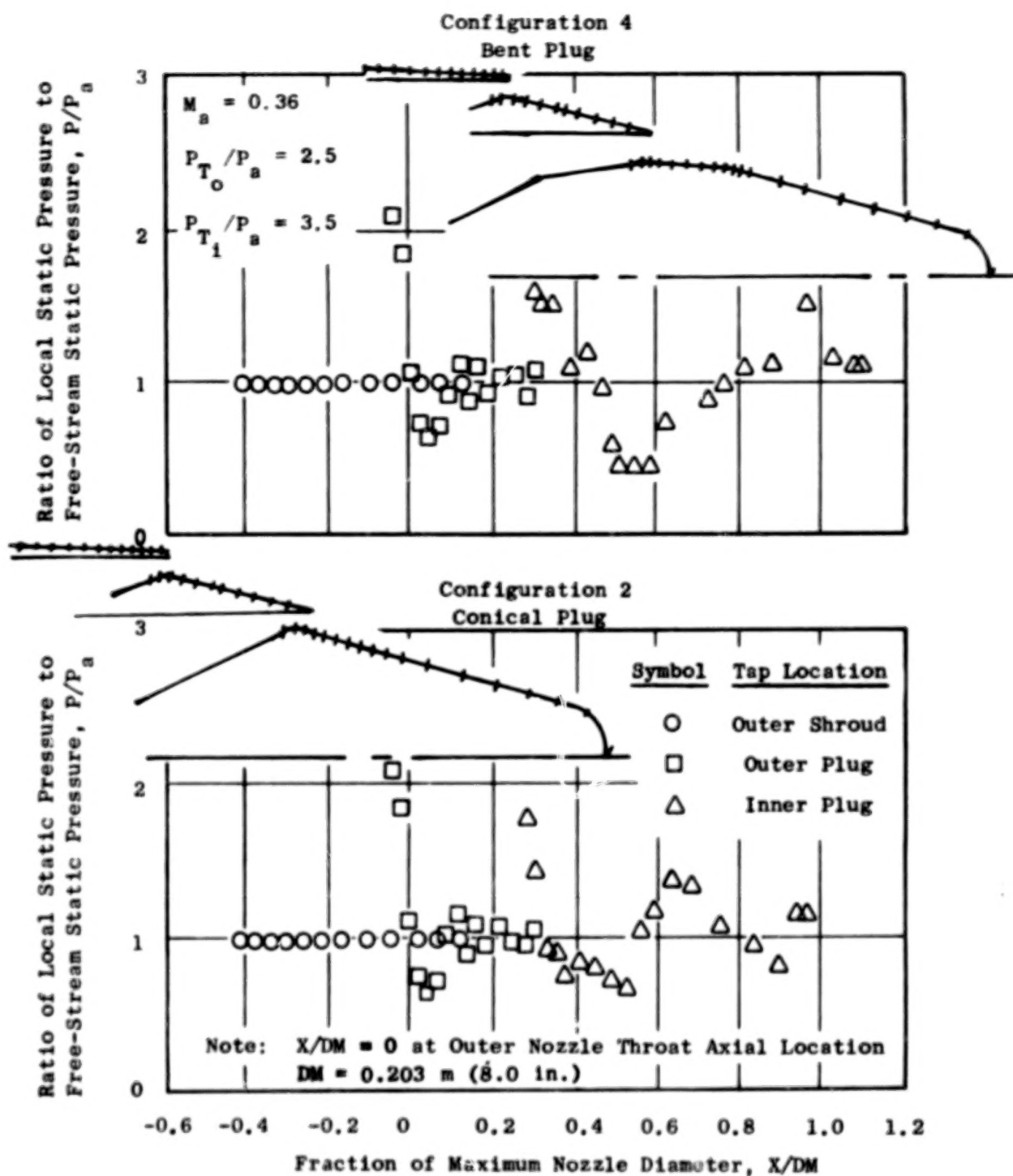


Figure 56. Static Pressure Distributions, Configurations 2 and 4, High Inner Flow,  $P_{T_1}/P_a = 3.5$ .

exhibits a slight expansion in the throat region with constant pressure downstream. The bent plug, Configuration 4, shows higher pressure in the throat region, followed by an expansion around the corner in the plug aft of the throat. At the higher inner nozzle pressure ratios, Figures 55 and 56, the conical nozzle has an expansion in the throat region followed by a fluctuating distribution. The bent inner plug configuration shown in these figures exhibits higher pressures in the throat region and a large sub-ambient pressure region caused by expansion around the corner.

#### 6.2.4 Effect of External Mach Number

The effect of ambient velocity on the models was not generally severe due to the small amount of boattailing required for these nozzles. Figure 57 presents some typical variations of thrust coefficient with tunnel Mach number for low inner flow rates. The outer radius ratio 0.902 model with the conical inner plug, Configuration 2, shows a degradation of 3-3.5% in performance between Mach 0 and 0.45. The bent plug configuration, as well as the 0.853 outer radius ratio configurations, exhibit only a 0.5-1.0% loss over the same range. The ambient velocity has the effect of lowering the static pressures on the outer plug and increasing the inner plug pressures. This is shown in Figures 58 and 59 for Configurations 4, 2, 5, and 8, where the integrated pressure forces on the plugs are normalized by the nozzle ideal gross thrust and plotted against tunnel Mach number. For these configurations, the decrease in thrust on the outer plug is approximately compensated for by the increase in inner plug thrust. As a consequence of the way the outer radius ratio was varied in these models, the amount of shroud boattail drag varies between the different outer radius ratio configurations. The boattail angle, and the amount of boattail area, increases with increasing radius ratio while the nozzle throat area decreases. This causes the boattail drag to increase, and the nozzle ideal thrust to decrease, causing a larger effect of boattail pressure drag on the thrust coefficient at the higher radius ratios. This is illustrated in Figure 60 for low inner flow rates.

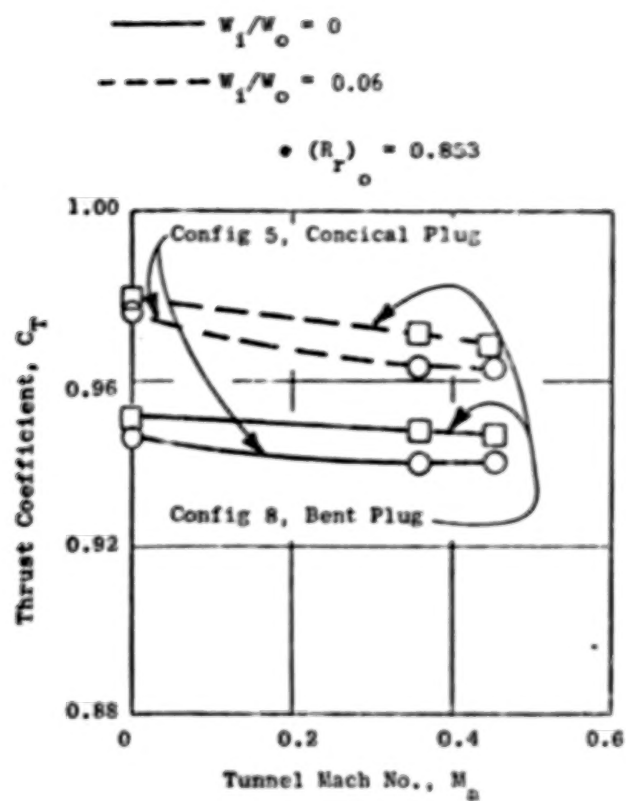
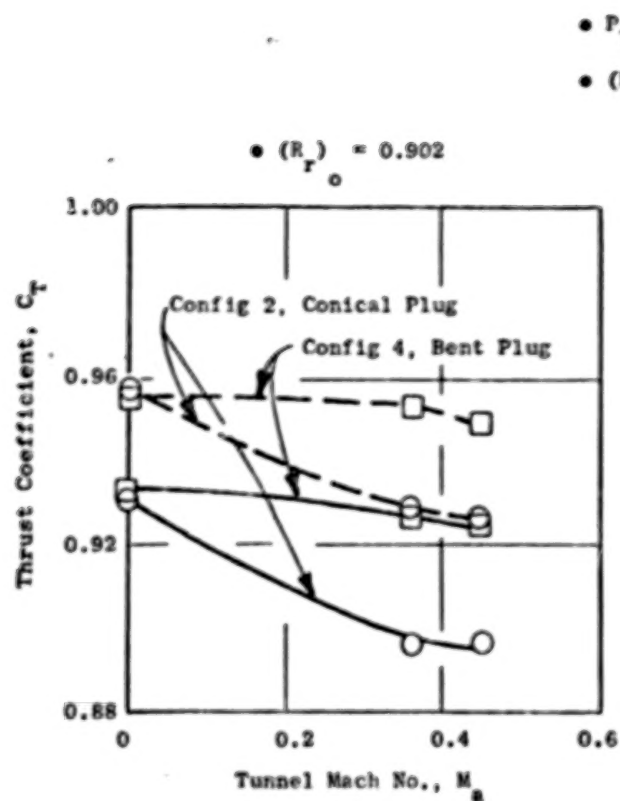


Figure 57. Thrust Coefficient as a Function of Tunnel Mach No. for Low Inner Flow Rates.

$$\bullet P_{T_0}/P_a = 2.5$$

$$\bullet W_1/W_0 = 0.06$$

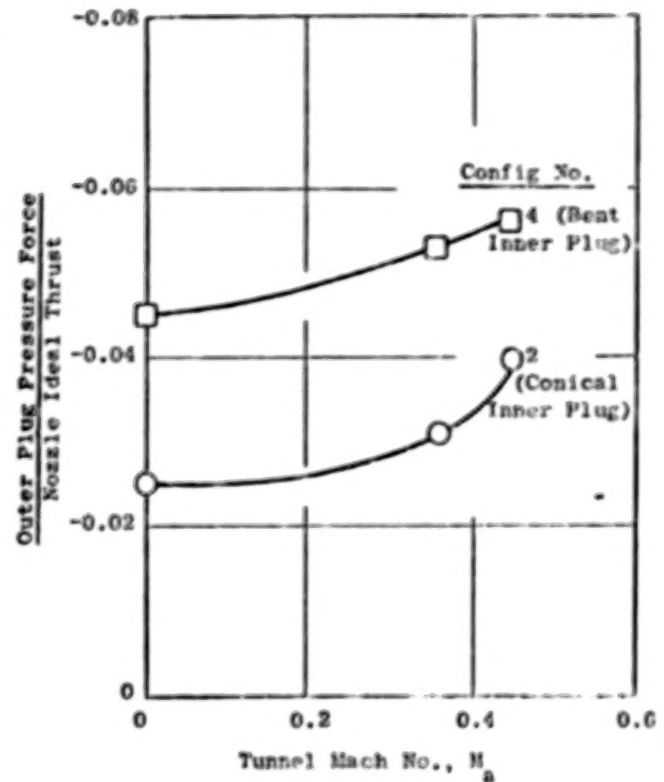
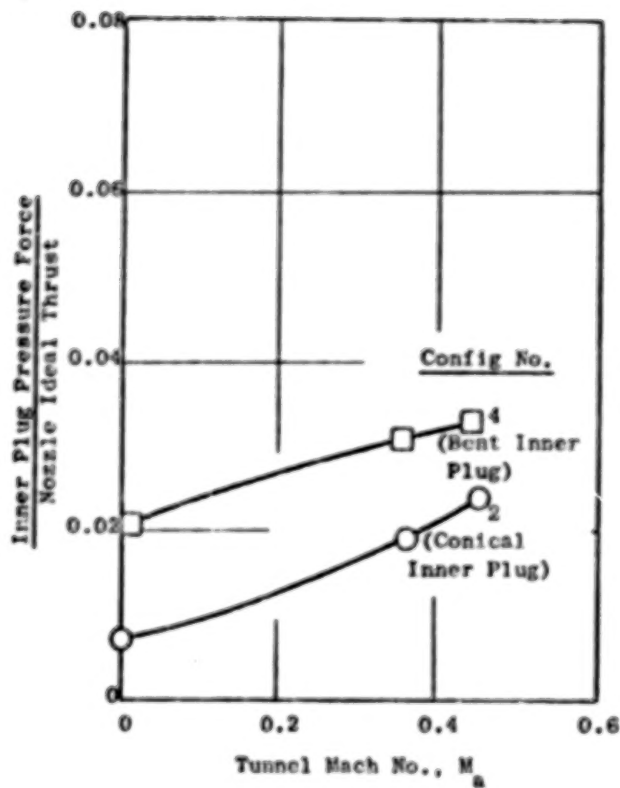


Figure 58. Inner Plug and Outer Plug Integrated Pressure Forces as a Function of Tunnel Mach No. for Low Inner Flow Rates,  $[(R_r)_0 = 0.903, (R_r)_1 = 0.8]$ .

$$\bullet \quad P_{T_o} / P_a = 2.5$$

$$\bullet \quad W_1 / W_o = 0.06$$

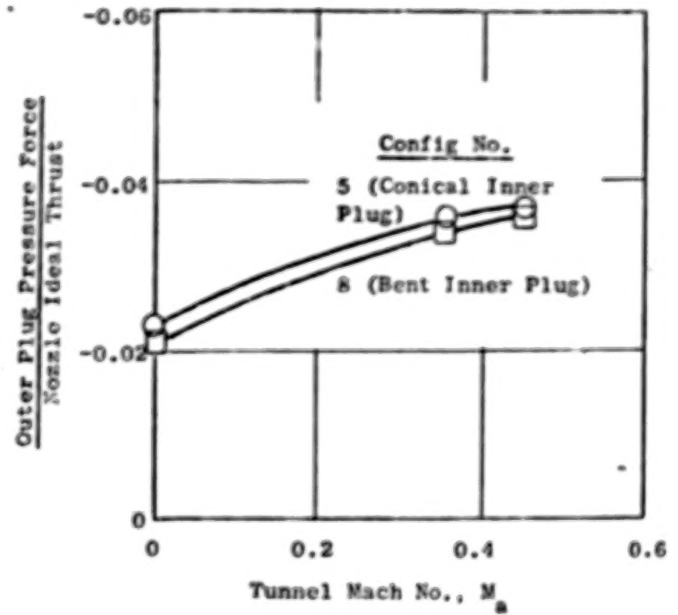
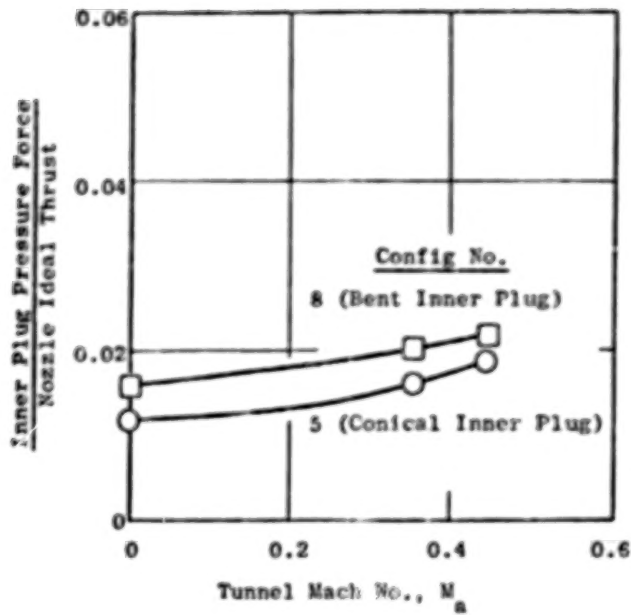


Figure 59. Inner Plug and Outer Plug Integrated Pressure Forces as a Function of Tunnel Mach No. for Low Inner Flow Rates,  $[(R_r)_o = 0.853, (R_r)_i = 0.8]$ .



$$P_{T_o}/P_a = 2.5$$

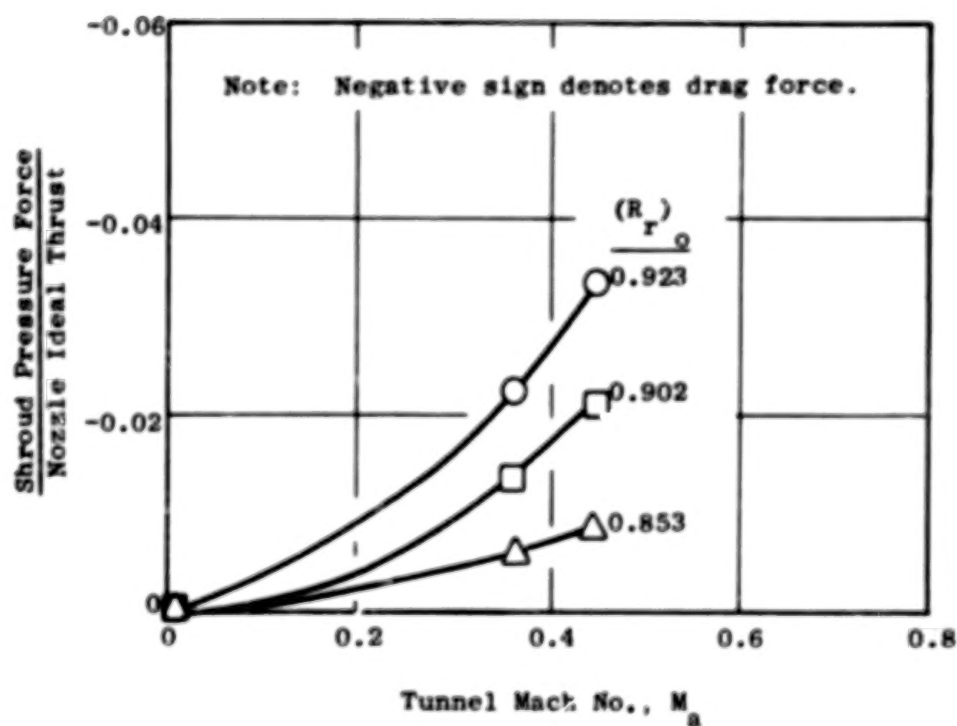


Figure 60. Shroud Drag as a Function of Tunnel Mach No. for Low Inner Flow Rates.

Figure 61 shows the effect of ambient Mach number on the thrust coefficient for Models 2, 4, 5, and 8 with high inner flow rates. The performance loss from static to wind-on is again small, 0.2% to 1.2%, with the exception of Configuration 2 at the low inner pressure ratio setting.

### 6.3 FLOW COEFFICIENTS

Flow coefficients for the outer nozzle are presented in Figure 62. These flow coefficients proved to be independent of both the inner nozzle flow conditions and the tunnel Mach number and are therefore shown only as a function of the outer nozzle pressure ratio for each of the three different outer nozzle geometries. Figures 63 to 70 show the inner nozzle flow coefficients as a function of inner nozzle pressure ratio during high inner flow rate testing. These coefficients did vary somewhat with different external flow conditions, as shown in the figures. For low inner flow tests, the total pressure required to supply the low amounts of air was generally less than ambient pressure due to the aspiration of the inner nozzle by the outer stream. This resulted in a calculated ideal flow rate of zero (see Section 5.4) which rendered the flow coefficient meaningless.

The measured flow coefficients exhibited excellent repeatability, generally within 0.1% to 0.2%, similar to that demonstrated by the STA nozzle. Repeat points are not shown on Figures 62 to 70 for the sake of clarity.

Values of outer nozzle flow coefficient ranged from 0.978 to 0.988 for pressure ratios of 2.0 and greater. At the unchoked pressure ratio of 1.5, the outer nozzle flow coefficient increased and exceeded 1.0. This was caused by the internal expansion area of the nozzles (the exit area was slightly larger than the throat area) and by the local surface curvature in the throat region. Since the exhaust-stream static pressure at the exit must equal ambient at this pressure ratio, the diverging internal area and throat curvature resulted in lower than ambient pressure in the nozzle throat. The throat Mach number and flow rate were thus higher than the ideal values calculated using the overall total-to-ambient pressure ratio. This lower than ambient pressure in the throat region can be seen in the measured pressures on the outer plug, an example of which is shown in Figure 71.

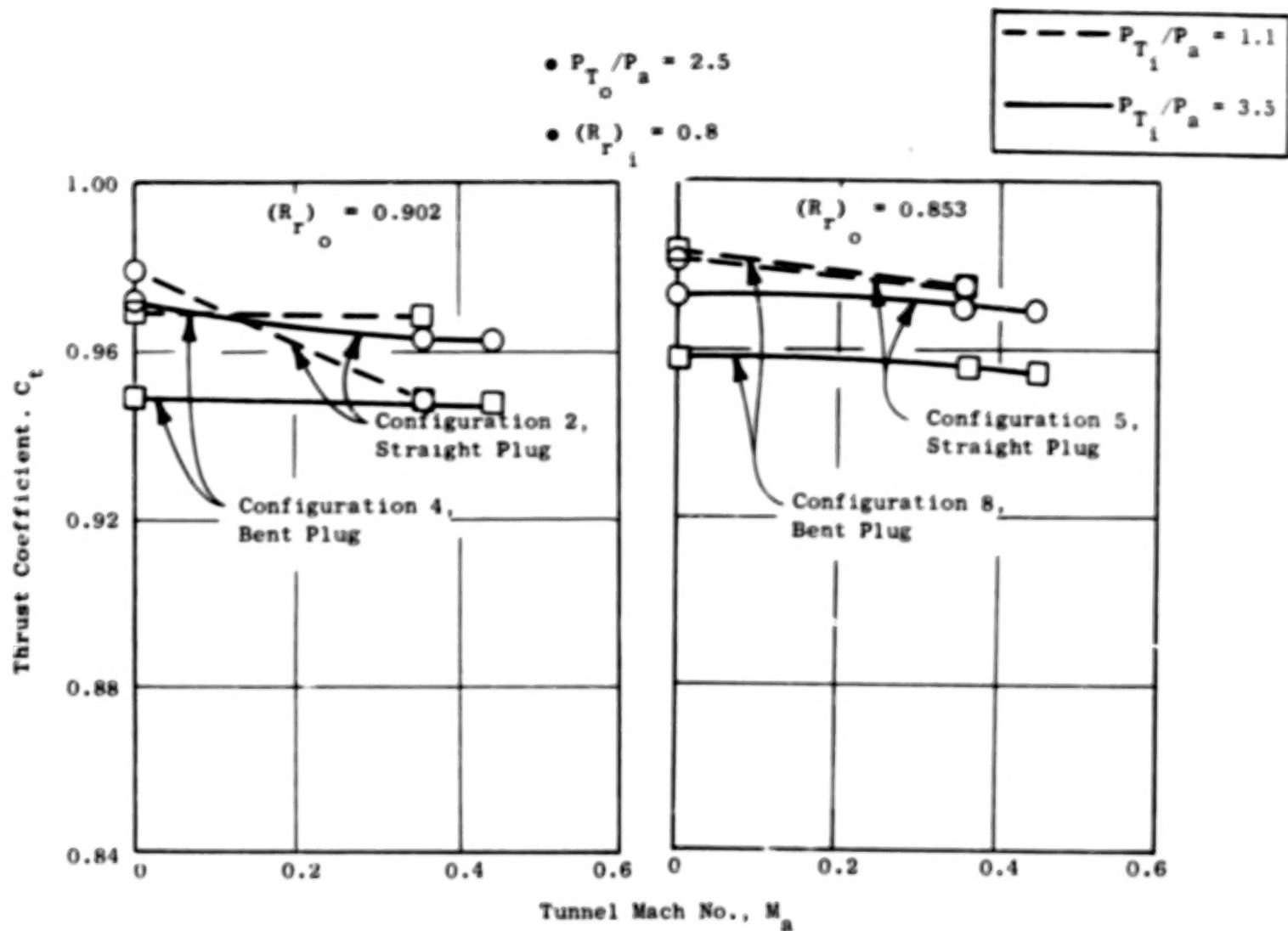


Figure 61. Thrust Coefficient as a Function of Tunnel Mach No. for High Inner Flow Rates.

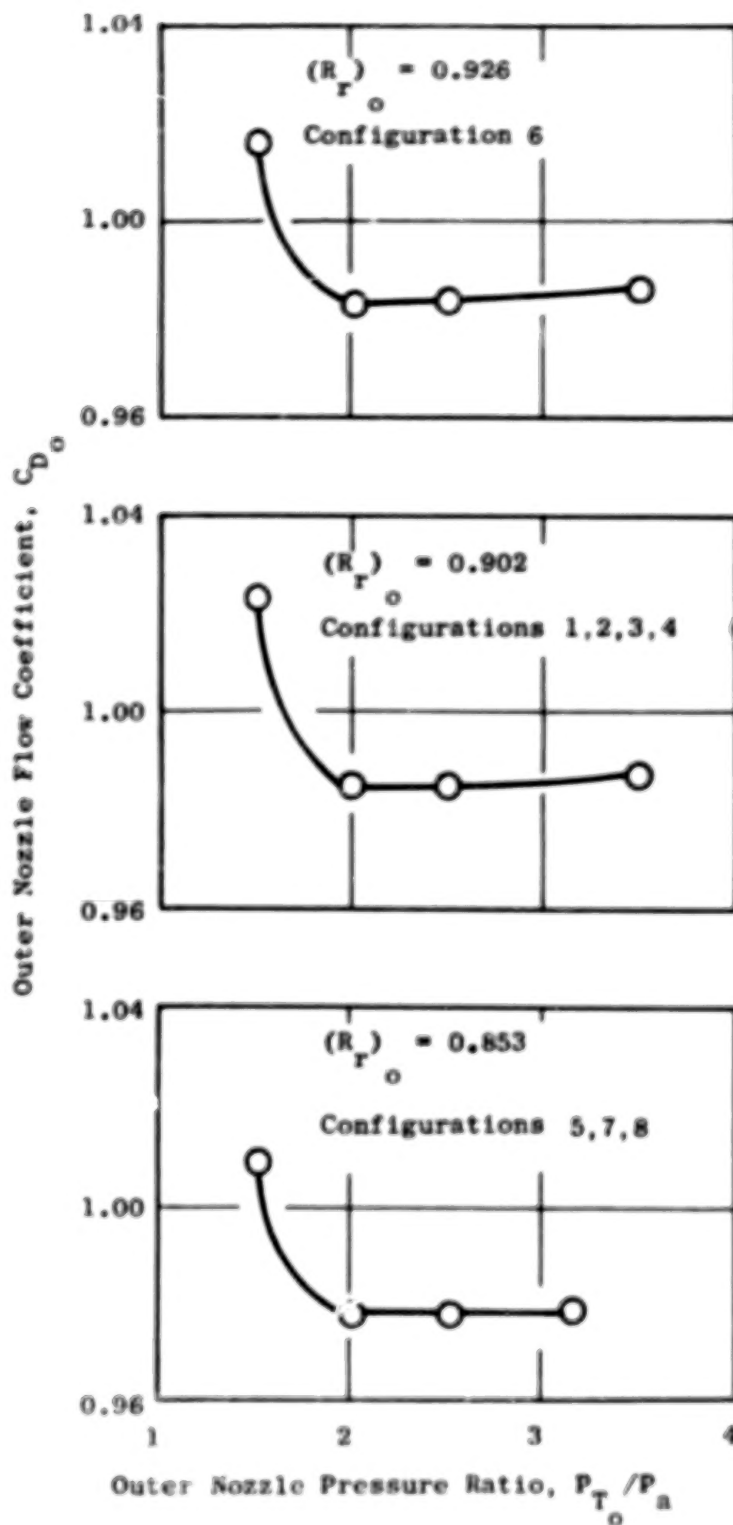


Figure 62. Outer Nozzle Flow Coefficients.

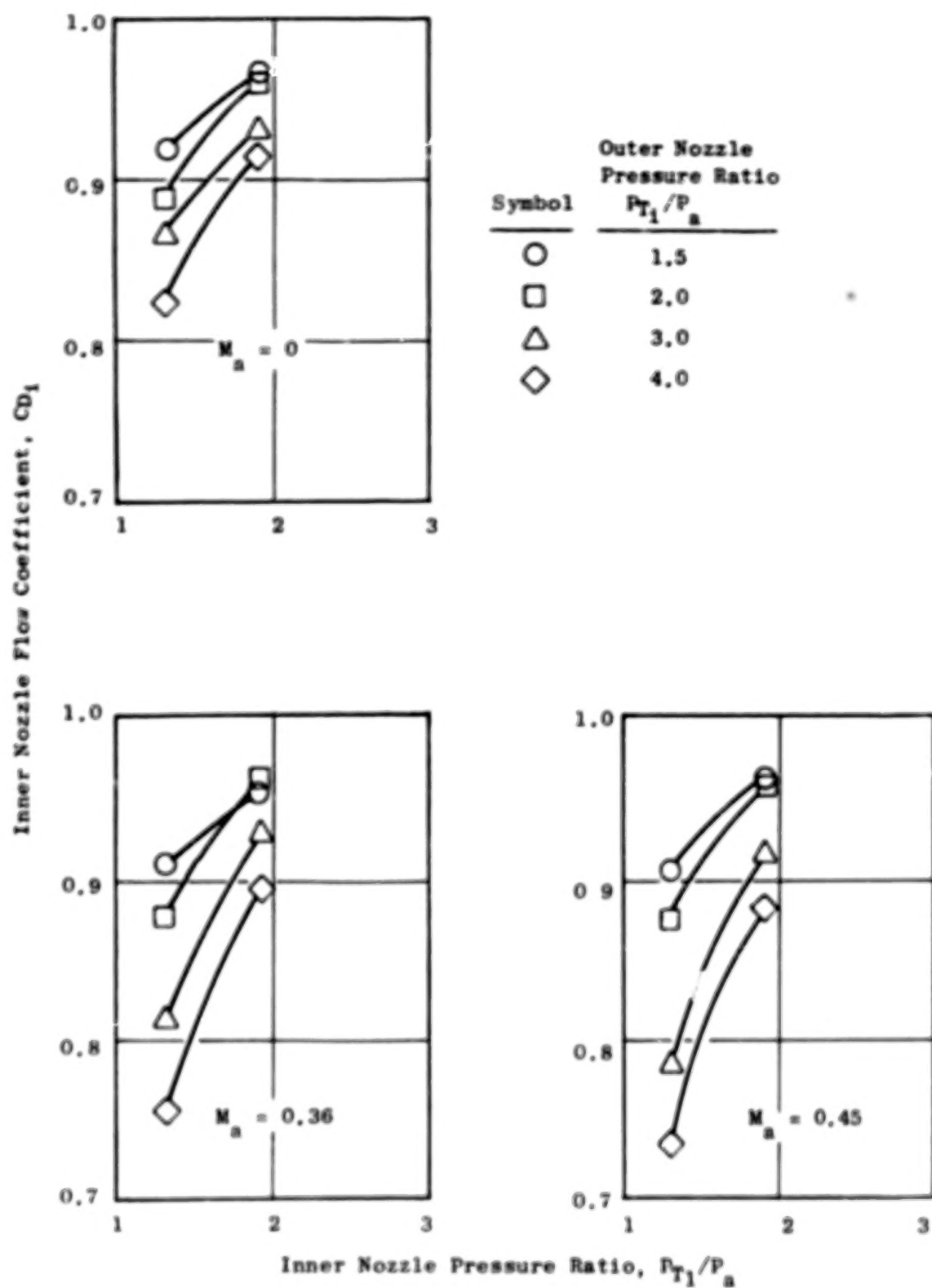


Figure 63. Inner Nozzle Flow Coefficients for Configuration 1 [ $(R_r)_o = 0.902$ ,  $(R_r)_i = 0.673$ , Bent Inner Plug].

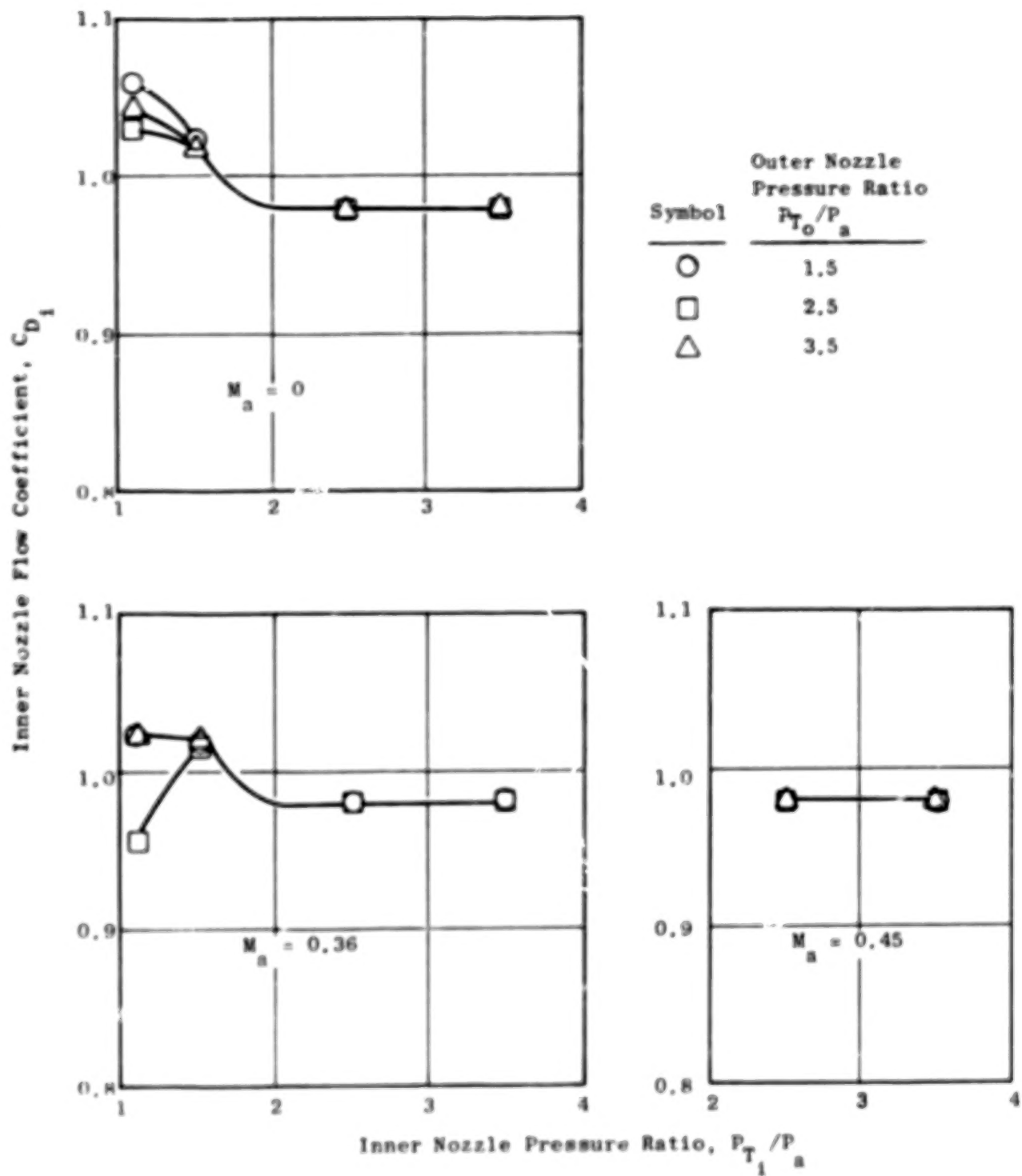


Figure 64. Inner Nozzle Flow Coefficients for Configuration 2 [ $(R_r)_o = 0.902$ ,  $(R_r)_i = 0.8$ , Conical Inner Plug].

# TABLE OF CONTENTS

<u>Section</u>	<u>Page</u>
1.0 SUMMARY	1 1/A10
2.0 INTRODUCTION	3 1/A12
2.1 List of Symbols	4 1/A13
3.0 TEST FACILITY DESCRIPTION	6 1/B1
4.0 MODEL DESCRIPTION	10 1/B5
5.0 DATA REDUCTION PROCEDURES	22 1/C3
5.1 Flow Rates	22 1/C3
5.2 Flow Coefficients	23 1/C4
5.3 Thrust Measurements	24 1/C5
5.4 Thrust Coefficient	26 1/C7
5.5 Pressure Data	26 1/C7
6.0 TEST RESULTS AND DISCUSSION	28 1/C9
6.1 Data Quality	28 1/C9
6.2 Model Thrust Coefficients	33 1/C14
6.2.1 Effect of Outer Nozzle Radius Ratio	52 1/E5
6.2.2 Effect of Inner Nozzle Radius Ratio	59 1/E12
6.2.3 Effect of Inner Nozzle Flow Rate and Pressure Ratio	64 1/F3
6.2.4 Effect of External Mach Number	80 1/G5
6.3 Model Flow Coefficients	85 1/G10
7.0 CONCLUSIONS	98 2/B1
APPENDIX - DATA REDUCTION PROCEDURES	99 2/B2
References	107 2/B10

# LIST OF ILLUSTRATIONS

<u>Figure</u>		<u>Page</u>	
1.	Schematic of Model System.	7	1/B2
2.	Schematic of Model Air Supply.	8	1/B3
3.	Schematic of Model Assembly.	11	1/B6
4.	Model Schematics, Configurations 1-4.	12	1/B7
5.	Model Schematics, Configurations 5-8.	13	1/B8
6.	Supersonic Tunnel Association Model Assembly.	15	1/B10
7.	Configuration 2 Mounted in NASA Tunnel.	16	1/B11
8.	Configuration 4 Mounted in NASA Tunnel.	17	1/B12
9.	Configuration 5 Mounted in NASA Tunnel.	18	1/B13
10.	Configuration 6 Mounted in NASA Tunnel.	19	1/B14
11.	Configuration 7 Mounted in NASA Tunnel.	20	1/C1
12.	STA Nozzle Mounted in NASA Tunnel.	21	1/C2
13.	Control Volume Applied to Model Test Setup.	25	1/C8
14.	STA Static Performance with the 3.1699 cm (1.248 in.) Diameter Flowmeter.	30	1/C11
15.	STA Static Performance with the 2.8951 cm (1.1398 in.) Diameter Flowmeter.	31	1/C12
16.	Wind-on STA Nozzle Thrust Coefficients.	32	1/C13
17.	STA Nozzle Bias and Standard Deviation on Static Thrust Coefficient.	34	1/D1
18.	STA Nozzle Bias and Standard Deviation on Flow Coefficient.	35	1/D2
19.	Thrust Coefficients for Configuration 1 [ $(R_r)_0 = 0.902$ , $(R_r)_1 = 0.673$ , Bent Inner Plug] with High Inner Flow Rates.	37	1/D4
20.	Thrust Coefficients for Configuration 1 [ $(R_r)_0 = 0.902$ , $(R_r)_1 = 0.673$ , Bent Inner Plug] with Low Inner Flow Rates.	38	1/D5



# LIST OF ILLUSTRATIONS (Continued)

<u>Figure</u>		<u>Page</u>	
21.	Configuration 1 Thrust Coefficients Compared to Previous Results.	39	1/D6
22.	Thrust Coefficients for Configuration 2 [ $(R_r)_o = 0.902$ , $(R_r)_i = 0.8$ , Conical Inner Plug] with High Inner Flow Rates.	40	1/D7
23.	Thrust Coefficients for Configuration 2 [ $(R_r)_o = 0.902$ , $(R_r)_i = 0.8$ , Conical Inner Plug] with High Inner Flow Rates.	41	1/D8
24.	Thrust Coefficients for Configuration 3 [ $(R_r)_o = 0.902$ , $(R_r)_i = 0.902$ , Conical Inner Plug] with High Inner Flow Rates.	42	1/D9
25.	Thrust Coefficients for Configuration 3 [ $(R_r)_o = 0.902$ , $(R_r)_i = 0.902$ , Conical Inner Plug] with Low Inner Flow Rates.	44	1/D11
26.	Thrust Coefficients for Configuration 4 [ $(R_r)_o = 0.902$ , $(R_r)_i = 0.8$ , Bent Inner Plug] with Low Inner Flow Rates.	45	1/D12
27.	Thrust Coefficients for Configuration 4 [ $(R_r)_o = 0.902$ , $(R_r)_i = 0.8$ , Bent Inner Plug] with Low Inner Flow Rates.	46	1/D13
28.	Inner Plug Pressure Distributions, Configuration 4 [ $(R_r)_o = 0.902$ , $(R_r)_i = 0.8$ , Bent Inner Plug].	47	1/D14
29.	Thrust Coefficients for Configuration 5 [ $(R_r)_o = 0.853$ , $(R_r)_i = 0.8$ , Conical Inner Plug] with High Inner Flow Rates.	48	1/E1
30.	Thrust Coefficients for Configuration 5 [ $(R_r)_o = 0.853$ , $(R_r)_i = 0.8$ , Conical Inner Plug] with Low Inner Flow Rates.	49	1/E2
31.	Thrust Coefficients for Configuration 6 [ $(R_r)_o = 0.926$ , $(R_r)_i = 0.8$ , Conical Inner Plug] with High Inner Flow Rates.	50	1/E3
32.	Thrust Coefficients for Configuration 6 [ $(R_r)_o = 0.926$ , $(R_r)_i = 0.8$ , Conical Inner Plug] with Low Inner Flow Rates.	51	1/E4
33.	Thrust Coefficients for Configuration 7 [ $(R_r)_o = 0.853$ , $(R_r)_i = 0.902$ , Conical Inner Plug] with High Inner Flow Rates.	53	1/E6

# LIST OF ILLUSTRATIONS (Continued)

<u>Figure</u>		<u>Page</u>	
34.	Thrust Coefficients for Configuration 7 [ $(R_r)_o = 0.853$ , $(R_r)_i = 0.902$ , Conical Inner Plug] with Low Inner Flow Rates.	54	1/E7
35.	Thrust Coefficients for Configuration 8 [ $(R_r)_o = 0.853$ , $(R_r)_i = 0.8$ , Bent Inner Plug] with High Inner Flow Rates.	55	1/E8
36.	Thrust Coefficients for Configuration 8 [ $(R_r)_o = 0.853$ , $(R_r)_i = 0.8$ , Bent Inner Plug] with Low Inner Flow Rates.	56	1/E9
37.	Thrust Coefficient as a Function of Outer Nozzle Radius Ratio for Low Inner Flow and Conical Inner Plug.	57	1/E10
38.	Thrust Coefficient as a Function of Outer Nozzle Radius Ratio for High Inner Flow Rates and Conical Inner Plug.	58	1/E11
39.	Thrust Coefficient as a Function of Outer Nozzle Radius Ratio for Low Inner Flow Rates and Bent Inner Plug.	60	1/E13
40.	Thrust Coefficient as a Function of Outer Nozzle Radius Ratio for High Inner Flow Rates and Bent Inner Plug.	61	1/E14
41.	Thrust Coefficient as a Function of Inner Nozzle Radius Ratio for Low Inner Flow Rates, $(R_r)_o = 0.902$ .	62	1/F1
42.	Thrust Coefficient as a Function of Inner Nozzle Radius Ratio for Low Inner Flow Rates, $(R_r)_o = 0.853$ .	63	1/F2
43.	Static Pressure Distribution, Configuration 2 [ $(R_r)_o = 0.902$ , $(R_r)_i = 0.8$ , Conical Inner Plug] with Zero Inner Flow.	65	1/F4
44.	Static Pressure Distribution, Configuration 3 [ $(R_r)_o = 0.902$ , $(R_r)_i = 0.902$ , Conical Inner Plug] with Zero Inner Flow.	66	1/F5
45.	Integrated Inner Plug Pressure Force as a Function of Inner Nozzle Radius Ratio for Low Inner Flow Rates.	67	1/F6
46.	Thrust Coefficient as a Function of Inner Nozzle Radius Ratio for High Inner Flow Rates, $(R_r)_o = 0.902$ .	68	1/F7
47.	Thrust Coefficient as a Function of Inner Nozzle Radius Ratio for High Inner Flow Rates, $(R_r)_o = 0.853$ .	69	1/F8

# LIST OF ILLUSTRATIONS (Continued)

<u>Figure</u>		<u>Page</u>	
48.	Thrust Coefficient as a Function of Inner Weight Flow for Low Inner Flow Rates, $M_a = 0$ .	70	1/F9
49.	Thrust Coefficient as a Function of Inner Weight Flow for Low Inner Flow Rates, $M_a = 0.36$ .	71	1/F10
50.	Static Pressure Distributions, Configuration 6 [( $R_r$ ) <sub>o</sub> = 0.926, ( $R_r$ ) <sub>i</sub> = 0.8, Conical Inner Plug] for Low Inner Flow Rates.	73	1/F12
51.	Thrust Coefficient as a Function of Inner Nozzle Pressure Ratio for High Inner Flow Rates, $M_a = 0$ .	74	1/F13
52.	Thrust Coefficient as a Function of Inner Nozzle Pressure Ratio for High Inner Flow Rates, $M_a = 0.36$ .	75	1/F14
53.	Inner Plug Integrated Pressure Force as a Function of Inner Nozzle Pressure Ratio for High Inner Flow Rates.	76	1/G1
54.	Static Pressure Distributions, Configurations 2 and 4, High Inner Flow, $P_{T1}/P_a = 1.1$ .	77	1/G2
55.	Static Pressure Distributions, Configurations 2 and 4, High Inner Flow, $P_{T1}/P_a = 2.5$ .	78	1/G3
56.	Static Pressure Distributions, Configurations 2 and 4, High Inner Flow, $P_{T1}/P_a = 3.5$ .	79	1/G4
57.	Thrust Coefficient as a Function of Tunnel Mach Number for Low Inner Flow Rates.	81	1/G6
58.	Inner Plug and Outer Plug Integrated Pressure Forces as a Function of Tunnel Mach Number for Low Inner Flow Rates, [( $R_r$ ) <sub>o</sub> = 0.902, ( $R_r$ ) <sub>i</sub> = 0.8].	82	1/G7
59.	Inner Plug and Outer Plug Integrated Pressure Forces as a Function of Tunnel Mach Number for Low Inner Flow Rates, [( $R_r$ ) <sub>o</sub> = 0.853, ( $R_r$ ) <sub>i</sub> = 0.8].	83	1/G8
60.	Shroud Drag as a Function of Tunnel Mach Number for Low Inner Flow Rates.	84	1/G9
61.	Thrust Coefficient as a Function of Tunnel Mach Number for High Inner Flow Rates.	86	1/G11

# LIST OF ILLUSTRATIONS (Concluded)

<u>Figure</u>		<u>Page</u>	
62.	Outer Nozzle Flow Coefficients.	87	1/G12
63.	Inner Nozzle Flow Coefficients for Configuration 1 [( $R_r$ ) <sub>o</sub> = 0.902, ( $R_r$ ) <sub>i</sub> = 0.673, Bent Inner Plug].	88	1/G13
64.	Inner Nozzle Flow Coefficients for Configuration 2 [( $R_r$ ) <sub>o</sub> = 0.902, ( $R_r$ ) <sub>i</sub> = 0.8, Conical Inner Plug].	89	1/G14
65.	Inner Nozzle Flow Coefficients for Configuration 3 [( $R_r$ ) <sub>o</sub> = 0.902, ( $R_r$ ) <sub>i</sub> = 0.902, Conical Inner Plug].	90	2/A7
66.	Inner Nozzle Flow Coefficients for Configuration 4 [( $R_r$ ) <sub>o</sub> = 0.902, ( $R_r$ ) <sub>i</sub> = 0.8, Bent Inner Plug].	91	2/A8
67.	Inner Nozzle Flow Coefficients for Configuration 5 [( $R_r$ ) <sub>o</sub> = 0.853, ( $R_r$ ) <sub>i</sub> = 0.8, Conical Inner Plug].	92	2/A9
68.	Inner Nozzle Flow Coefficients for Configuration 6 [( $R_r$ ) <sub>o</sub> = 0.926, ( $R_r$ ) <sub>i</sub> = 0.8, Conical Inner Plug].	93	2/A10
69.	Inner Nozzle Flow Coefficients for Configuration 7 [( $R_r$ ) <sub>o</sub> = 0.853, ( $R_r$ ) <sub>i</sub> = 0.902, Conical Inner Plug].	94	2/A11
70.	Inner Nozzle Flow Coefficients for Configuration 8 [( $R_r$ ) <sub>o</sub> = 0.853, ( $R_r$ ) <sub>i</sub> = 0.8, Bent Inner Plug].	95	2/A12
71.	Measured Static Pressure Distribution with Unchoked Outer Nozzle, Configuration 2, Low Inner Flow.	96	2/A13

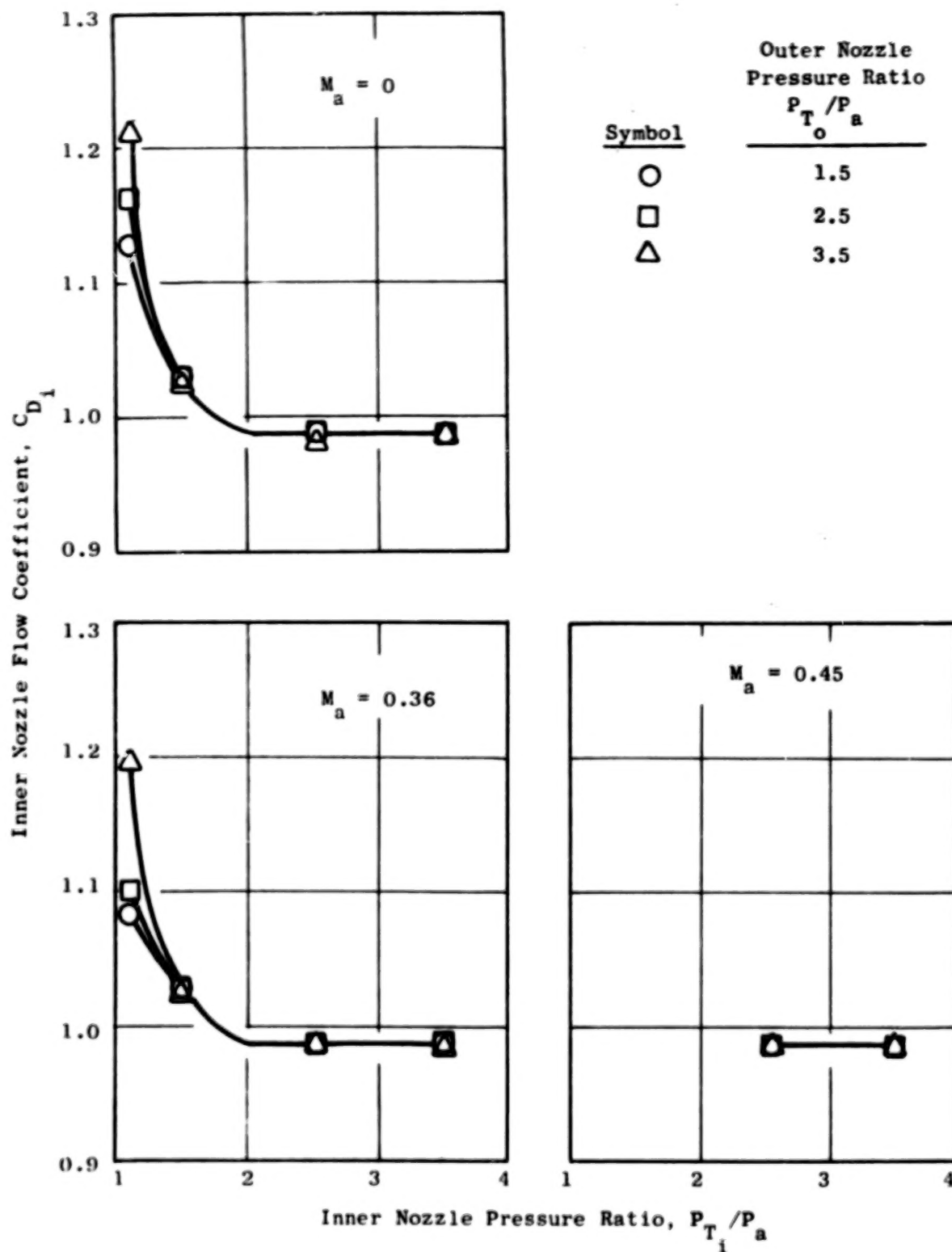


Figure 65. Inner Nozzle Flow Coefficients for Configuration 3  $[(R_r)_o = 0.902, (R_r)_i = 0.902, \text{Conical Inner Plug}]$ .

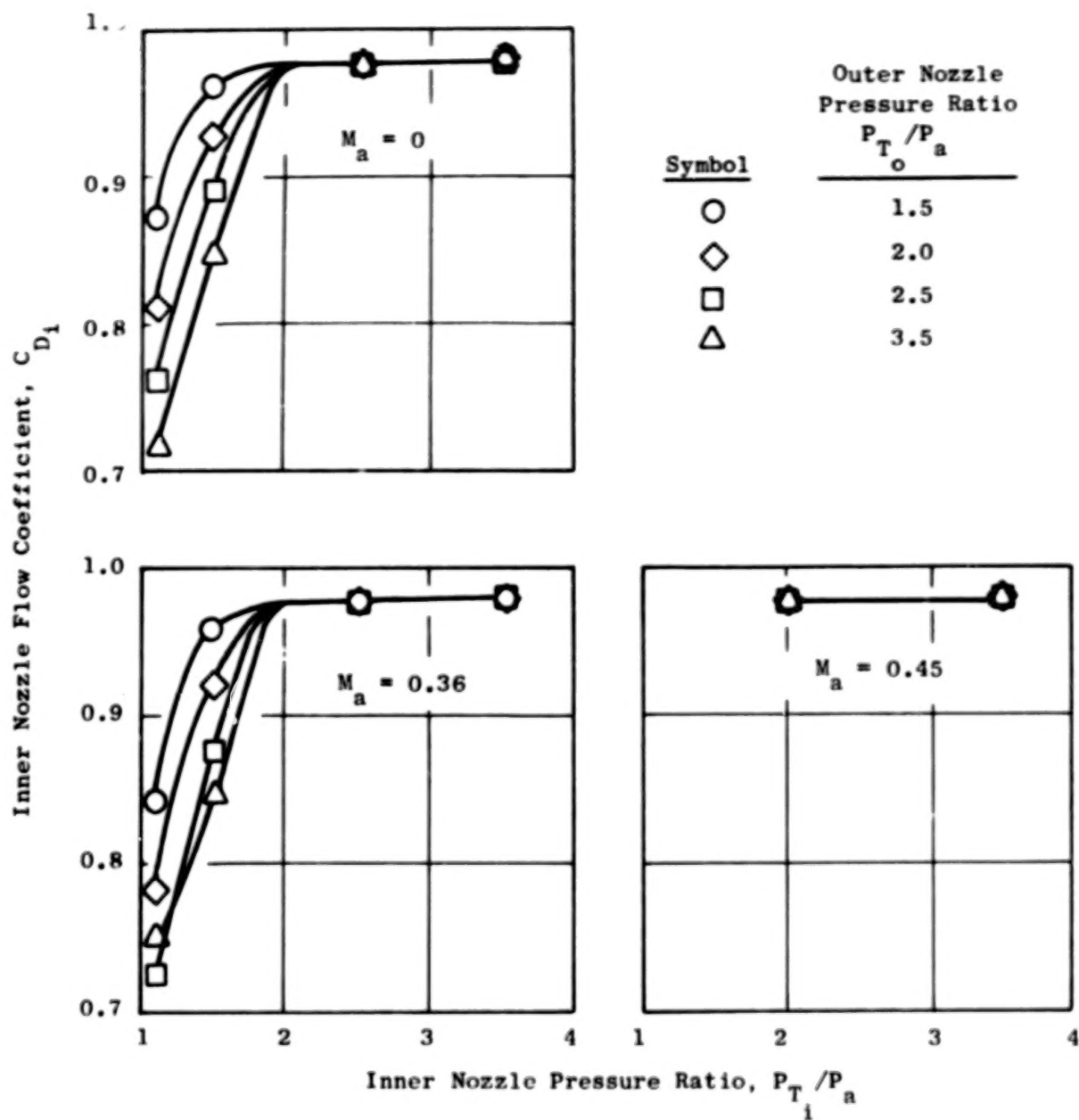


Figure 66. Inner Nozzle Flow Coefficients for Configuration 4  $[(R_r)_o = 0.902, (R_r)_i = 0.8, \text{ Bent Inner Plug}]$ .

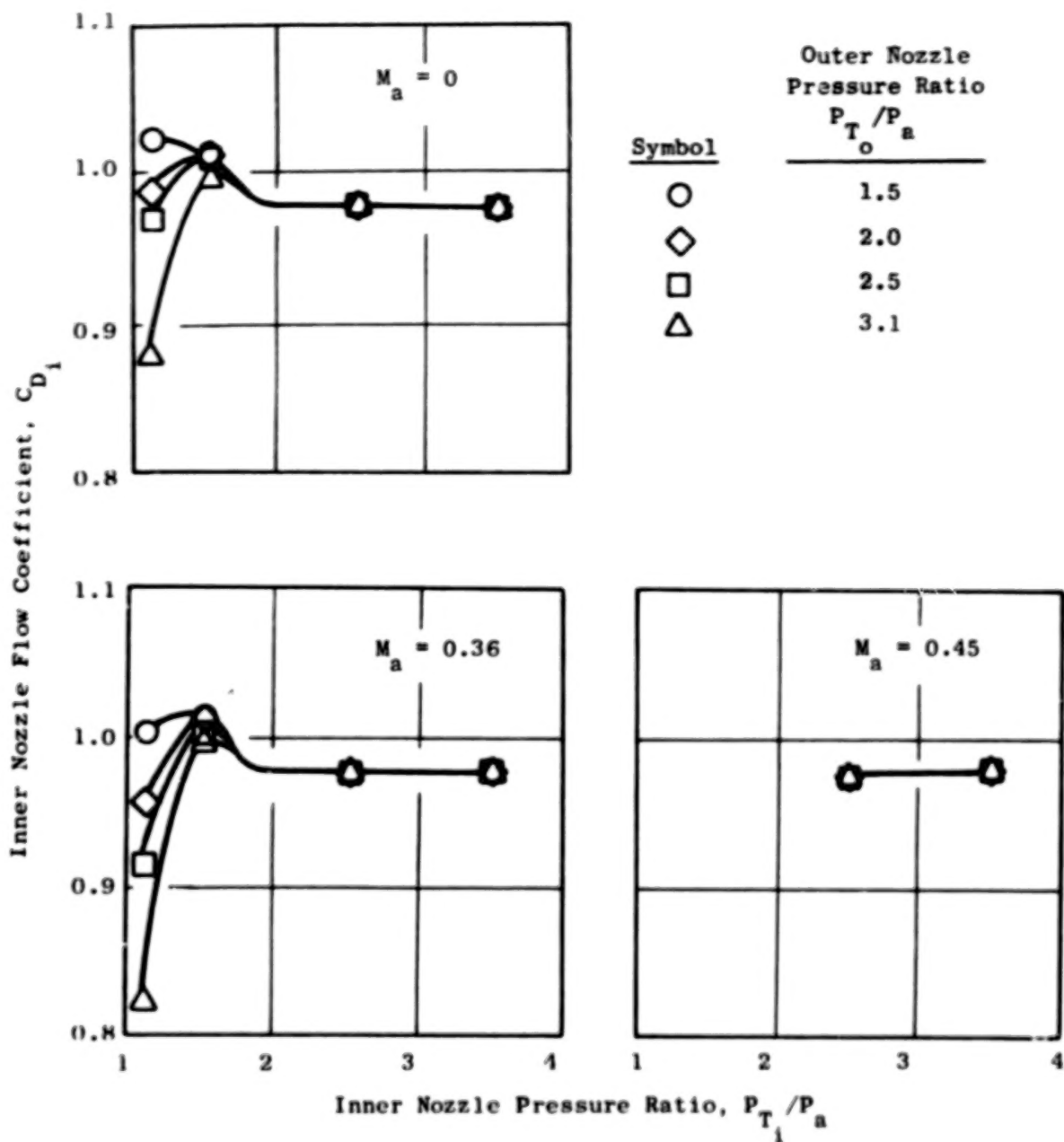


Figure 67. Inner Nozzle Flow Coefficients for Configuration 5  $[(R_r)_o = 0.853, (R_r)_i = 0.8, \text{Conical Inner Plug}]$ .

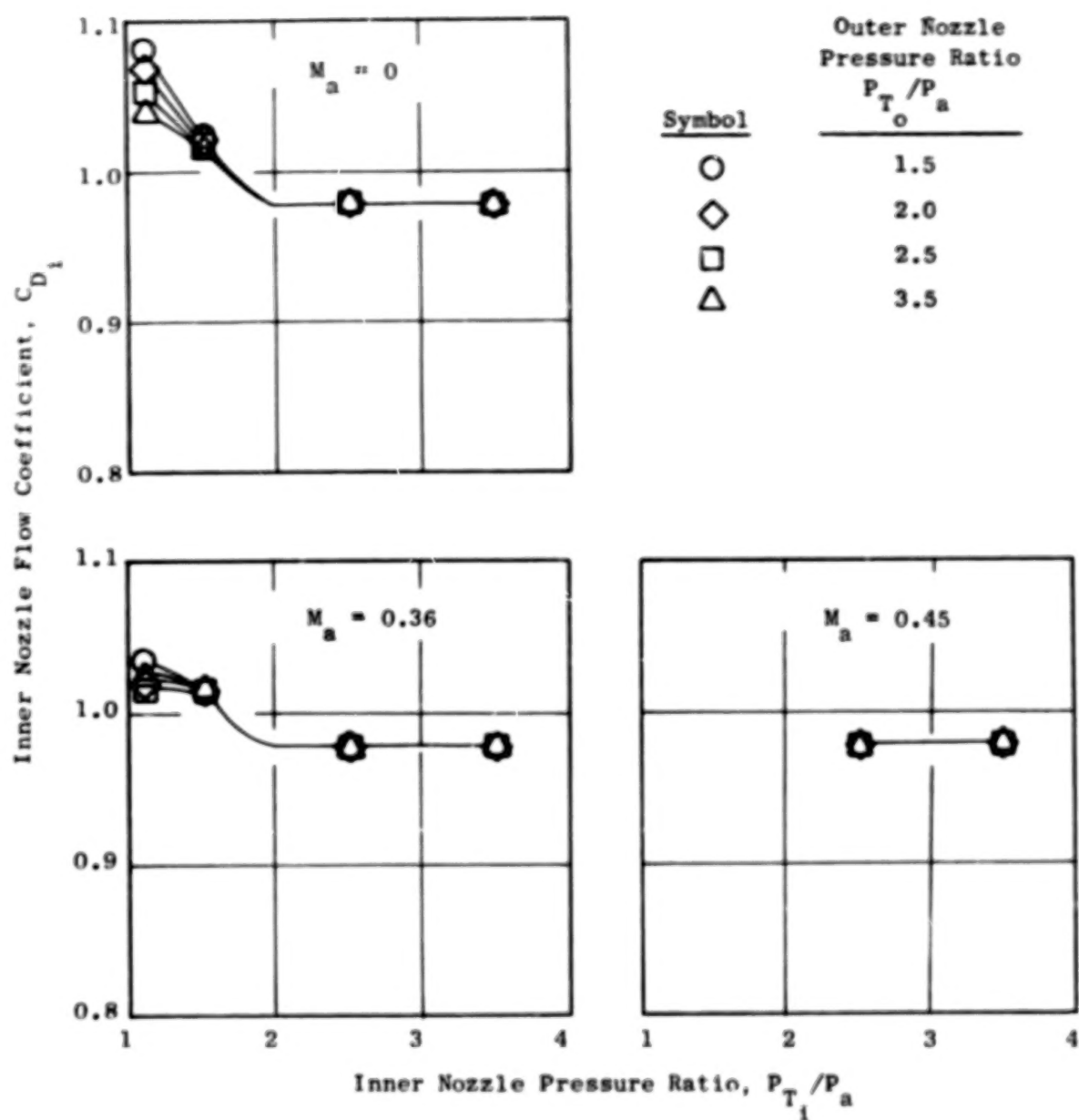


Figure 68. Inner Nozzle Flow Coefficients for Configuration 6  $[(R_r)_o = 0.926, (R_r)_i = 0.8, \text{Conical Inner Plug}]$ .



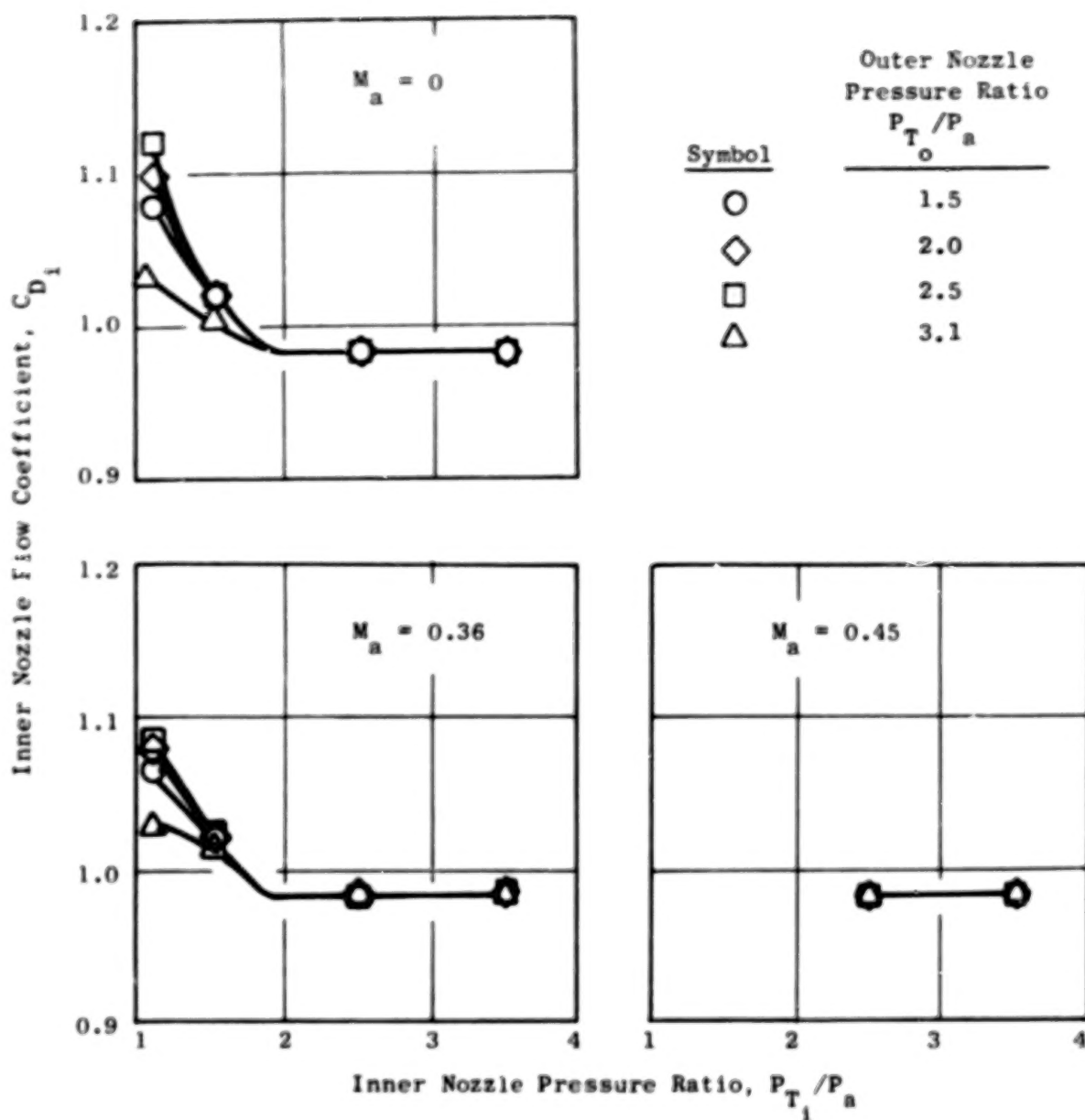


Figure 69. Inner Nozzle Flow Coefficients for Configuration 7  $[(R_r)_o = 0.853, (R_r)_i = 0.902, \text{Conical Inner Plug}]$ .

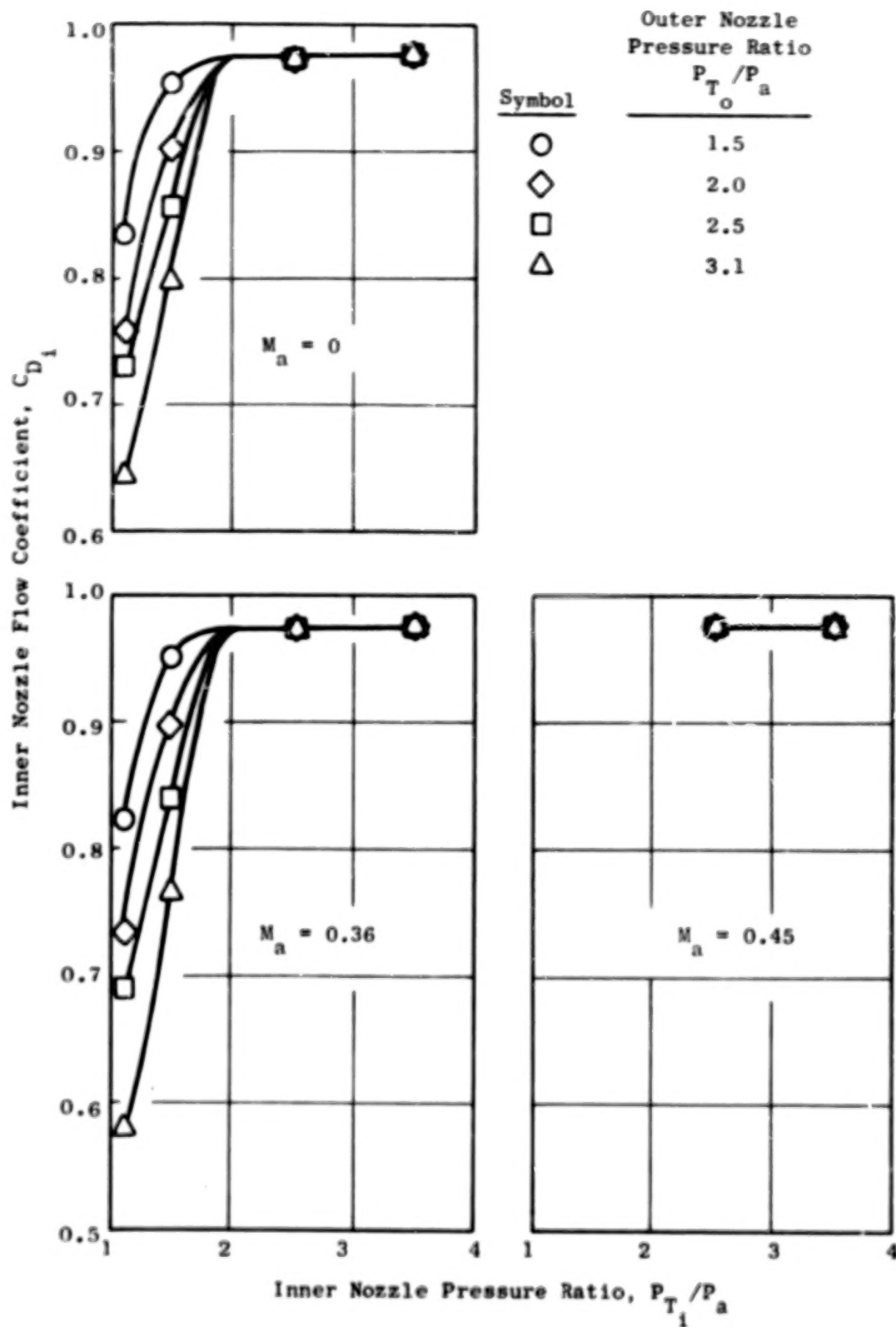


Figure 70. Inner Nozzle Flow Coefficients for Configuration 8  $[(R_r)_o = 0.853, (R_r)_i = 0.8, \text{ Bent Inner Plug}]$ .

- $P_{T_o}/P_a = 1.5$

- $W_1/W_o = 0$

- $M_a = 0$

- $DM = 0.203 \text{ m (8.0 in.)}$

Symbol	Tap Location
--------	--------------

○	Outer Shroud
---	--------------

□	Outer Plug
---	------------

△	Inner Plug
---	------------

Note:  $X/DM = 0$  at Plane of Outer Nozzle Throat

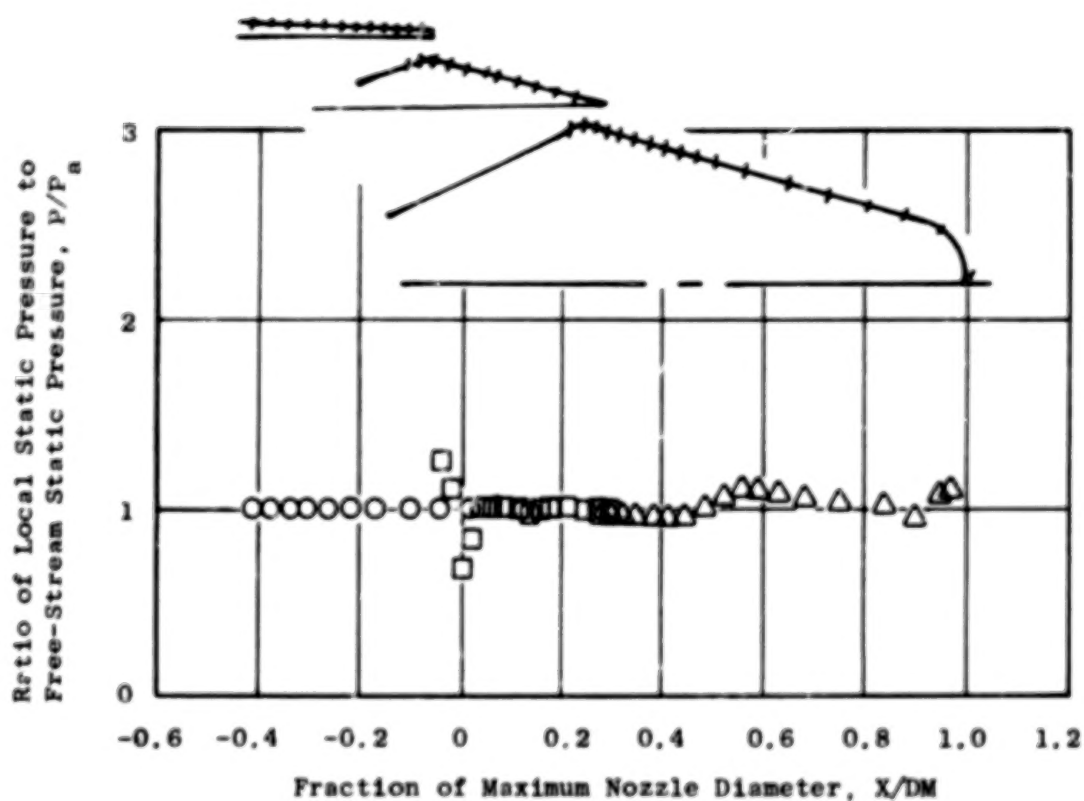


Figure 71. Measured Static Pressure Distribution with Unchoked Outer Nozzle, Configuration 2, Low Inner Flow.

The inner nozzle flow coefficients for choked pressure ratios varied from 0.975 to 0.988. At lower than critical pressure ratios the inner flow coefficients exhibited either of two characteristics, dependent on the plug geometry. The configurations with conical inner plugs exhibited generally higher flow coefficients when the nozzle was unchoked, for the same reasons described above for the outer nozzle. The bent core plugs invariably showed a substantial drop in flow coefficient with the nozzle unchoked. This was due to the interaction of the outer and inner streams where the two merge. The shallow angle of the bent plugs allowed the outer stream to create a restriction in the flow area of the inner stream, raising the static pressure in the throat region and lowering the flow coefficient. Some configurations, most notably Configuration 5, Figure 67, exhibited both characteristics, increasing at some combinations of inner and outer pressure ratio and decreasing at others.

## 7.0 CONCLUSIONS

The data obtained in the NASA Lewis 8 x 6 foot wind tunnel was of high quality. STA nozzle results indicated test data accuracy and repeatability to be generally better than  $\pm 0.5\%$ .

The coannular plug nozzle models exhibited no inherent characteristics which would preclude attaining high performance levels when operating with high inner flow rates. Performance levels up to 0.98 statically and 0.974 at Mach 0.36 were demonstrated. However, the bent inner plug geometry, with an abrupt change in plug angle, incurred a performance loss at high inner nozzle pressure ratios of 1 to 2%, relative to the conical plug geometry.

The coannular plug nozzle models operating with low, or bleed, inner flow rates experienced a pump-down in pressure of the inner nozzle flow area. This low pressure region resulted in a significant thrust loss, particularly at the zero bleed and lowest bleed conditions and on those configurations for which the inner flow area was large, i.e., low inner radius ratio.

## APPENDIX

### DATA REDUCTION PROCEDURES

A detailed description of the data reduction procedures is given in the following sections. All the constants and equations in this appendix are given as actually used in the data reduction programs and as such are consistent with English units and not metric units.

#### FLOW RATES

The mass flow through the outer nozzle was measured with a 3.1699 cm (1.248 in.) throat diameter choked venturi meter, located as shown in Figure 2. The flow rate was calculated using the equation:

$$W_o = C_{DV_o} \frac{K_{V_o} P_{TV_o} A_{V_o}}{\sqrt{T_{TV_o}}} \quad (14)$$

The critical flow factor,  $K_{V_o}$ , was calculated as a function of total pressure and temperature:

$$K_{V_o} = 0.5282 + a T_{TV_o} + b T_{TV_o}^2 + c T_{TV_o}^3 + (1.86 \times 10^{-5}) P_{TV_o} e^{-.0067 (T_{TV_o} - 500.00)} \quad (15)$$

where

$$\begin{aligned} a &= 1.654 \times 10^{-5} \\ b &= -2.119 \times 10^{-8} \\ c &= 6.008 \times 10^{-12} \end{aligned}$$

where  $T_{TV_o}$  and  $P_{TV_o}$  are in R and psia, respectively.

This equation was obtained by curve-fitting tabulated values in Reference 3.

The meter flow coefficient was calculated as a function of the throat Reynolds number using the following semiempirical relation:

$$C_{D_{V_0}} = 0.9983 (1 - .0691 RN^{-0.183}) \quad (16)$$

The 0.9983 factor in the equation is to account for the effects of sonic line distortion.

The meter total pressure,  $P_{T_{V_0}}$ , was determined by measuring the static pressure,  $P_{V_0}$ , upstream of the venturi throat and calculating the total pressure as:

$$P_{T_{V_0}} = P_{V_0} / 0.9995 \quad (17)$$

The 0.9995 factor is the static-to-total pressure ratio for that Mach number based on the ratio of the area at the measurement plane to the meter throat area. The static pressure was measured by six taps, each of which was sampled four times with dummy scanning valves during the taking of each data point. These 24 readings were averaged to determine the static pressure.

The meter total temperature,  $T_{T_{V_0}}$ , was determined using five platinum resistance thermometers located upstream of the venturi. Each thermometer was read twice and the readings averaged.

The mass flow through the inner nozzle was measured with either of two choked venturi meters located as shown on Figure 2. The flow for high inner flow rates was measured using the 2.8951 cm (1.1398 in.) throat diameter venturi. The flow for the low inner flow rate testing was measured with the 1.0122 cm (0.3985 in.) throat diameter venturi. For both meters, the flow rate was calculated using the equation:

$$W_1 = \frac{K_{V_1} P_{V_1}}{60.00 \sqrt{T_{T_{V_1}}}} \quad (18)$$

This equation is based on calibration of the meters made by the manufacturer. The  $K_{V_1}$  factors based from the calibration were:

$$K_{V_1} = (-1.9153 \times 10^{-7}) P_{V_1}^2 + (1.10896 \times 10^{-3}) P_{V_1} + 32.29807 \quad (19)$$

for the 2.8951 cm (1.1398 in.) diameter meter, and:

$$K_{V_1} = (-3.02076 \times 10^{-8}) P_{V_1}^2 + (9.49693 \times 10^{-4}) P_{V_1} + 3.93951 \quad (20)$$

for the 1.0122 cm (0.3985 in.) diameter meter.

The meter static pressure,  $P_{V_1}$ , was measured upstream of the venturi throat with four static taps, each of which was read twice and the eight numbers averaged. The venturi total temperatures were measured with three thermocouples (each read twice) located upstream of the meter.

### FLOW COEFFICIENTS

The flow coefficient of a nozzle is defined as the ratio of actual mass flow rate through the nozzle to the ideal isentropic flow rate at the temperature and pressure of the flow:

$$C_D = \frac{\text{measured } W}{\text{ideal } W} \quad (21)$$

The ideal weight flow for the outer nozzle flow was calculated from the relation:

$$W_{I_O} = \frac{K_O A_O P_{T_O}}{\sqrt{T_{T_O}}} \left( \frac{A^*}{A_O} \right) \quad (22)$$

$A_O$  is the outer nozzle physical throat area and

$$K_O = 0.5282 + a T_{T_O} + b T_{T_O}^2 + c T_{T_O}^3 + (1.86 \times 10^{-5}) P_{T_O} e^{-.0067 (T_{T_O} - 500.00)} \quad (23)$$

where  $a$ ,  $b$ , and  $c$  are as given in the previous section, and  $T_{T_O}$  and  $P_{T_O}$  are in R and psia, respectively.

The nozzle temperature,  $T_{T_O}$ , and pressure,  $P_{T_O}$ , were measured upstream of the nozzle throat with multielement rakes. These rakes were placed downstream of



choke plates and screens which provided a flow with no pressure profile distortion at the rakes to assure an accurate pressure measurement. The outer nozzle rakes contained eight total pressure probes, the readings of which were averaged to arrive at  $P_{T_0}$ , and two thermocouples, the readings of which were averaged. The inner nozzle rakes contained five Pitot tubes and one thermocouple.

For values of nozzle pressure ratio greater than 1.8929,  $A^*/A_0$  in the ideal weight flow equation is equal to one. For lower pressure ratios,  $A^*/A_0$  was calculated from the isentropic relationships;

$$A^*/A_0 = \frac{216}{125} M_0 \left( 1 + \frac{M_0^2}{5} \right)^{-3} \quad (24)$$

where

$$M_0 = \left\{ 5 \left[ \left( \frac{P_{T_0}}{P_a} \right)^{0.28571} - 1 \right] \right\}^{1/2} \quad (25)$$

The inner nozzle ideal weight flow was calculated in identical fashion as the outer nozzle, but using the inner nozzle throat area, flow pressure and temperature. For the low inner flow testing, the inner nozzle total pressures required to supply the low flow rates were generally lower than ambient pressure due to the pumping effect of the outer flow. In these cases, the ideal flow rate and flow coefficients are meaningless and were not calculated.

#### THRUST MEASUREMENTS

The thrust of the exhaust nozzles is defined as the axial exit momentum of the exhaust flow, plus the excess of exit pressure over ambient pressure times the exit area normal to the axis, minus the axial drag on the nozzle external surface, i.e.,

$$F = \int_{A_{\text{exit}}} d(WV)_{\text{axial}} + \int_{A_{\text{exit}}} (P - P_a) dA - D_{\text{external}} \quad (26)$$

The external drag consists of both the pressure drag on the boattail surface and the axial component of skin friction. Figure 13 shows a control volume applied to the test nozzles. Writing the momentum equation in the axial direction for this control volume demonstrates how the thrust was measured for the tests:

$$F = F_{LC} + F_{AS} + A_1(P_1 - P_a) + A_2(P_2 - P_a) + A_3(P_3 - P_a) + A_4(P_4 - P_a) \quad (27)$$

where  $F_{LC}$  is the axial force applied to the load cell and  $F_{AS}$  is the axial force applied at the boundary of the control volume by the air supply tubes. The static pressures  $P_1$ ,  $P_2$ ,  $P_3$ , and  $P_4$  were measured with two static taps 180° apart at each of the four areas (see Figure 13). The force measuring system was calibrated by applying known forces and correlating this force against the load cell output, as previously described in Section 3.0. This calibration provided a linear relationship between the applied load and the load cell output in millivolts which was used to determine the load cell plus air supply tube force as follows:

$$\text{Applied Load} = a \text{ (mv)} + b = F_{LC} + F_{AS} \quad (28)$$

where  $a$  and  $b$  are constants determined by the calibrations and  $mv$  is the load cell reading in millivolts. The load cell was sampled 48 times during the taking of each point, the above calculation made for each sample, and the results averaged to yield the measured force.

An adjustment was made to the measured thrust to account for external friction drag on the cylindrical section upstream of the nozzle shroud. The axial force on this 20.32 cm (8.0 in.) diameter section, which extended from the metric-break to the attach-point of the nozzle shrouds, was not included in the nozzle net thrust. The friction drag was calculated by the equation:

$$D_f = \frac{\gamma}{2} P_a M_a^2 A_c C_f \quad (29)$$

where  $A_c$  is the wetted surface area of the cylindrical piece 20.32 cm (8.0 in.) in diameter and 17.78 cm (7.0 in.) in length. The drag coefficient was calculated from

$$C_f = 0.288 (1 + 0.2 M_a^2)^{-0.5} (\log_{10} RN_x)^{-2.45} \quad (30)$$

where  $RN_x = 9.37 RN_a$ ,  $RN_a$  being the Reynolds number per foot based on the ambient stream Mach number, temperature, and pressure.

The thrust of the nozzles for this test was therefore given by;

$$F = F_{LC} + F_{AS} + A_1(P_1 - P_a) + A_2(P_2 - P_a) + A_3(P_3 - P_a) + A_4(P_4 - P_a) + D_f \quad (31)$$

or, substituting the equations by which  $F_{LC} + F_{AS}$  and  $D_f$  were calculated:

$$F = a(mv) + b + A_1(P_1 - P_a) + A_2(P_2 - P_a) + A_3(P_3 - P_a) + A_4(P_4 - P_a) + \frac{\gamma}{2} P_a M_a^2 A_c C_f \quad (32)$$

#### THRUST COEFFICIENT

The thrust coefficient is the ratio of the measured nozzle thrust to the ideal thrust of the inner duct flow plus the ideal thrust of the outer duct flow. The ideal thrust for each stream equals the actual mass flow rate times the ideal velocity, i.e., the velocity of the stream expanded isentropically from the total pressure to the ambient pressure. The equation for the thrust coefficient is thus:

$$C_T = \frac{F}{W_o V_{I_o} + W_1 V_{I_1}} \quad (33)$$

The ideal thrust for the nozzles was calculated using the dimensionless ideal-thrust function which is a function of only the nozzle pressure ratio:

$$\frac{W_I V_I}{P_T A^*} = \gamma \left( \frac{2}{\gamma+1} \right)^{\frac{\gamma}{\gamma-1}} \left( \frac{\gamma+1}{\gamma-1} \right)^{1/2} \left[ 1 - (P_a/P_T)^{\frac{\gamma-1}{\gamma}} \right]^{1/2} \quad (34)$$

$$= 1.81163 \sqrt{1 - (P_a/P_T)^{0.28571}} \quad \text{for } \gamma = 1.4$$

The ideal thrust for the inner and outer streams was then:

$$W_I V_{I_1} = C_{D_1} P_{T_1} A_1 \left( \frac{A_1^*}{A_1} \right) \left( \frac{W_{I_1} V_{I_1}}{P_{T_1} A_1^*} \right) \quad (35)$$

$$W_O V_{I_O} = C_{D_O} P_{T_O} A_O \left( \frac{A_O^*}{A_O} \right) \left( \frac{W_{I_O} V_{I_O}}{P_{T_O} A_O^*} \right)$$

For pressure ratios greater than 1.8929,  $A^*/A = 1.0$ . For pressure ratios less than this,  $A^*/A$  was calculated as described in the previous section on flow coefficients.

During much of the low inner flow rate testing, the total pressure of the inner nozzle flow was lower than ambient. In these cases, the ideal thrust of the inner nozzle was set equal to zero.

For the static thrust tests of the STA model, a dimensionless stream-thrust parameter was also calculated as:

$$f_9 = \frac{F + P_a A_9}{P_T A_9} \quad (36)$$

where  $A_9$  is the STA nozzle exit area.

### PRESSURE DATA

Total pressures in the models and static pressures on the model surfaces were measured with scanning value/transducer arrangements. The individual static pressure readings were also nondimensionalized by the ambient pressure. Pressure forces on the aft-facing portions of the shroud, outer plug, and inner plug were calculated by multiplying the difference between the static pressure at each tap and ambient by an incremental projected area represented by the particular tap and summing the products, i.e.,

$$F_p = \sum (P - P_a) \Delta A \quad (37)$$

These pressure forces were also nondimensionalized by the total ideal thrust of the nozzle:

$$\frac{F_p}{W_i V_{I_i} + W_o V_{I_o}} \quad (38)$$

#### REFERENCES

1. Compton, W.B., and Runckel, J.F.; "Jet Effects on the Boattail Axial Force of Conical Afterbodies at Subsonic and Transonic Speeds," NASA TM X-1960, 1970.
2. Blozy, J.T., Knott, P.R., and Staid, P.S.; "Acoustic and Performance Investigation of Annular Plug Nozzles with Base Bleed," Concept Screening and Model Design Report, NASA Contract NAS3-19777, 1976.
3. Johnson, R.C.; "Real-Gas Effects in Critical Flow Through Nozzles and Tabulated Thermodynamic Properties," NASA TN D-2565, 1965.
4. Siegfried, R.G., and Kuchar, A.P.; "A Standard for Exhaust Nozzle Tests," General Electric Company, ESAD Technical Brief 71006. April 6, 1971.
5. Harrington, D.E., Schloemer, J.J., and Skebe, S.A.; "Thrust Performance of Isolated 36-Chute Suppressor Plug Nozzles with and Without Ejectors at Mach Numbers from 0 to 0.45," NASA TM X-3298, October 1/75.
6. Knott, P.R., Heck, P.H., Latham, D., Brausch, J.F., Stringas, E.J., and Staid, P.S.; "Acoustic Tests of Duct-Burning Turbofan Jet Noise Simulation," NASA CR-2966, 1 February 1978.

1. Report No. <b>NASA CR-2990</b>	2. Government Accession No.	3. Recipient's Catalog No.	
4. Title and Subtitle  <b>WIND TUNNEL PERFORMANCE TESTS OF COANNULAR PLUG NOZZLES</b>		5. Report Date <b>April 1978</b>	
		6. Performing Organization Code	
7. Author(s)  <b>Paul S. Staid</b>		8. Performing Organization Report No.  <b>77AEG596</b>	
		10. Work Unit No.	
9. Performing Organization Name and Address  <b>General Electric Company 1 Jimson Road Cincinnati, Ohio 45215</b>		11. Contract or Grant No.  <b>NAS3-19777</b>	
		13. Type of Report and Period Covered  <b>Contractor Report</b>	
12. Sponsoring Agency Name and Address  <b>National Aeronautics and Space Administration Washington, D.C. 20546</b>		14. Sponsoring Agency Code	
15. Supplementary Notes  <b>Final report. Project Manager, Orlando A. Gutierrez, V/STOL and Noise Division, NASA Lewis Research Center, Cleveland, Ohio 44135.</b>			
16. Abstract  Wind tunnel performance test results and data analyses are presented for dual-flow plug nozzles applicable to supersonic cruise aircraft during takeoff and low-speed flight operation. Outer exhaust stream pressure ratios from 1.5 to 3.5 were tested; inner exhaust stream conditions were varied from very low, or bleed flow rate up to a pressure ratio of 3.5. Mach numbers tested ranged from zero to 0.45. Measured thrust coefficients for the eight model configurations, operating at an external Mach number of 0.36 and an outer flow pressure ratio of 2.5, varied from 0.95 to 0.974 for high inner flow rates. At low inner flow, the performance ranged from 0.88 to 0.97 for the same operating conditions. The primary design variables influencing the performance levels were the annular height of the inner and outer nozzle throats (denoted by radius ratio - the ratio of inner-to-outer flowpath diameter at the nozzle throat), the plug geometry, and the inner stream flow rate.			
17. Key Words (Suggested by Author(s)) <b>Thrust coefficient Flow coefficient Exhaust nozzle Exhaust noise Design parameters</b>		18. Distribution Statement <b>Unclassified - unlimited STAR Category 01</b>	
19. Security Classif. (of this report)  <b>Unclassified</b>	20. Security Classif. (of this page)  <b>Unclassified</b>	21. No. of Pages  <b>114</b>	22. Price*  <b>A06</b>





**END**

**9. 19. 78**